ELECTRON MICROSCOPY OF SOLIDS

Ross A. Blackley

A Thesis Submitted for the Degree of MPhil
at the
University of St Andrews

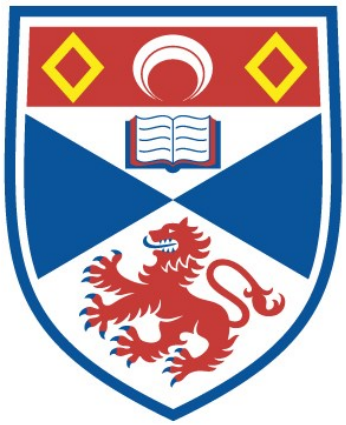

2005

ELECTRON MICROSCOPY OF SOLIDS

Ross A Blackley

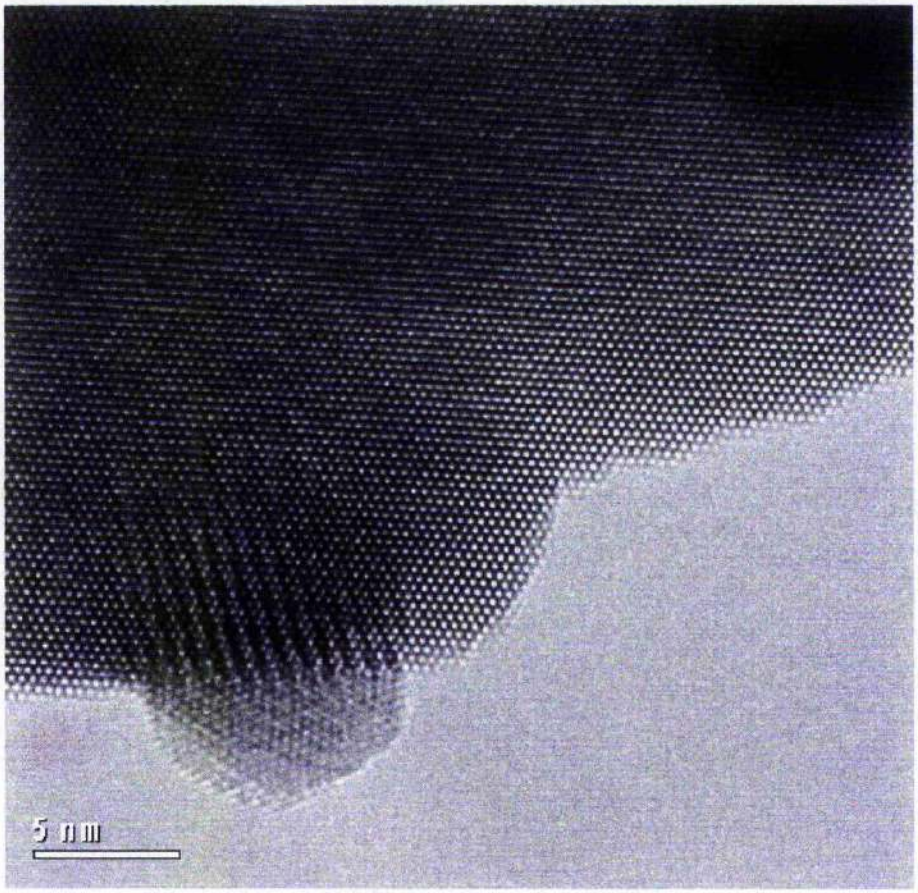

A Dissertation Submitted for the Degree of Master of Philosophy
School of Chemistry, University of St Andrews
September, 2004

Contents

SECTION TWO – SEM AND CHEMICAL ANALYSIS OF SOLIDS

DECLARATION

I, Ross Alexander Blackley, hereby certify that this thesis, which is approximately 26000 words in length, has been written by me, that is the record of work carried out by me, that is the record of work carried out by me that has not been submitted in any previous application for a higher degree.

Date 28/09/2004 Signature of Candidate

I was admitted as a candidate for a part-time degree of Master of Philosophy in September 2001, the higher study for which this is a record was carried out in the University of St Andrews between 2001 and 2004.

Date 28/09/2004 Signature of Candidate

I hereby certify that the candidate has fulfilled the conditions of the Resolution and Regulations appropriate for the part-time degree of Master of Philosophy in the University of St Andrews and that the candidate is qualified to submit this thesis in application for that degree.

Date 28/09/2004 Signature of Supervisor

In submitting this thesis to the University of St Andrews I understand that I am giving permission for it to be made available for use in accordance with the regulations of the University library for the time being in force, subject to any copyright vested in the work not being affected thereby. I also understand that the title and abstract will be published, and that a copy of the work may be made and supplied by any bona fide library or research worker.

Date 28/09/2004 Signature of Candidate

Acknowledgements

The work undertaken throughout the three years of this project could not have been completed without the help of the people I would like to thank below:

- My supervisor, Dr Wuzong Zhou, for advice on high resolution TEM, theoretical knowledge and many aspects of solid state chemistry.

- Professor John Irvine and his research team, especially for help and advice in the use of the high temperature tube furnaces.

- Dr Phil Lightfoot for continuing advice on the use of the Philips X-ray diffractometer.

Abstract

A series of compounds with general composition $Ba_{1\pm x}Bi_{1\mp x}O_3$ were prepared (x=0.05, 0.1, 0.2, 0.4, 0.5). The compounds were then studied by means of selected area electron diffraction and high resolution transmission electron microscopy. It was found that for a small change in the cation composition there was little or no overall change to the basic perovskite unit cell structure, whereas for the compounds with more marked changes in cation composition subtle changes to the basic unit cell were recorded.

The evidence for transformation is presented by changes in the diffraction patterns and HRTEM imaging. These changes are compared with the results expected and observed for the basic perovskite unit cell for the standard $BaBiO_3$ sample. It is thought that these changes in structure are brought about by the ordering of the Bi cation into much more complicated structures. This method of structural determination can indeed be applied to other complex materials.

It has been shown that in the duration of this project that high resolution electron microscopy is invaluable in the structural determination of both microporous and mesoporous materials. The identification of pore diameters ranging from 2-20nm is of particular interest to many workers in this research field.

It is shown that direct observation of these systems at sub-nanometer resolution and of loaded nanoparticles within is potentially of great value in the understanding and therefore the manipulation of these structures.

It was concluded that the observation of certain nanoparticles directly loaded into the porous channels could lead to problems, however HRTEM (High Resolution Transmission Electron Microscopy) had sufficient resolution to allow the determination of the size and location of these particles. Chemical analysis using EDS was used to identify and quantify the loaded metal within the pore channels or in many cases out with the target region in these materials. It was shown that scanning electron microscopy is a more than valuable tool in the study of morphology and elemental analysis from many solids.

SECTION ONE – HRTEM OF SOLIDS

Chapter 1. Introduction

1.1 $BaBiO_3$ System

This system was chosen as the solid solution as a great deal of research has focused on $BaBiO_3$ as the forerunner compound to two superconductors ($Ba_{1-x}K_xBiO_3$) and ($BaPb_{1-x}Bi_xO_3$), both derived from the compound $BaBiO_3$ (*Matheiss et al 1988).*

$BaBiO_3$ is a semiconductor although band theory states this material should be a metal because of its 6s band (*Sleight et al 1975).* This band is energetically unstable and $BaBiO_3$ undergoes a structural transition leading to a charge ordered insulating state. $BaBiO_3$ is a distorted form of perovskite. An ideal perovskite structure is shown in (*Fig. 1.1).*

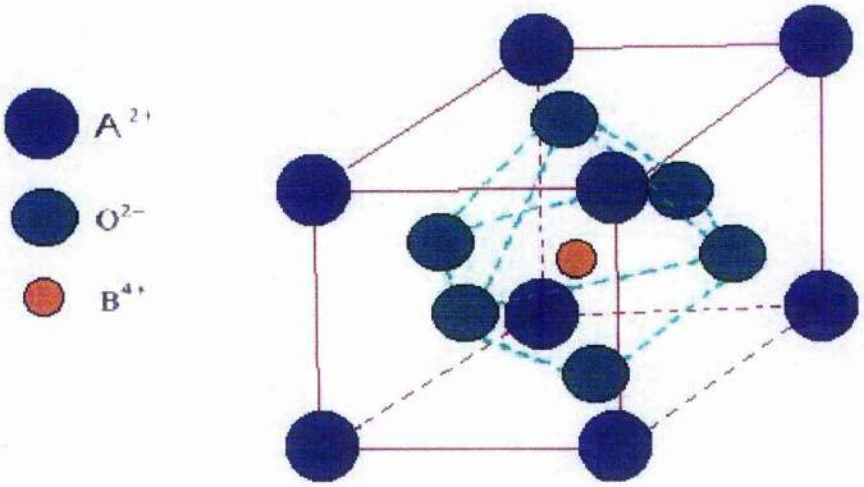

Fig. 1.1 Ideal perovskite structure (ABO_3).

Perovskite compounds have a general formula ABX_3, where A and B are cations in crystallographically distinct sites, and X is usually O^{2-}. The structure is made up of cubic closed–packed layers with AX_3 composition. The smaller B cations occupy the octahedral interstices that are co-coordinated by six anions. This arrangement can lead to $BaBiO_3$ having very surprising electronic properties. If $BaBiO_3$ contains Bi^{3+} and Bi^{5+} the material is semiconducting. On the other hand if all the Bi cations have uniform valence, Bi^{4+} has configuration 6s1, and a half filled 6s band should exist in $BiBaO_3$, with metallic properties expected (*Wells 1962).*

$BaBiO_3$ has been proposed to have a mixed valence, where the electrons are localized in pairs at the Bi (III) sites, which make up one half of the B-sites. The remaining sites can be classed as Bi (V) so that the compound can be formulated as $Ba_2Bi(III)Bi(V)O_6$. This falls into the Class I of mixed valence compounds as classified by *Robin and Day* in 1967.

Neutron diffraction studies have revealed that the $BaBiO_3$ structure has monoclinic symmetry (a=6.18Å, b=6.14Å, c=8.67Å, and β= 90.173°) (*Cox and Sleight 1976, Thornton and Jacobsen 1978)* at room temperature. This unit cell can be regarded as a $\sqrt{2}$ x $\sqrt{2}$ x 2 supercell which is derived from the ideal perovskite unit cell. This transforms to rhombohedral at 130°C, and cubic at 500°C (*Cox and Sleight 1979).* Data at room temperature suggested the existence of two different Bi sites, which possess different average Bi-O bond lengths, and therefore two distinct Bi charges. These are ordered so that one Bi^{3+} site is surrounded by six Bi^{5+} bridged by oxygen anions and vice versa.

The valence state(s) of Bi in $BaBiO_3$ has been the subject of debate. On the one hand Bi (IV) has never been observed in oxides, however the octahedral co-ordination of Bi (III) does not correspond to previous observations, where it takes up less symmetrical environments. A number of techniques have been applied to try and clarify this matter.

The neutron diffraction data gives some evidence for the disproportionation and ordering of Bi (III) and Bi (V), which can be described as a charge density wave on the B-sites. Bond length-bond strength correlations were applied to these two sites, this confirmed a difference in the charge of the two, this was not enough to represent complete disproportionation into Bi (III) and Bi (V) (*McGuire and O'Keefe 1984).* Further neutron diffraction of various samples of $BaBiO_3$ under different conditions were prepared (*Chaillout, et al 1988).* Those samples heat treated above the rhombohedral-cubic structural transition temperature showed little difference in Bi-O bond lengths, whereas those treated at lower temperatures showed two average bond lengths. The effective valancies were calculated for the two sites as being about 3.5 and 4.5 and it was concluded that only 75% ordering of Bi^{3+} and Bi^{5+} existed. For samples prepared at high temperatures, 100% disordering (or a random arrangement) of Bi^{3+} and Bi^{5+} was proposed, which would lead to the *average* cubic structure observed.

X-ray photoelectron spectroscopy has been widely used to look at the Bi core energy levels, which reflect the valancies present in the material (*Orchard and Thornton 1977, Wertheim et al 1982, Hedge et al 1989).* Results show a significant broadening of the Bi

(4f) peaks for surface cleaned (in vacuo) samples, but these signals could not be resolved unambiguously into the two components expected from the crystal structure. It has been proposed that, rather than containing mixed valent Bi, $BaBiO_3$ possesses mixed valent O^{2-} and O^{-} ions (*Hedge et al 1989*).

The initial proposal of an antiferromagnetic arrangement of Bi (IV) as an explanation of semiconductivity in $BaBiO_3$ (*Nakamura et al 1971*) has been rejected by a muon spin rotation study, which finds no evidence of magnetic order in $BaBiO_3$ (*Uemura et al 1988*).

There remains however strong evidence for some charge disproportionation in $BaBiO_3$, even in the metallic phase. Alternatively, the two different bond lengths observed could arise from distortions of the BiO_6 octahedra, however this difference within an octahedron is small compared to the difference in average Bi-O bond lengths between Bi^{3+} and Bi^{5+} (*Boyce et al 1991, Boyce and Sleight 1991*).

It seems therefore that in the metallic phase, there is a tendency for the Bi to disproportionate, perhaps on a local scale, so that two adjacent Bi sites become 3+ and 5+, but an isolated Bi remains as 4+ and contributes to the conduction band *(Sakuma et al 1990)*. Electrons are localised by Anderson-type disorder at Bi^{3+} sites. This band splits into two discrete bands at the metal–insulator transition, representing the complete localisation of electrons at Bi^{3+} sites and the consequent disappearance of the itinerant Bi^{4+} states.

1.2 Mesoporous solid solutions

Microporous zeolitic molecular sieves such as zeolite A, zeolite Y, synthetic aluminosilicates ZSM-5, ZSM-11 and the aluminophosphate family are all crystalline materials which have been widely used as catalysts and sorbents for oil refining and production of petrochemicals (*Breck et al 1974*). These materials have a very high surface area and therefore high adsorption capacity *(Zhou 1999)*.

Porous solids can be classified as either microporous (pore width up to 2nm) or mesoporous (pore width 2-50nm) *(McEnaney et al 1997)*. The size of the channels and cavities in microporous materials allows them to present a high selectivity of desired chemical reactions. However microporous materials are of limited application in chemical processes where large molecules are involved. Therefore, there is an increasing demand for molecular sieves with pore diameter in the mesopore (2-20nm) range for use

in the production of fine chemicals consisting of large molecules. The discovery of the new family of synthetic mesoporous silicates, known as M41, by the Mobil scientists Kresge and Beck opened a new territory of research field in materials science. These possess regular pores of size 1.5nm to 10nm range and exhibit:

1. Well-defined pore size and shape,
2. Possibility of fine tuning the pore aperture, which makes them of interest to heterogeneous catalysis,
3. It is thought to have high thermal and hydrolytic stability, although there is still some debate regarding this,
4. High degree of pore ordering over micrometer length scales,
5. Excellent thermal insulation and sound proofing qualities.

A typical mesoporous molecular sieve is MCM-41 (*Fig. 1.2*), which has a 1-D pore system.

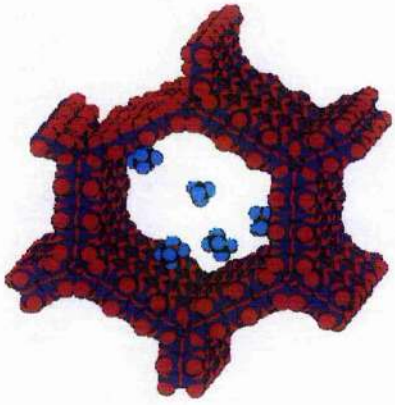

Red=Oxygen, Blue=Silicon,
Light Blue=Hydrogen, Brown=Carbon

Fig. 1.2 Methane and ethane inside one of the hexagonal pores of molecular sieve MCM-41 (of about 3 nm pore diameter).

The most popular formation mechanism is the so called liquid-crystal templating mechanism (LCT), this was first postulated by the Mobil scientists *Kresge, et al 1992, Beck, et al 1992* and later supported by other groups including *Zhou and Klinowski 1998.*

The two main reagents used in the synthesis are surfactant and a silica source. Surfactants are bifunctional molecules that contain a solvent loving (lyophilic) head group and a solvent hating (lyophobic) tail (i.e. they are amphiphiles), such as alkyltrimethylammonium salts. Two possible pathways were proposed for the LCT mechanism. One is that the surfactant molecules form hexagonal arrays of micellar rods, acting as the template. Silicate species are deposited between surfactant tubules to form

the inorganic framework. In the second, the interaction of the silicate species with the surfactants mediates the hexagonal ordering *(Raman, et al 1996)*. Both result in an assembly of silicate ions on the surfaces of the surfactant rods, which are in the form of hexagonal liquid crystals *(Zhou, et al 2000)*.

The organic compounds are removed by calcinations and mesoporous silica forms. The most popular mesoporous phase, MCM-41 (Mobile Crystalline Material), forms with all the mesopores along the c-axis and a hexagonal symmetry on the (ab) planes. It has therefore a 2-dimensional structure with a=b, c=∞, α=β=90° and $\gamma = 120°$. The most suitable space group determined from XRD is P6m *(Tolbert, et al 1997)*.

The pore diameter in MCM-41 can be controlled by the length of the surfactant molecules used in the reaction, for example the n value in $C_nH_{2n+1}(CH_3)_3NX$. When n changes from 8 to 18 the pore size in the product increases from 1.5 to 4.5nm *(Beck, et al 1992, Luca, et al 1995)*. To further define the pore size auxiliary organics can be added *(Kresge, et al 1992, Beck, et al. 1995, Cheng, et al 1997)*.

The formation mechanisms of other mesoporous materials are similar to that of MCM-41 except that different liquid crystal phases form in different conditions. For example the cubic phase, which consists of two interweaving non-intersecting channels, is formed in a solution with a high ratio of surfactant/silica, which is an analogue of a lytropic liquid crystal.

Others can be synthesised using so called Gemini quaternary ammonium surfactants as templates and can be considered to be derived from a hexagonal close packing of globular surfactant/silica arrays *(Rist et al 2001)*.

The examination of these materials by XRD is difficult, and limited information can be gained. Strictly speaking they are not crystal. In a typical pattern gained by XRD only very few peaks are evident at the low angle range and extremely weak peaks at the high angle 2θ range. As a consequence of this an examination of the local structures of these materials by XRD is impossible. HRTEM is however a good technique to reveal the detailed structures of mesoporous materials.

1.3 Aims

Continuous studies including electron microscopy over a range of $Ba_{1\pm x}Bi_{1-x}O_3$ compositions have been carried out. $BaBiO_3$ has many interesting and important properties and characteristics, for this reason it is a very suitable solid for close inspection

using high resolution electron microscopy (HRTEM) and its related techniques. Electron microscopy has emerged to become the most powerful and versatile tool to study the detailed structures of materials, to identify new or known phases and to gain information on composition. Imaging and electron diffraction are usually employed together in transmission electron microscopy.

Analytical electron microscopy is the most sophisticated tool available for micro structural analysis. Using this method, we can obtain both the detailed structures of $BaBiO_3$-related materials and also their elemental compositions. This is also the best technique to obtain local elemental composition of small regions of a heterogeneous solid. The most important aspect of electron microscopy in solid state chemistry is in its ability to elucidate problems that are beyond the capability of X-ray or neutron crystallography. High resolution microscopic images show local structures of crystals in remarkable detail. Ultra microstructures of imperfections are readily seen in these images. Selected area electron diffraction along with imaging can often reveal atomic arrangements in regions containing only a few atoms. HRTEM is also very useful in identifying new phases, some often occurring in one or two rows or layers as imperfections or as intergrowths in other phases.

To determine the microstructures of $Ba_{1\pm x}Bi_{1\mp x}O_3$ solids of different chemical structure and behaviour using various techniques. These techniques include HRTEM imaging, energy dispersive X- ray analysis (EDS), selected area electron diffraction (SAED) and powder X-ray diffraction (XRD). It will be assumed that the oxygen content is 3 for all compositions. The oxygen content cannot be determined however the standard is perovskite with formula $BaBiO_3$ and all compositions are based on this. It will also be demonstrated that HRTEM is a major player into the investigation of some typical mesoporous molecular sieves.

It is hoped to show conclusively that this technique can give us structural information, which could not be gained from any other experimental procedures.

Chapter 2. Experimental

2.1 Synthesis of $BaBiO_3$-based solid solutions

All solid solutions of $Ba_{1\pm x}Bi_{1\mp x}O_3$ with differing ratios of Bi/Ba were synthesized using the following two reagents:

1. $BaCO_3$ (Barium Carbonate) Aldrich, purity-99.98%
2. Bi_2O_3 (Bismuth Oxide) BDH, purity- not less than 99%

For the standard and the Ba-rich solid solutions stoichiometric amounts of $BaCO_3$ and Bi_2O_3 were ground together in acetone: The mixture was then pressed into a pellet, placed onto an aluminium boat on gold foil and heated in a tube furnace at 820°C for 48 hours with flowing pure O_2 using a slow heating ramp of 5°C per minute. The pellet was quenched to room temperature after 48-hours heating while still under flowing O_2.

For Bi rich samples the appropriate quantities of $BaBiO_3$ and Bi_2O_3 were ground together in acetone, dried and pressed into pellets. They were then fired at 820°C for 12 hours in flowing N_2 gas, and cooled to 100°C. Without removing the samples, the gas was changed to O_2, and the pellets annealed at 420° C for 4 hours.

2.2 Powder X-Ray Diffraction

Powder x-ray diffraction is a versatile, non-destructive analytical technique for identification and quantitative determination of the various crystalline forms known as "phases" of compounds present in powdered and solid samples.

One method of identification can be achieved by comparing the x-ray diffraction pattern or diffractogram, obtained from an unknown sample with an internationally recognized database JCPDF, containing reference patterns for more than 70,000 phases. Alternatively the d–spacing of each peak position can be calculated and thus the possible unit cell parameters. Modern computer controlled diffractometer systems use automatic routines to measure, record and interpret the unique diffractograms produced by individual constituents in even highly complex mixtures.

The source of the X-rays in the Philips diffractometer is Cu Kα produced by bombarding copper metal with electrons, the wavelength of which are smaller than the interplanar distances of the crystal planes. The Philips diffractometer was used along with the Philips Xpert and Stoe winXPOW software. Powder diffraction patterns consist of a pattern of peaks, which result from constructive interference of X-rays diffracted by atoms in the various hkl planes. From the information that is given certain questions can be answered:

1. *Which phases are present?*
2. *At what concentration levels?*
3. *What is the amorphous content of the sample?*

To ascertain the phases present one must observe the peak positions, for phase concentrations peak heights must calculated, amorphous content is evident by the background hump and crystalline size by peak widths. In any crystal, planes exist in a number of different orientations, each with its own specific d-spacing, which is the distance that parallel planes are separated from one another.

Braggs Law

Bragg's law states that $n\lambda=2d\sin\theta$ when the monochromatic x-ray beam with wavelength λ is incident on lattice planes in a crystal at an angle θ. Diffraction occurs only when the distance travelled by the rays reflected from the successive planes differs by a complete number n of wavelengths. By varying the angle θ the Bragg's law conditions are satisfied by different d-spacings in polycrystalline materials. Plotting the angular positions and intensities of resultant diffraction peaks produces a pattern, which is characteristic of the sample. Where a mixture of different phases is present the diffractogram is formed by the addition of individual patterns. Resultant XRD measurement shows:

1. *Phase present-peak positions.*
2. *Phase concentration-peak heights.*
3. *Amorphous content-background hump.*
4. *Crystalline size/strain-peak widths.*

2.3 High resolution transmission electron microscopy

2.3.1 Energy Dispersive X-ray Analysis

When a beam of electrons hits a sample the generation of X-rays occurs. Each element has a characteristic X-ray emission spectrum, by monitoring the energy and the intensity of the emitted X-rays; an elemental analysis can be formed.

In a sample containing two elements, as in the samples studied in this report, (Bi, Ba) the concentration of each element (C_x and C_y) can be calculated from the Cliff-Lorimer approximation when the specimen is very thin, *(Myklebust et al 1981)*.

$$\frac{C_x}{C_y} = K_{xy}\frac{I_x}{I_y}$$

where I_x, I_y are the X-ray intensities of the elements and K_{xy} is a constant determined from a standard material containing x and y.

In a thick specimen three main effects can occur that may limit emission of X-rays from a specimen:

1. Atomic Number (Z) effect; The X-ray intensity per unit concentration increases with Z. Therefore, if the mean atomic number of the standard differs from the sample, it must be accounted for in the correction.

2. Absorption (A) effects; X-rays produced at depth must pass through a certain distance within the sample and risk being absorbed.

3. Fluorescence (F) effect. The *critical excitation energy* (E_c) of an element is the energy threshold needed to initiate inner sphere ionisation and generate characteristic X-rays.

For calculating the concentration of element x:

$$Cx = \frac{KxIx}{CzCaCf}$$

where K_x is a constant obtained from a standard and Cz, Ca and Cf are correction factors for the effects of atomic number, X-ray absorption and X- ray fluorescence. This is known as the ZAF correction *(Armstrong 1988)*.

To do the ZAF correction,

1. The specimen must be thick enough to absorb all the incident electrons,

2. The chemical composition must be known,

3. The total number of atoms in the whole region where X-rays are emitted must be known.

This is used only on thick specimens such as those used in SEM. We do not actually do the ZAF calibration; this has been included in the software of the EDS analysis. For SEM EDS the specimen should ideally be flat and polished, this is not possible with powder samples and the results should take this into consideration. Resolution of the chemical analysis is also limited by its maximum voltage i.e.: 30kV as opposed to 200 kV for the HRTEM. The HRTEM chemical analysis using EDS therefore has high energy resolution over a small spatial area.

All the EDX analyses of the $BaBiO_3$-related solid solution specimens were performed on a Jeol JEM-2011 high resolution TEM operated at 200kV, tilting angle ± 20° with Oxford Link ISIS Semi STEM microanalysis system. Samples were ground in acetone and air dried onto a carbon coated copper grid. The specimen once inserted into the microscope was then tilted +18° in the X direction to-wards the detector. Thirty crystals for each sample were analysed and the ratio of Bi:Ba calculated for each. For each element the L series line was used in quantification for Ba and Bi as there was a strong absorption factor in the M series line for Bi in the spectrum. A typical EDS spectrum is shown in (*Fig. 2.1).*

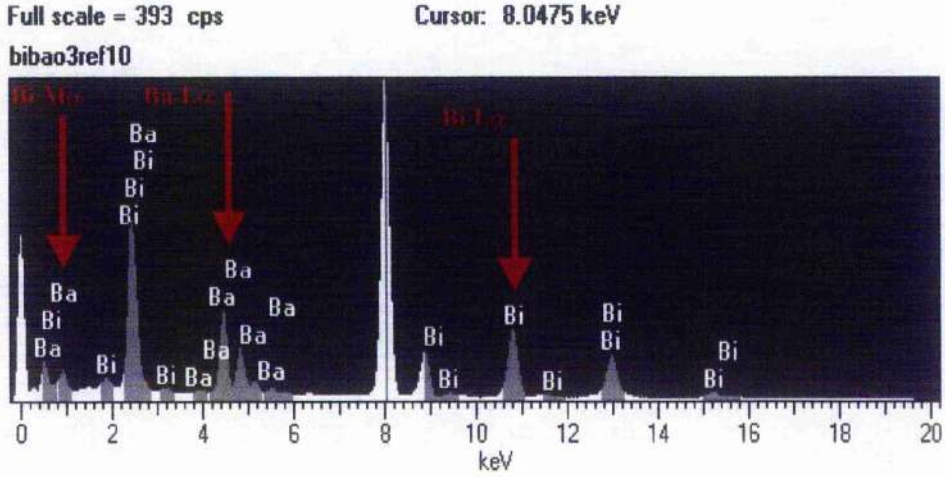

Fig. 2.1 Typical EDS Spectrum for $BaBiO_3$ standard sample.

2.3.2 Selected Area Electron Diffraction. (SAED)

A beam of electrons can be considered to have wave like behaviour and will be diffracted from lattice planes in a crystal. In an electron microscope a beam of electrons is accelerated towards a sample and the resultant electron diffracted beam produces both a diffraction pattern and an image of the sample.

The wavelength of accelerated electron in an electron microscope could be very short, *e.g.* when the accelerating voltage V = 200 kV, λ = 0.0251 Å. When the electron beam passes through a crystalline specimen, it is scattered by the crystal planes defined by (*h k l*) according to Bragg's law

$$2d\sin\theta = n\lambda$$

where *d* is the *d*-spacing of the crystal planes, *n* the order of reflection and θ the angle of incidence (Bragg angle). If $d_{(h\,k\,l)}$ = 5 Å, *n* = 1, λ = 0.0251 Å, the Bragg angle, θ, is then 0.14°, which is significantly smaller than that in a conventional X-ray diffraction beams (*Fig. 2.2*).

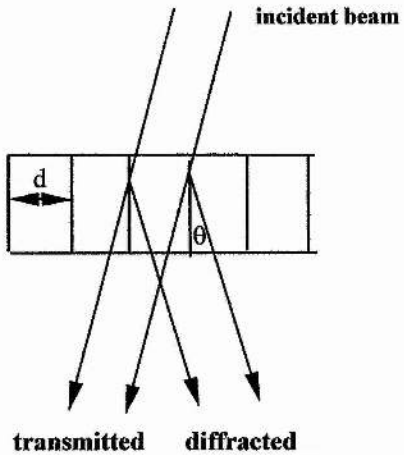

Fig. 2.2 Schematic drawing of an electron beam diffracted by a crystal.

Both transmitted and diffracted beams are focused by the objective lens to the back focal plane. The beams diverge and form a magnified image of the object in the intermediate image plane. Below this plane, two modes of operation (imaging and diffraction) are possible *(Fig. 2.3)*.

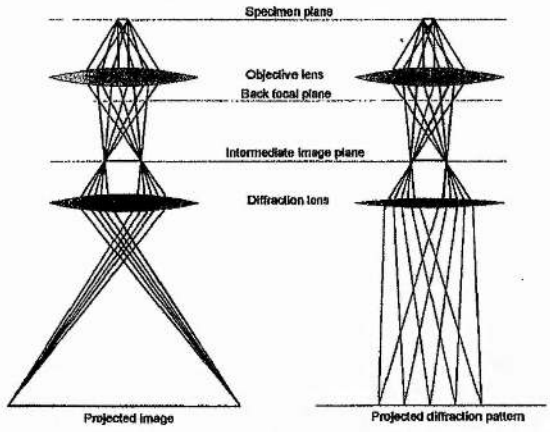

Fig. 2.3 Electron microscopy, modes of operation (imaging and diffraction)

In the image mode, the lower lens magnifies further the intermediate image onto the fluorescent screen. When a weaker lens is used underneath the intermediate image plane, the electron wave front in the objective back focal plane is projected onto the screen. We now have the diffraction mode.

One of the advantages of electron microscopy is that a very small area of the solid can be examined. An aperture, inserted into the intermediate image plane, enables us to collect beams scattered only from a small area in the specimen. This operation is called Selected Area Electron Diffraction (SAED), *(Weirich 2004)*.

Calculation of the SAED patterns can be achieved by the following relation:

$$d^* = 2\sin\frac{\theta}{\lambda} = \frac{D^*}{L\lambda}$$

In electron diffraction the wavelength is very small ($\lambda = 0.0251$ Å for an accelerating voltage of 200kV). The angle of incidence θ is also very small $\theta<1°$. The perpendicular distance from the sample to where the un-diffracted electron beam is focused is called the effective camera length L. To obtain an accurate camera length, calibration using a standard crystal should be carried out. The distance measured from the central spot (000) to another given spot is D* (enlarged reciprocal d-spacing, d*) in the above equation. The d-spacing acquired can then be compared with the d space given by the XRD to index the diffraction spots. Two or more patterns are needed to reveal a 3D unit cell. This is because an SAED pattern only gives a magnified 2D reciprocal lattice. By recording two or more SAED patterns along various zone axes from the same crystal by tilting, one can combine to give an enlarged 3D reciprocal lattice *(Somorjai 1981)*.

The sample was first studied in transmission mode until a thin crystal of reasonable size and over a hole in the film was found. The appropriate selected area aperture was then inserted and the microscope switched to diffraction mode. The crystal was then examined in diffraction mode until a possible face of the reciprocal unit cell was obtained. The crystal was then tilted to obtain more inter-planar spacings at different angles. Two-dimensional projections of the sides of the reciprocal unit cell could be drawn from these measurements.

2.3.3 High resolution imaging

Unlike X-rays and neutron diffraction, focusing of an electron beam can be achieved using electromagnetic fields, thus magnified images of objects may be produced in a similar way as with light but with much higher resolution due to a shorter wavelength. *Fig. 2.4* is a HRTEM image obtained from a sample of $BaBiO_3$ in the [111] projection with magnification of 800,000X. The black dots correspond to columns of atoms.

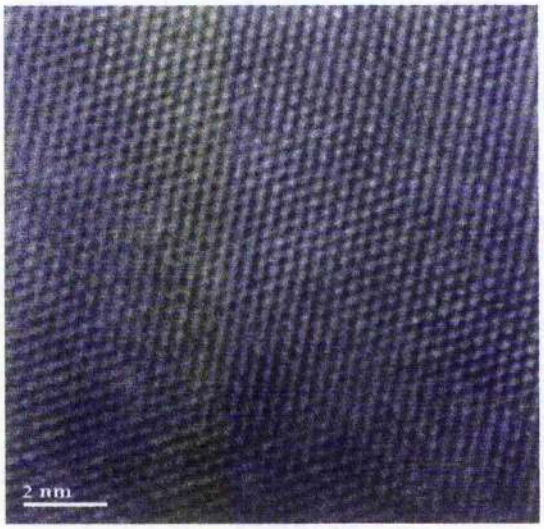

Fig. 2.4 Image of $BaBiO_3$ in the [111] projection.

The resolution in HRTEM is governed partly by the electron wavelength and the optical characteristics of the objective lens. The most important part of the latter is the spherical aberration, this introduces a phase difference into the individual diffracted beams and when the real image is synthesized by the lens from these diffracted beams this can give confusion in the image contrast.

Spherical Aberration

Consider two rays emanating from the point Q, one along the optic axis and one at a scattering angle α (generally of the order of 10 milliradians) (*Fig. 2.5*). The latter will reach the lens a distance R from the centre of the lens, where $R = a\alpha$. If the lens is perfect, these two rays should intersect at a point P. If spherical aberration is present, the non-axial ray reaches the Gaussian image plane at the point P_2, an amount Δr from the optic axis, where Δr is the radius of the disc of least confusion, given by: $\Delta r = MC_s\alpha^3$, where $M = b/a$ is the magnification of the lens and C_s is the coefficient of spherical aberration *(Smith 2000), (Conrady 1985)*. The angular deviation of the non-axial ray can be expressed as the angle ε_s which may be written:

$$\varepsilon_s = \frac{\Delta r}{b} = \frac{MC_s\alpha^3}{b} \approx \frac{C_s R^3}{F^4} \text{ if } a \approx F, \text{ F being the focal length of the lens.}$$

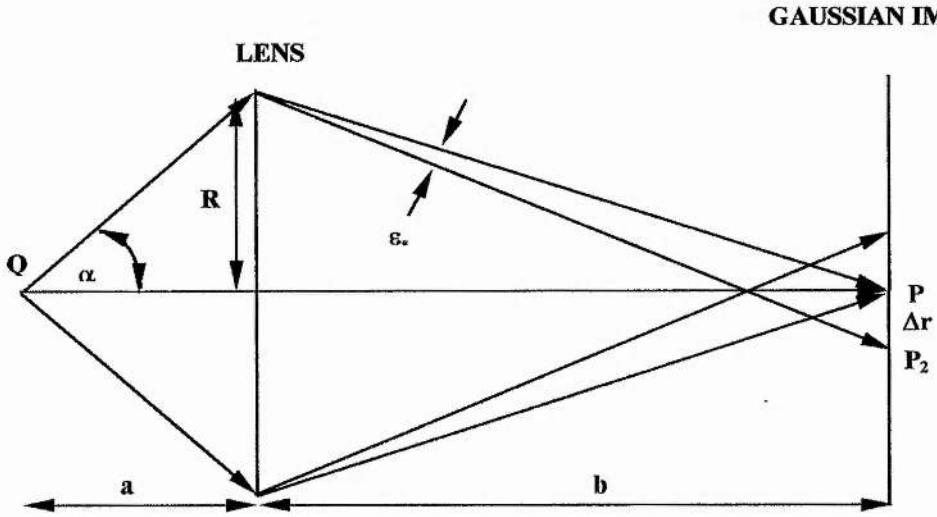

Fig. 2.5 A ray diagram showing spherical aberration.

Consider two non-axial rays, (*Fig. 2.6*) one distant R from the centre of the lens and one distant R + dR. The path difference between the two (corresponding to P and P_2, respectively), ds, arises from the extra deviation ε_s and is given by:

$ds = \varepsilon_s dR$

The total path difference $W_s(\alpha)$ between the non-axial ray and the one along the optic axis is

$$W_s(\alpha) = \frac{2\pi}{\lambda}\Delta = \frac{2\pi}{\lambda}\int_0^R ds = \frac{2\pi}{\lambda}\int_0^R \varepsilon_s dR = \frac{2\pi}{\lambda}\int_0^R \frac{C_s R^3}{F^4} dR = \frac{2\pi}{\lambda}\frac{1}{4}\frac{C_s R^4}{F^4} = (\frac{2\pi}{\lambda})\frac{1}{4}C_s\alpha^4$$

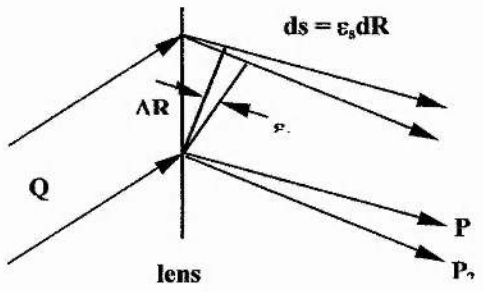

Fig. 2.6 Ray diagram showing path difference introduced by spherical aberration.

Phase Contrast

Electron scattering can be described as the diffraction of electron waves. If the interference of diffracted waves produces differences in intensity at the image, phase contrast is generated. Electrons scattered through large angles may fall outside the lens aperture, giving rise to amplitude contrast. Ideally, all other scattered electrons will be focused by the lens at the corresponding image points, they arrive in phase. At planes above or below the ideal image plane, interference produces differences in intensity. These differences consist of the focus (Fresnel) fringes. Because of lens aberrations, a slight phase contrast is produced by a combination of defocusing and lens aberration.

Phase contrast in images arises from differences in phase between scattered and un-scattered rays in different parts of the image and interference between these rays. In a fully transparent (i.e. no variation in refractive index) object, there are no phase differences and, hence no phase contrast in the image. Defocusing, in which path lengths for scattered rays are changed more than for the un-scattered rays, can be used to enhance phase contrast. Contrast due to phase differences is more important for thin objects and when working near the resolution limit than contrast due to amplitude differences.

Defocus or phase contrast results in the formation of strong Fresnel fringes about any part of the specimen where there is a rapid change in mass thickness. The fringes serve to enhance such points or edges by delineating them with a bright line in the under-focused position (objective lens too weak) or with a dark line in the over-focused position (objective lens too strong). The Fresnel fringes virtually disappear at the point of "exact" focus and image contrast due to phase effects is at a minimum. It is common practice with thin specimens studied at high resolution to defocus (under-focus) slightly to improve image contrast. At slight over-focus the image is generally confusing. Initially, at slight defocus, resolution is not significantly reduced, but further defocusing reduces resolution considerably *(McCartney et al 1996)*.

Chromatic Aberration

Chromatic aberration has two main causes, the primary one being a fluctuation in the energy of the electrons leaving the filament. This arises from slight fluctuations in the accelerating voltage (ΔV) and variations in the electron energies due to thermal effects (ΔE). Both of these effects cause minor variations in the scattering angle for a given diffracted beam and also change the focal length of the objective lens *(Van Dyck et al 2003)*. The second cause of chromatic aberration lies in fluctuations in the current of the objective lens coil (ΔI). This also changes the focal length of the lens. Consequently, all three effects give a focal spread for the microscope, δF.

Beam Divergence

The divergence of the electron beam *(Fig. 2.7)* or spatial incoherence, also limits the ultimate resolution of the microscope. The real electron source is never an infinitely small point, i.e. the incident beam is not exactly parallel, but forms a cone on the specimen. Consequently, the image observed is an average over a small circular range of beam inclination angles. Therefore, an amount of such inclination, δS, has to be included in the calculation of the diffracted amplitude and the intensities of the image.

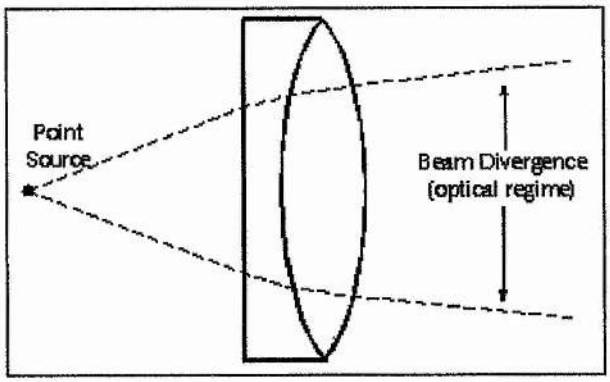

beam divergence

Fig. 2.7 Schematic drawing showing beam divergence.

The Multislice Approximation

The limitations in resolution of the imaging system of HRTEM lead to detail loss, which is usually caused by multiple scattering within the specimen. A model can be proposed from the observed image and a computer simulation of the multiple scattering. The model is adjusted until the computer created images from it match the experimental HRTEM images. The multi-slice approximation is the most common method used by software, *(Cowley and Moodie 1957)* including the MacTempas software package in the Department of Chemistry, University of St Andrews.

Fig. 2.8 represents the crystal in the multi-slice approximation. The crystal is cut in the direction perpendicular to the incident electron beam into slices of the thickness of the order of one atomic layer. For each of the slices the crystal potential is projected to a plane. The electrons propagate in the "layers" of vacuum on very small distances and under very small angles. Subsequently they are diffracted on the planes of the potential projected on very small distances and thus only slightly influencing the wave function.

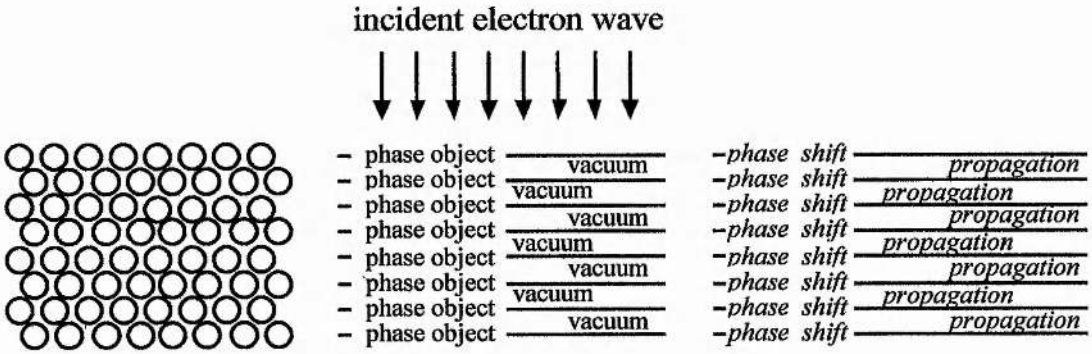

Fig. 2.8 Model representing the multislice approximation

The high resolution images in this report were taken with the Jeol JEM 2011 TEM operated at 200kV, resolution 0.194nm. The smallest beam diameter is 0.5nm. Magnification is up to 1,500,000x. The images can either be recorded on film or more usually as in this project a Gatan 794 CCD camera system with a high sensitivity detector, which enables the user to record high quality digital images.

Chapter 3. Results and discussion

3.1 $BaBiO_3$

$BaBiO_3$ was used as the standard material to which all subsequent samples were compared. The structures and properties of $BaBiO_3$ have been well documented and the current literature on the compound was used as a reference.

Stoichiometric amounts of $BaCO_3$ and Bi_2O_3 were ground together in acetone; the powder appeared to be yellow at this point. The mixture was then pressed into a pellet, placed onto an aluminium boat on gold foil and heated in a tube furnace for 48 hours at 820°C with flowing pure O_2. A slow heating ramp was introduced of 5°C per minute. It was hoped pure O_2 would eliminate the chance of oxygen vacancies occurring and therefore false results. After heating the sample was cooled slowly, at this stage it appeared gold/brown.

The sample was then ground with mortar and pestle and run on the Philips diffractometer for X-ray diffraction study. Powder XRD patterns were collected initially for fingerprinting purposes in order to firstly determine which compositions had formed single phase perovskite material. The peaks in XRD pattern gained in *Fig. 3.1* were initially indexed into the cubic unit cell with a = 4.3Å and the specimen seems to be monophasic perovskite.

This X-ray pattern and all subsequent patterns for both the Ba rich and the Bi rich samples were collected over a period of one hour from starting point of 5 two-theta to an end point of 90 two- theta on the Philips PW 1710 diffractometer. The parameter settings for each run were set as one degree per minute and each run having a step size of 0.02. Each pattern was collected in a file format called UDF; this is the Universal Diffraction Format. This is a format that can be easily converted to another file format of the users choosing. In this case the UDF file was converted to a RAW file. This format can be used with the Stoe WinXpow software to obtain peak intensities, peak positions and D spacing results.

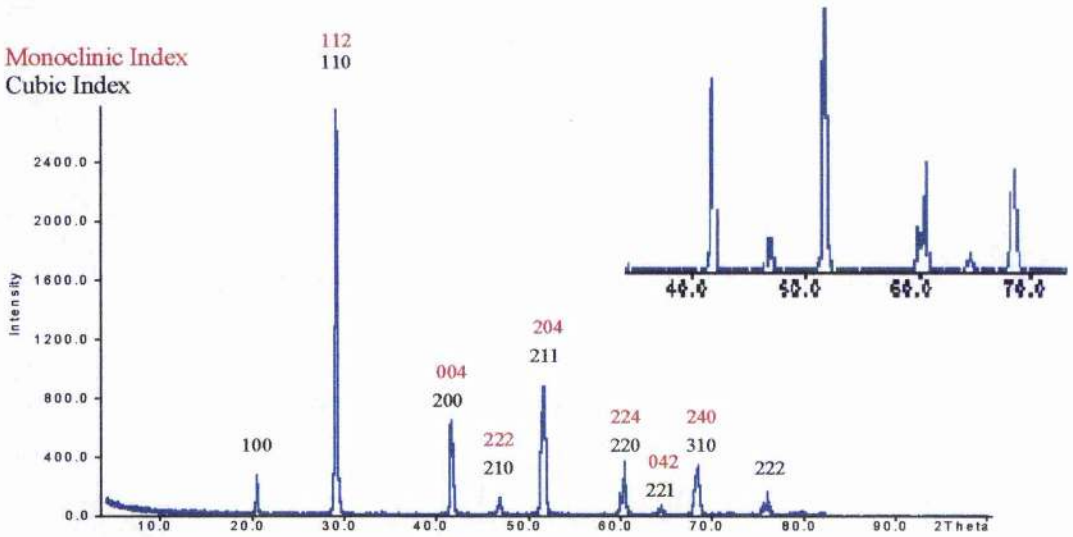

Fig. 3.1 XPD pattern of $BaBiO_3$ at room temperature.

However a close look reveals that the pattern in *Fig. 3.1* shows the reflections from the pseudocubic unit cell are split (inset). This could be due to symmetry tending towards monoclinic a=6.1814, b=6.1360, c=8.661Å and β= 90.173°, rather than cubic although this is not a certain as two peaks (100) and (222) cannot be indexed to monoclinic symmetry. The evidence given from the XRD pattern leads us to believe that the sample is truly single-phase perovskite material since all the peaks have been indexed. The peaks signature, the $\sqrt{2}a_p \times \sqrt{2}b_p \times 2c_p$ cell is present in the $BaBiO_3$ standard. The sample appears to be pure as well because there is no amorphous background hump in any of the patterns.

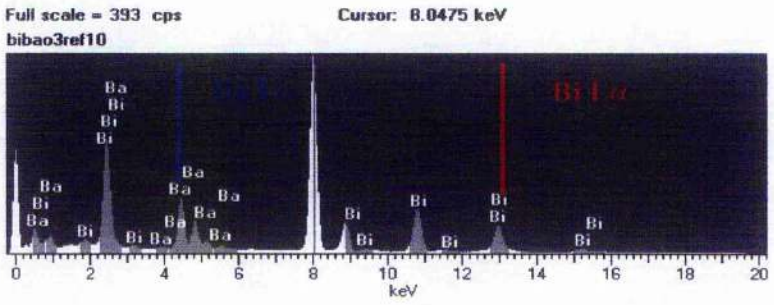

Fig. 3.2 Energy Dispersive X-ray Analysis spectrum for $BaBiO_3$

The EDS spectrum of $BaBiO_3$ obtained from the ISIS microanalysis software is shown in *Fig. 3.2*. The Lα line was chosen for the analysis for both Bi and Ba

calculations, as it was more reliable than the M line, having less absorbance problems. 20 particles were finally used after "rogue" particles were discarded from the final results. The calibration constant for the standard sample $BaBiO_3$ was determined to be $K_{Bi/Ba}$=0.69±0.02. This value was obtained by first measuring Bi Lα and Ba Lα I (peak intensities), and calculating K (calibration constant), using this value the ratio of Bi/Ba for all subsequent samples was calculated. 20-30 particles for each sample were analysed of which 20 were selected for the final analysis. "Rogue" results with high margins of error were discarded. This system was adopted for all compositions. The ratio for Bi/Ba in a known sample of $BaBiO_3$ is by definition 1.0.

Selected area electron diffraction studies were then undertaken with the Jeol JEM 2011 TEM on the standard material to confirm the presence or the absence of superstructure and to determine the reciprocal lattice pattern of the perovskite structure. *Fig. 3.3* shows the initial patterns with the electron beam parallel to the [-111] and [1-2-2] directions, indexing of the spots is based on a pseudocubic primitive cell ($a \approx 4.35$Å). These patterns are compatible with a unit cell based on the primitive perovskite cell. No extra superlattice diffraction spots were present.

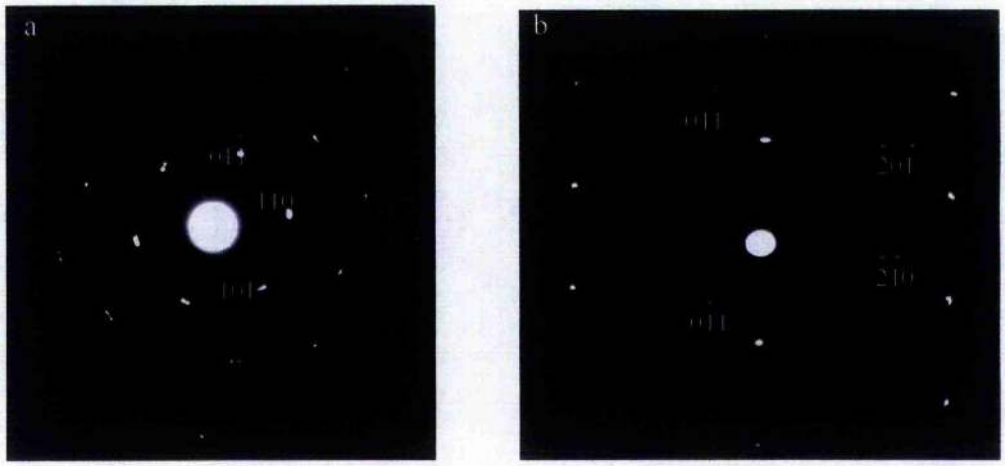

Fig. 3.3 SAED patterns of $BaBiO_3$ viewed down the (a) [-111] and (b)[1-2-2] projections.

High-resolution images of the microstructure of the $BaBiO_3$ standard were taken, once again these were to show structure consistent with that expected of a simple

pseudocubic perovskite structure. *Fig. 3.4* shows a typical image when the beam is parallel to the [111] direction.

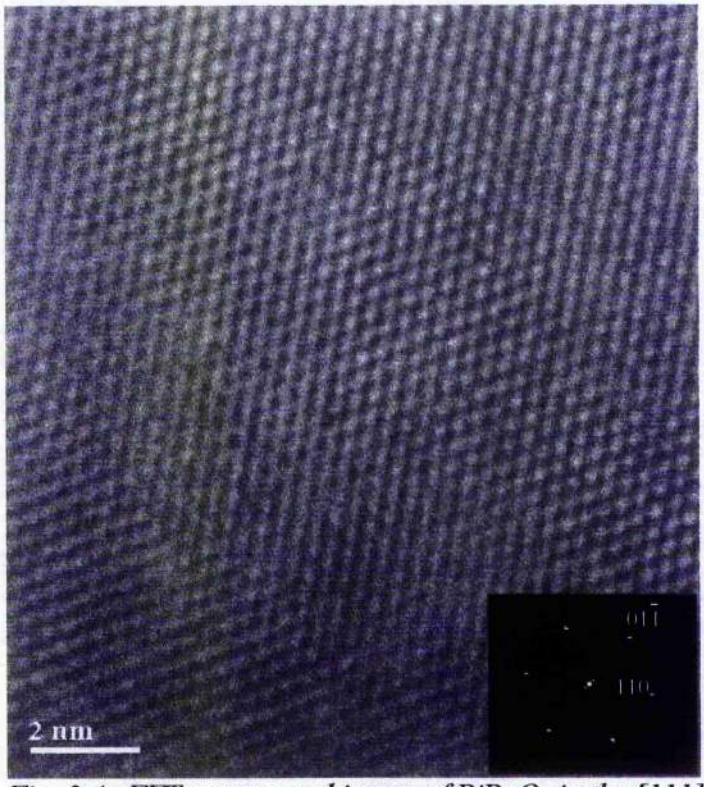

Fig. 3.4 FFT pattern and image of $BiBaO_3$ in the [111] projection.

3.2 $Ba_{1.1}Bi_{0.9}O_3$

The sample was prepared as described above, quenched under flowing O_2, as it was thought that Ba rich samples are not as stable as the standard. The appearance of the sample after firing was of a dark brown powder.

The XRD study of this material (*Fig. 3.5)* shows very little change to that of the basic perovskite structure for the standard sample. The peak splitting may be greater than in the standard sample indicating a lowering of symmetry, no extra peaks are observed however and all seem to be of the same intensity as those observed for the standard.

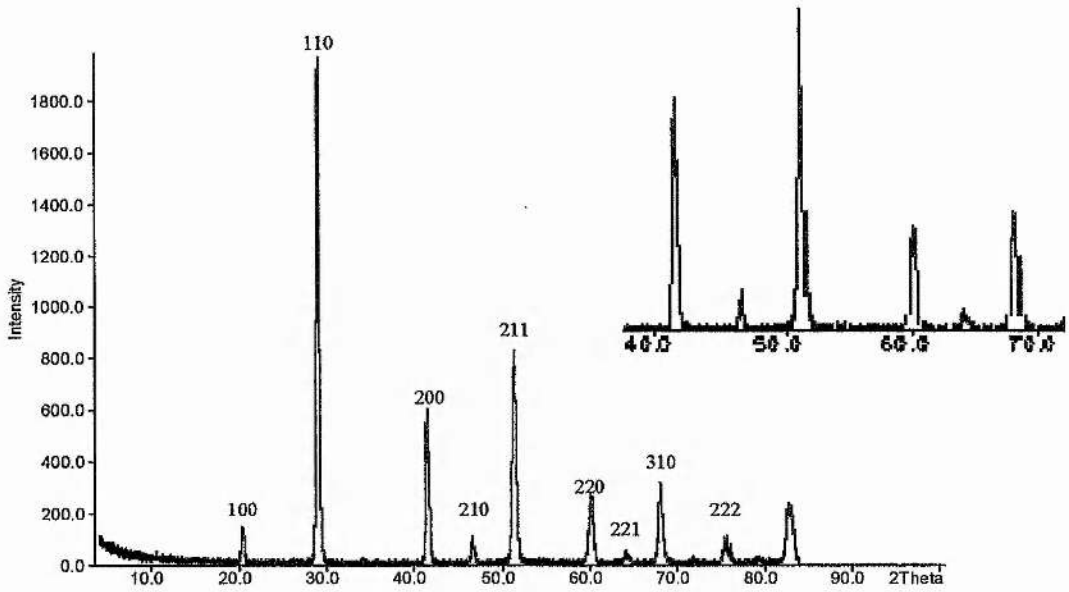

Fig. 3.5 XPD pattern of $Ba_{1.1}Bi_{0.9}O_3$ at room temperature

EDS microanalysis was performed to confirm its homogeneity, 18 particles were selected. Once again the K = 0.691 was used in the calculation, using this value the ratio of Bi/Ba was: CBi/Ba=0.78, Standard deviation=0.05. This value agrees with the theoretical value of 0.818 for this compound when the standard deviation is taken into consideration. Many reasons could account for the initial slight reduction in the original value. The particles could have been too thick, they may have been too near another particle, which then absorbed some X-rays, the particle may have been slightly turned away from the detector and finally the known problem of overlapping peaks. All of these conditions must be taken into consideration when analysing EDS microanalysis results. When this is taken into account it is assumed that the perovskite phase observed for this sample has the nominal Ba rich stoichiometry.

The SAED study of this material (*Fig. 3.6*) show the pattern for the basic pseudocubic unit cell in the [110] projection, however small weak satellite spots were also evident, these could be superlattice spots in one dimension. These faint spots could not be indexed and did not appear in the XRD pattern as extra peaks, never the less they could be significant. This could be due to deviation from the cubic symmetry of the unit cell.

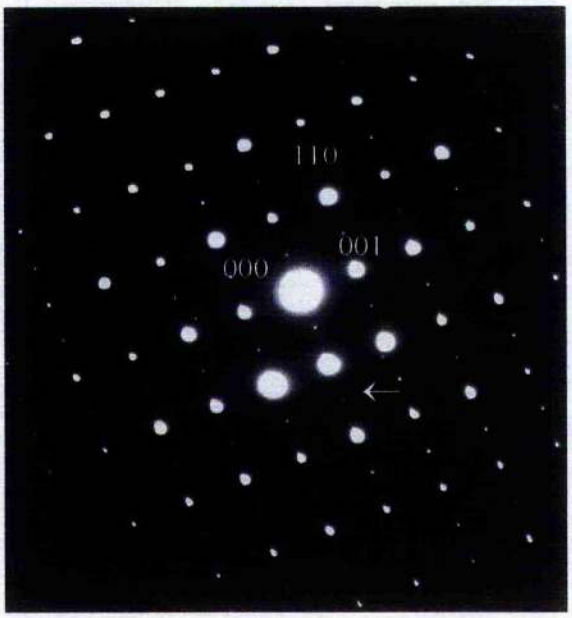

Fig. 3.6 [110] projection SAED of $Ba_{1.1}Bi_{0.9}O_3$.

Extra diffraction spots appear in diffraction pattern *Fig. 3.6* (arrow), however these spots could not be indexed to correspond to the perovskite pseudocubic unit cell and so there appears to be a 2-fold superlattice along the [110] direction. In this case, the smallest superunit cell is $\sqrt{2}$ X $\sqrt{2}$ X 2 derived from the basic perovskite unit cell. HRTEM imaging of this sample reveal a superlattice but also did show the typical cubic structure evident in the basic perovskite unit cell. The *Fig's. 3.7a, b* show images with the beam parallel to the [111] direction and parallel to the [100] direction showing no evidence of superstructure. From the evidence presented by both the SAED patterns and images it has to be concluded that there is superstructure present in some crystals as observed in *Fig. 3.6* and that the dominant orientation still relates to that of the basic perovskite cubic structure, however there also appears to be some lattice distortion present as well and this is shown by *Fig. 3.7b* on the next page.

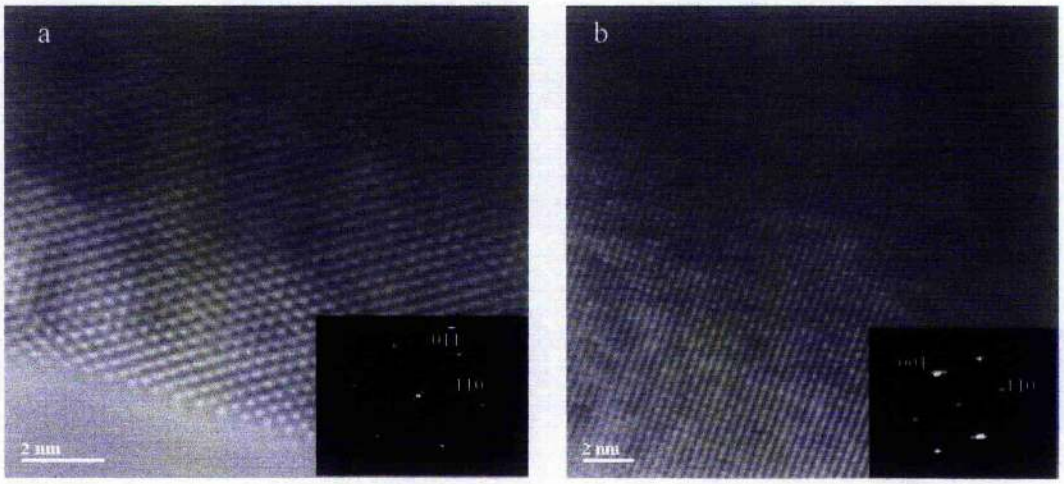

Fig. 3.7 HRTEM images and corresponding FFT diffraction patterns from $Ba_{1.1}Bi_{0.9}O_3$ viewed down the (a) [111] and (b) [100] directions of the crystal.

3.3 $Ba_{1.2}Bi_{0.8}O_3$

The appearance of the sample after preparation and firing was of a greenish/black powder. As before, powder XRD analysis was gained from the above sample. In the XRD study of this material (*Fig. 3.8*), the pattern show once again peaks corresponding to the basic unit cell, however a number of extra peaks of varying intensity are also evident. The pseudocubic reflections appear to be split to a greater degree (inset), suggesting that the difference between, a_p, b_p, c_p is rather larger than in $BaBiO_3$. The extra peaks are $2\theta = 25°, 34°, 43°, 53°$, none of which are peaks which signature the $\sqrt{2}a_p \times \sqrt{2}b_p \times 2c_p$ cell present in the $BaBiO_3$ standard. These observations may imply that the symmetry of the cell in this sample has changed so the space group is no longer I2/m. The XRD result suggests that there may be a substitution of the Bi cations on the B-sites by Ba cations giving an increase in the difference in the primitive cell dimensions a_p, b_p, c_p and therefore leading to the formation of a lower symmetric unit cell.

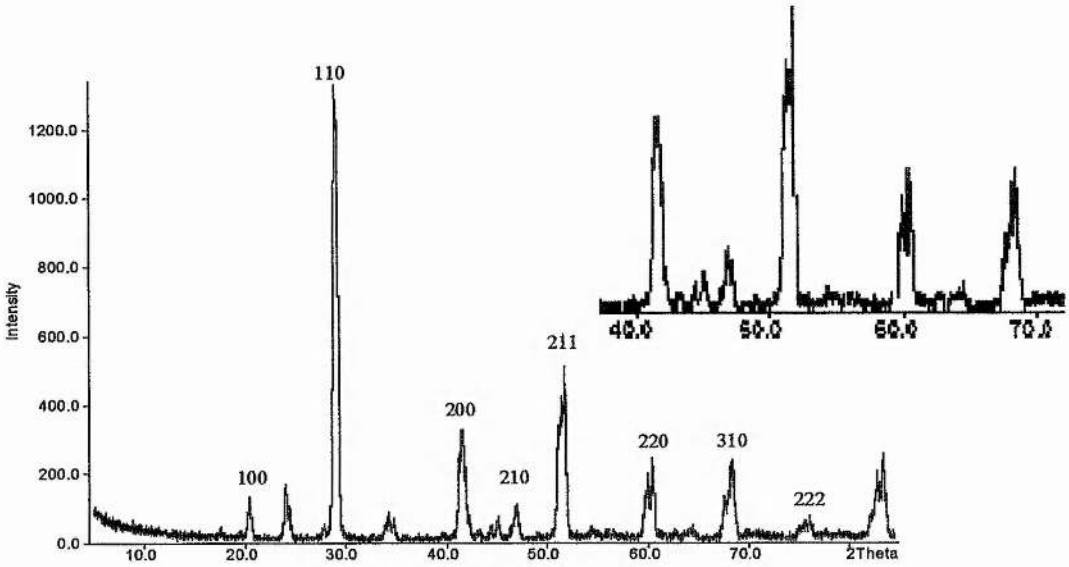

Fig. 3.8 XPD pattern for $Ba_{1.2}Bi_{0.8}O_3$.

EDS microanalysis was performed on the composition to ascertain its homogeneity. 20 particles were selected, Using the K=0.691, CBi/Ba=0.47±0.06. This result was down on the expected theoretical value for this sample of 0.666; this could be attributed to the experimental problems in EDS outlined in the previous section. However the EDS result combined with the presence of the extra peaks shown in the XRD pattern could lead us to assume that the sample is perhaps not single phase and that it is slightly nonhomogeneous, it may indeed have two phases. When those two separate phases are calculated the results obtained are, phase one, CBi/Ba=0.85±0.03 and phase two, CBi/Ba=0.42±0.07.This would explain the decrease in the overall result when the CBi/Ba is calculated from all 20 particles. If the reaction did not go to completion it may leave the sample with excess Ba in the form of $BaCO_3$. One other conclusion is that the high temperature used for the reaction could lead to decomposition of a proportion of the Bi_2O_3 leaving an excess amount of Ba for the ratio $Ba_{1.2}Bi_{0.8}$.

The SAED study of this material (*Fig. 3.9)* shows the pattern for the basic pseudocubic unit cell, however small weak satellite spots were also evident and these could be evidence of a superlattice. *Fig. 3.9a* shows the pattern obtained with the electron beam parallel to the [001] direction of the pseudocubic cell, and reveals the presence of weak satellite spots. A second pattern (*Fig. 3.9b)* shows the pattern obtained with the

electron beam parallel to the [021] direction of the pseudocubic cell, this also reveals weak satellite spots. It would appear that the substitution of Bi for Ba has a subtle effect on the symmetry of the perovskite lattice. This change could be due to ordering of cations on the B-sites. This could be supported by the observation by XRD of extra peaks, which cannot be indexed (although as stated above those could also be caused by an incomplete reaction) and by SAED of satellite spots although those may be faint.

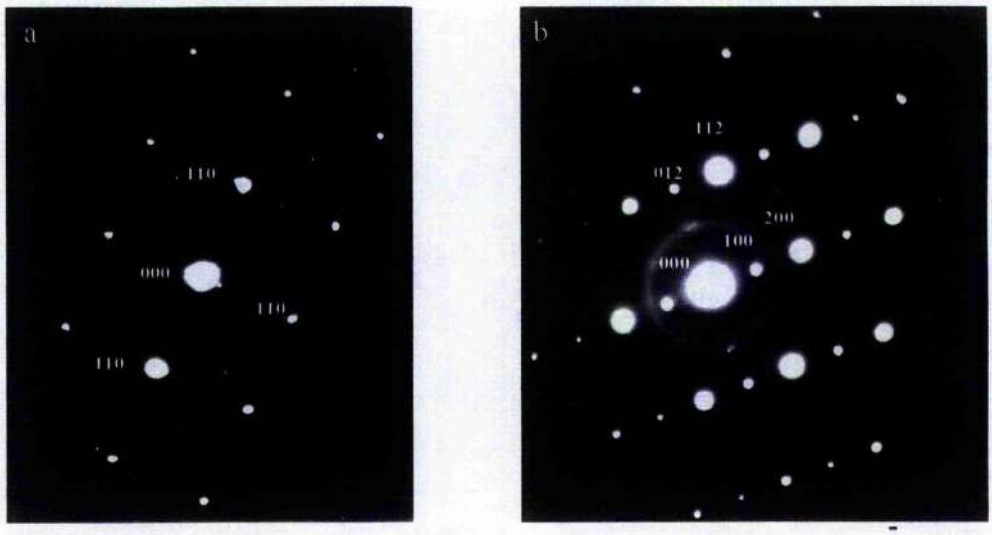

Fig. 3.9 SAED patterns from $Ba_{1.2}Bi_{0.8}O_3$ along the (a) [001] and (b) [021] directions.

Fig. 3.9a is a pattern showing a [001] orientation which is readily associated with a cubic perovskite structure, however faint extra spots can be seen and those could indicate presence of superstructure. One other possible explanation for their presence may be one crystal overlapping another. *Fig. 3.9b* is not dissimilar to the [111] pattern of the basic cubic cell, however the distances from the central spot (000) to the strong spots are not equal. When those distances are calculated it is found that the pattern is in fact $[0\bar{2}1]$. The angles between spots must also be taken into consideration in determining this pattern. The determination in how those extra spots came about will be discussed later. The most likely explanation is that it is the ordering of the cations to each other, this could be ordering of Ba and Bi, however it seems much more likely that it is the ordering of the Bi^{5+} and the Bi^{3+} cations (due to their differing valency) in this and in subsequent samples of the Ba Bi O_3 system that is responsible for the extra spots observed.

HRTEM imaging of $Ba_{1.2}Bi_{0.8}O_3$ found that no superlattice were observed at high resolution TEM. This may be due to the very weak and subtle changes in the structure of the lattice.

Although images *Fig's 3.10a,b* show little evidence of superstructure, the FFT pattern inset, *(Fig. 3.10a)* shows very weak extra spots. They are however very faint and appear to have no apparent effect on the overall structure of the crystal. This is shown in the IFFT image of this area. The basic [011] pattern is not distorted or in an altered state, which you could normally expect if a superstructure were present.

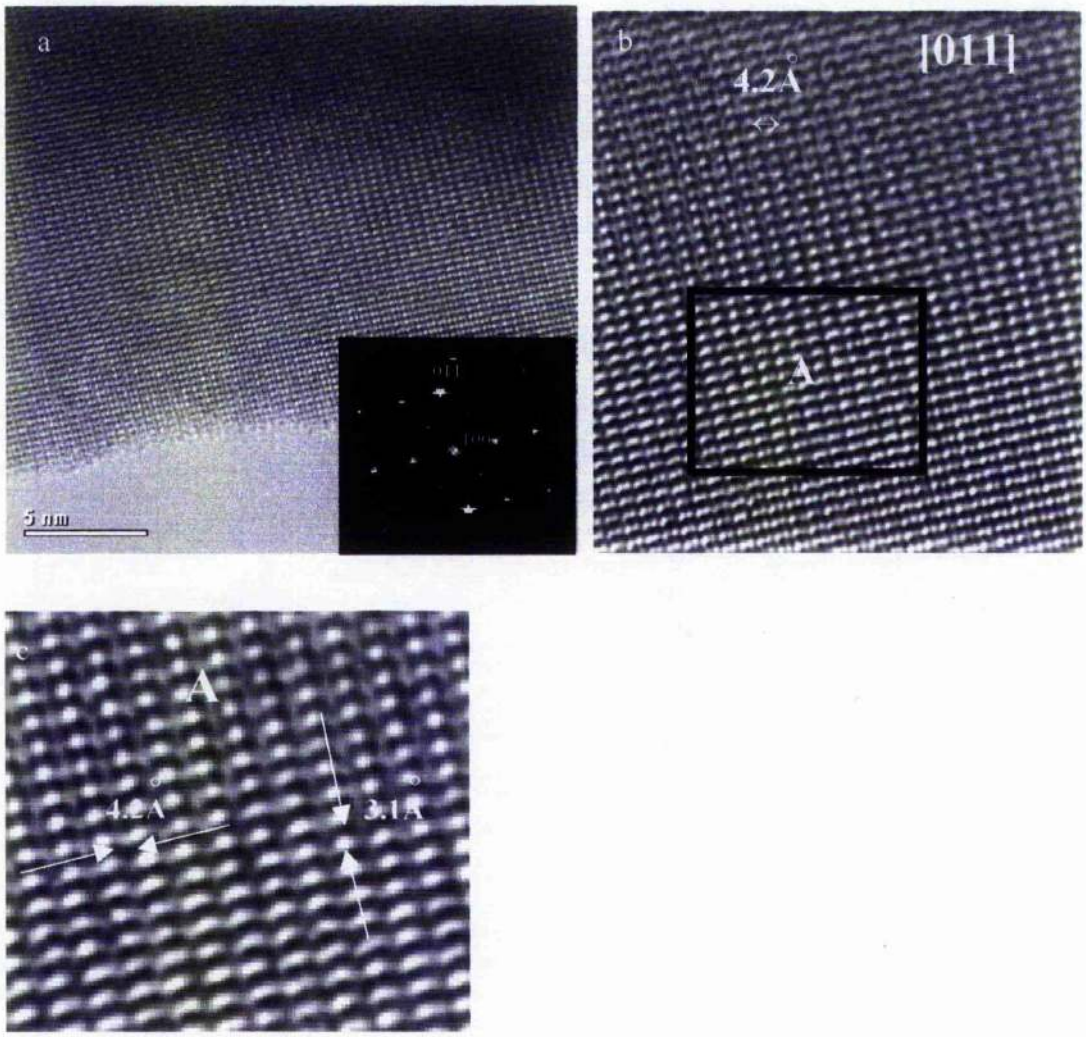

Fig. 3.10 (a) Original image plus FFT pattern, (b) Showing region for masking, (c) enhanced image from area (A) of a crystal of $Ba_{1.2}Bi_{0.8}O_3$ in the [011] orientation.

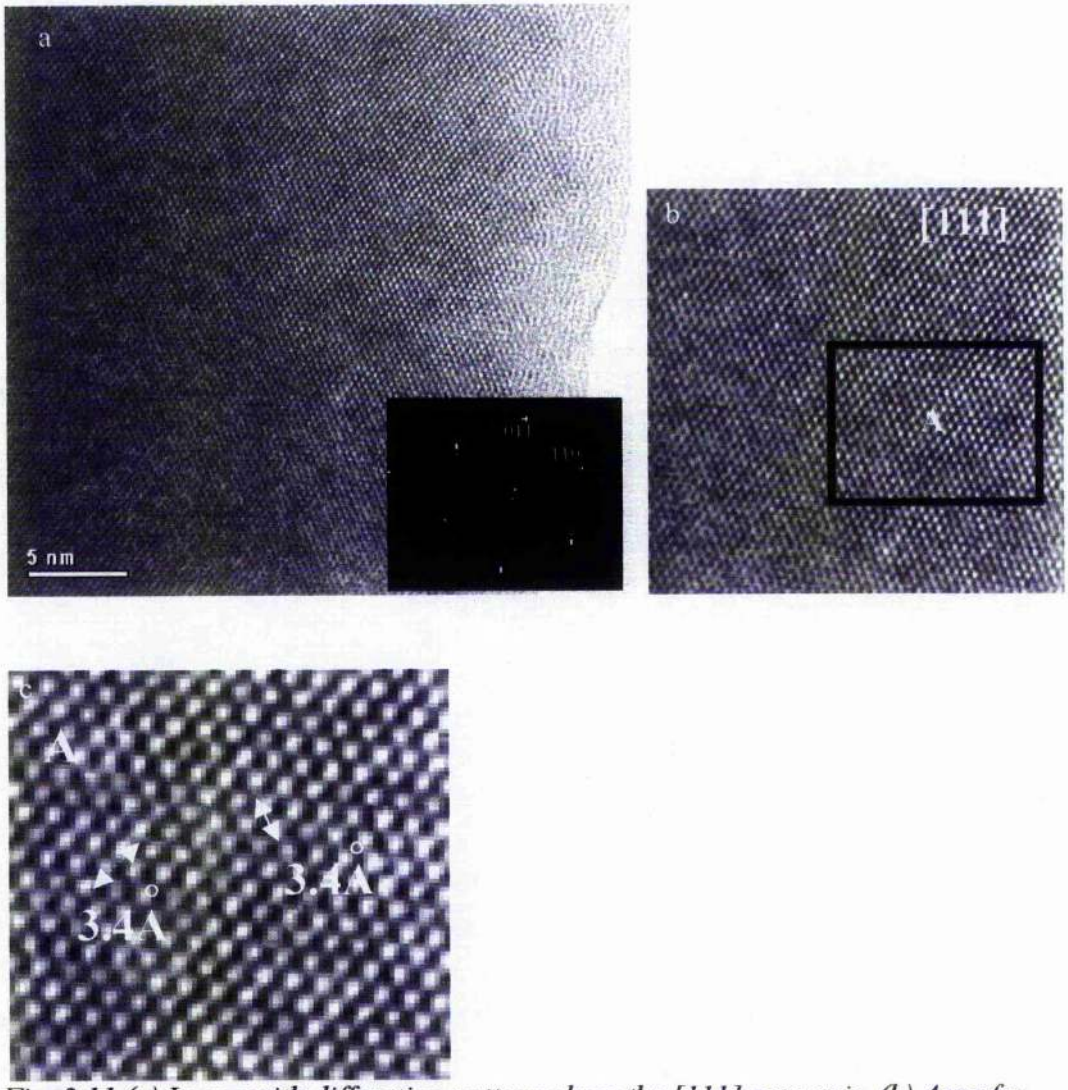

Fig. 3.11 (a) Image with diffraction pattern along the [111] zone axis, (b) Area for cropping and enhancing, (c) Cropped and enhanced area of $Ba_{1.2}Bi_{0.8}O_3$.

Another crystal analysed using SAED and HRTEM imaging, *Fig. 3.11a-c* shows no change in overall structure, to that of the basic perovskite solid solution. No superstructure is present.

In conclusion it would appear that the solid solution $Ba_{1.2}Bi_{0.8}O_3$ has little structural change taking place with this amount of Ba "doping", shown by the results of SAED and HRTEM imaging. However extra small peaks did appear in the powder XRD pattern, this may indicate possible superstructure. However given the inconclusive EDS data and the extra peaks in the XRD pattern it is at least a strong assumption that the above results are the result of a reaction not going to completion. Loss of Bi in the heating process due to the very high temperatures involved may be a cause of the higher than expected Ba/Bi ratio in the EDS results.

3.4 $Ba_{1.4}Bi_{0.6}O_3$

This time after preparation and firing the appearance of the sample was of greenish powder. Once more powder XRD studies on the sample were undertaken (*Fig. 3.12).*
The results obtained for $Ba_{1.4}Bi_{0.6}O_3$ show a pattern similar to that of $Ba_{1.2}Bi_{0.8}O_3$, however with a few exceptions. In $Ba_{1.4}Bi_{0.6}O_3$ there is a peak at $2\theta \sim 18°$, where there is none at that position in $Ba_{1.2}Bi_{0.8}O_3$. The peaks in $Ba_{1.4}Bi_{0.6}O_3$ also appear to be more defined and the pseudocubic reflections less split, which may suggest that the symmetry in the $Ba_{1.4}Bi_{0.6}O_3$ sample is different from that of the $Ba_{1.2}Bi_{0.8}O_3$ sample.

In comparison to that of the $BaBiO_3$ pattern, extra peaks apart, the pseudocubic reflections are all present indicating that once again the pattern corresponds to that of the basic perovskite cubic unit cell. Perhaps the indication that the pseudocubic reflections are not as greatly split (inset) as they are in $Ba_{1.2}Bi_{0.8}O_3$ reflects that the difference between a_p, b_p, and c_p is not as large in this sample as it was in $Ba_{1.2}Bi_{0.8}O_3$ and that it is closer to that of the standard.

One extra peak is evident in both $Ba_{1.4}Bi_{0.6}O_3$ and $Ba_{1.2}Bi_{0.8}O$ $2\theta \sim 35°$ this peak corresponds to hkl (111) and fits in with the $\sqrt{2}a_p \times \sqrt{2}b_p \times 2c_p$ cell. This observation may imply that the symmetry of the cell has changed and the space group is no longer I2/m. The further extra peaks which do not fit with the $\sqrt{2}a_p \times \sqrt{2}b_p \times 2c_p$ cell ($2\theta \sim 18°$, 25° 45°, 54°, 63°) may indicate presence either of superstructure or a multi phase solid solution.

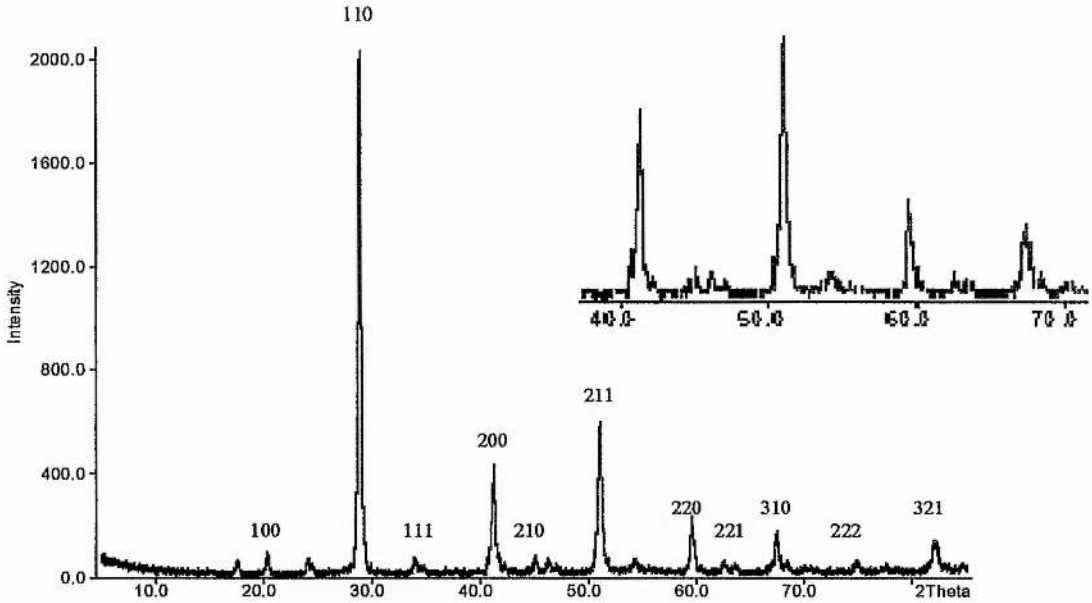

Fig. 3.12 XPD pattern of $Ba_{1.4}Bi_{0.6}O_3$.

EDS microanalysis was again performed on the composition to confirm its homogeneity. As with the previous samples using the K constant, K=0.691, the value CBi/Ba=0.32±0.1 was calculated. This was slightly down on the expected ratio from this sample of 0.42. Why is this the case? The reasons usually associated with microanalysis EDS such as, overlapping, sample thickness, absorption problems and sample thickness all could lead to the ratio being marginally smaller than the theoretical value. Taking those anomalies and a small systematic error the EDS result probably shows that the reaction has gone to completion and that the sample is single phase and homogenous.

From images obtained from the SAED study of this material (*Fig's. 3.13a,b)* the diffraction patterns show the pattern for the basic pseudocubic unit cell, however satellite spots were also evident. The diffraction pattern (*Fig. 3.13a)* obtained with the electron beam parallel to the [011] direction of the pseudocubic cell also reveals satellite spots. *Fig. 3.13b* from the same sample down the [111] projection also shows weak spots next to the diffraction spots associated with the pseudocubic cell. It is interesting to compare this pattern with the corresponding initial pattern obtained from the $BaBiO_3$, (*Fig. 3.3a)*, which also shows a projection [111] along the zone axis of the primitive pseudocubic unit. It should be noted that for this sample and the $Ba_{1.2}Bi_{0.8}O_3$ sample studied a variety of patterns were obtained from different crystals, some reveal the presence of satellite

spots, some show diffuse streaks and others gave no occurrence of superlattice. This may suggest that these compositions, in terms of the possible cationic ordering are rather inhomogeneous.

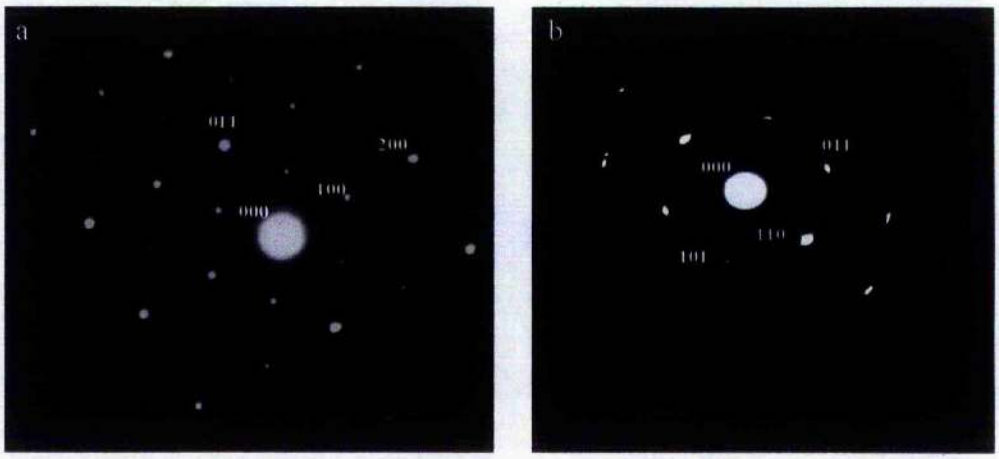

Fig. 3.13(a) Electron diffraction in [011] projection, (b) Electron diffraction in [111] direction from $Ba_{1.4}Bi_{0.6}O_3$.

HRTEM imaging of $Ba_{1.4}Bi_{0.6}O_3$ was observed at high resolution power on the Jeol-Jem 2011 TEM. *Fig. 3.14a* shows the original [111] pattern with the FFT diffraction image shown inset. There appear to be no superstructure in evidence from either image. *Fig. 3.14b* is taken from the same area of the crystal; this was masked using the Gatan software to rid the image of excess background noise. The distinctive [111] pattern associated with the cubic perovskite phase can clearly be seen. *Fig. 3.14c* is a close up image of the same area after masking showing detailed measurements.

The atomic columns in *Fig. 3.14c* are imaged as dark dots. Bismuth and barium-containing columns are imaged as dots of a different "darkness". The darkness is directly related to a columns composition i.e., to the column potential. Taking into account that the sample is barium rich it seems plausible that these dark columns must be enriched in barium. From this enhanced image it can also be seen that the measurement from the central column to any of the other columns in the pattern is equidistant at 3.5Å.

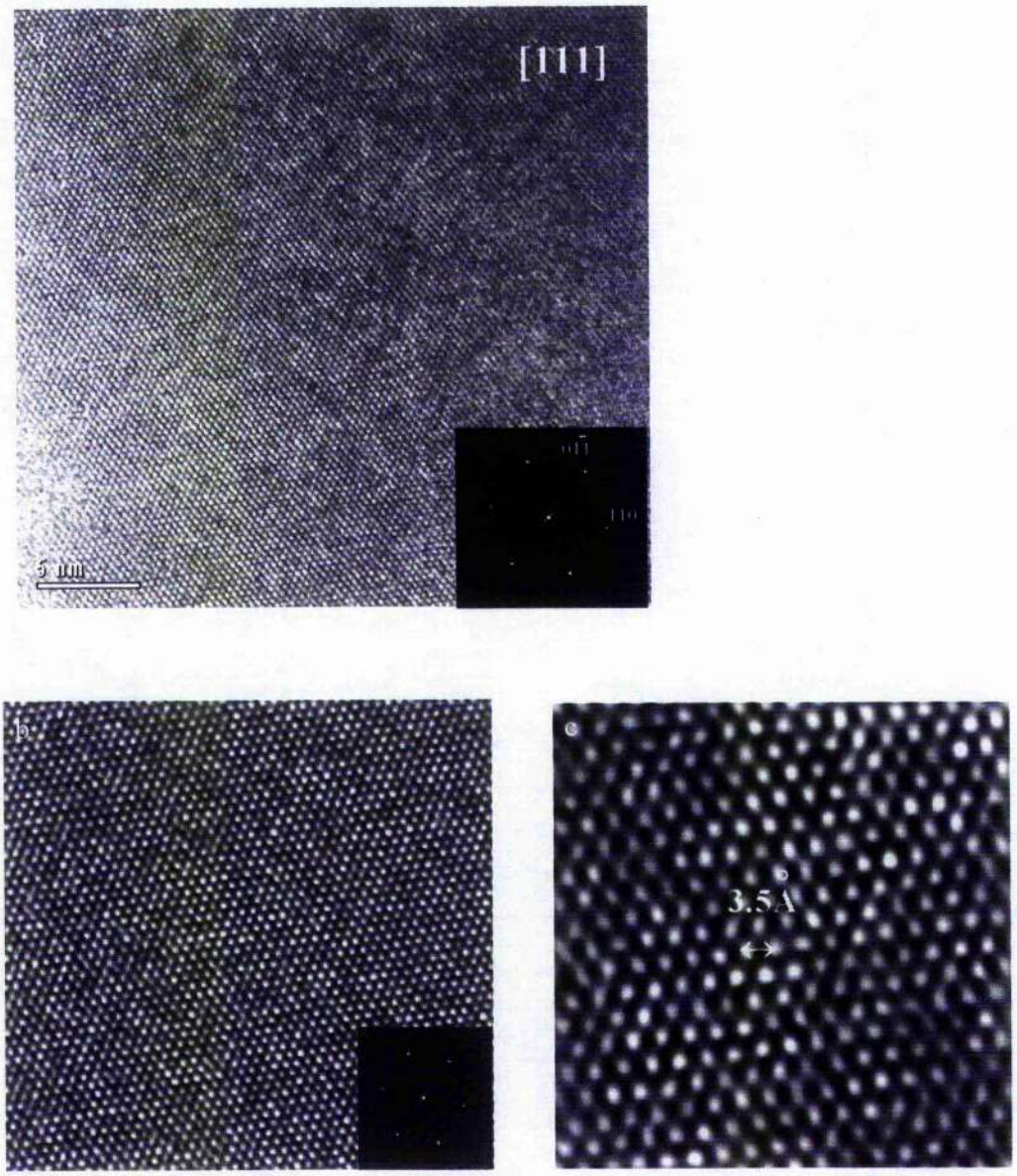

Fig. 3.14 (a) Image and diffraction pattern in the [111]Projection, (b) Image after masking, (c) Image cropped and measured from $Ba_{1.4}Bi_{0.6}O_3$.

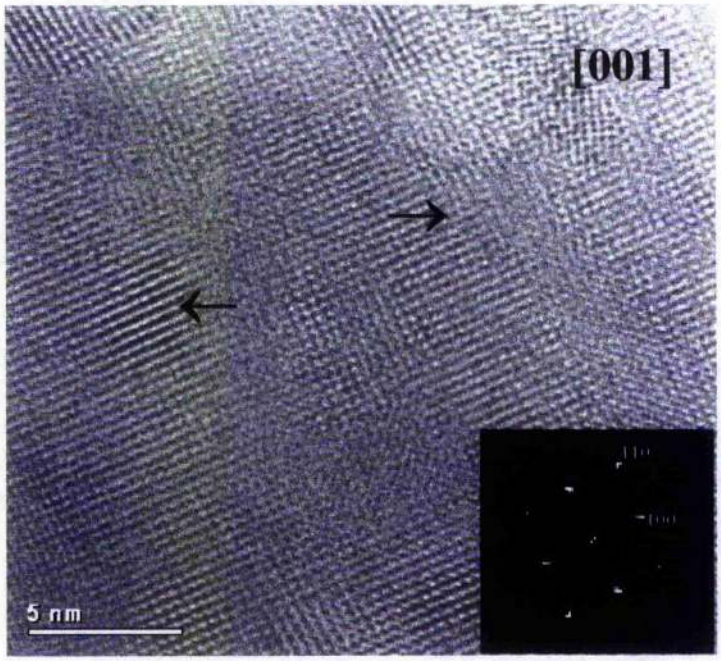

Fig. 3.15 Image in [001] showing two defect domains, (arrowed) in $Ba_{1.4}Bi_{0.6}O_3$.

The image above is shown in the [001] direction, however there are also defects in evidence; these are arrowed. In domains such as those, ordering appears to have broken down into some kind of disordered structure. This could be caused by the instability of the Ba cations in the highly doped solid solution. Similar defect and disorder are not in evidence in the less doped Ba rich samples. Defects are themselves very interesting areas of study due to the change in structure they bring to a composition which in turn could lead to a change of electrical properties of a sample. The defect shown in *Fig. 3.15* leads to a break in the regular periodicity of the crystal lattice and a change in the electronic structure. The electronic properties of $BaBiO_3$ samples are in fact dominated by such effects, doping is in fact the deliberate introduction of impurities, which lead to defects. The defects shown above appear to be disruption of a crystal in a single lattice site, or at most a small group of sites. This kind of defect range may contain **point defects** *(Cox 1987)*. This defect is often charged as they introduce an imbalance of ions of different types, in this case an imbalance of Ba to Bi. Charged defects can only exist if the charge is compensated by that of other defects. The defect above could consist of a Ba cation and an O anion vacancy or vacancies. This sort of defect in metals tends to decrease

conductivity, however in non-metallic solids defects introduce extra electrons into the conduction band.

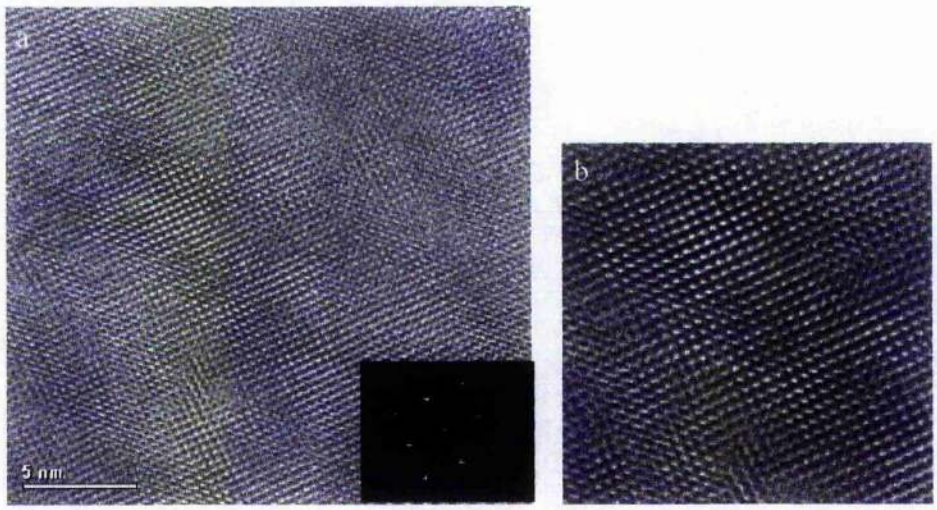

Fig. 3.16 (a) Image and diffraction in the [001] direction, (b) corresponding masked image along the [001] zone axis of $Ba_{1.4}Bi_{0.6}O_3$.

Fig. 3.16a is an image showing a much more uniformly ordered area in the [001] direction of the same crystal. Inset is the FFT diffraction pattern of this image. *Fig. 3.16b* is the inverse FFT image of the previous image, (*Fig. 3.16a)* after masking. Why should this particular area in the crystal be more stable than that shown in *Fig. 3.15*? One explanation of this could be due to the strength of the electron beam on the crystal. It has been suggested that the ordering of the cations can be changed in some circumstances as a result of electron beam inducing oxygen vacancies *(Koyama and Ishimaru 1992).*

If the sample is homogenous the impact of the beam should be consistent over the sample, however even at best the sample may not be 100% homogenous. It would appear however that usually the Ba rich solid solution is fairly stable and that disorder is not widespread.

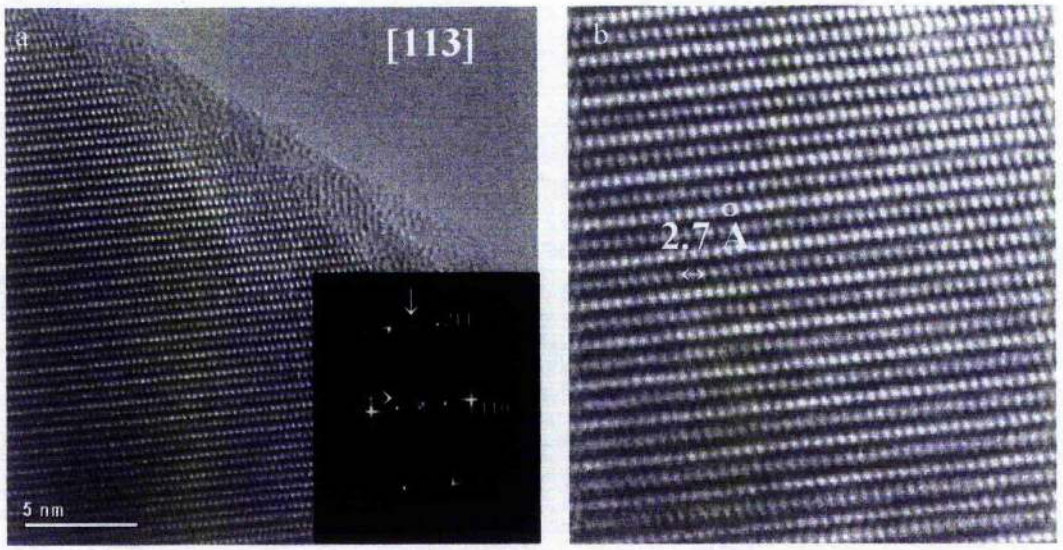

Fig. 3.17 (a) Image in the [113] projection, (b)The corresponding masked image of $Ba_{1.4}Bi_{0.6}O_3$.

The two images above are taken in the [113] projection, the basic pattern with bright spots are shown in *Fig. 3.17a.* Faint, weak extra spots are also in evidence in the FFT inset (arrowed). *Fig. 3.17a* is the original image in the [113] direction, showing possible superlattice structure. (*Fig. 3.17b)* is the corresponding IFFT image after masking.

Finally the superstructure *(Fig's 3. 18a-d)* could have arisen from partial ordering of Bi^{3+} and Bi^{5+} and displacements of the Bi^{3+} cations within the [011] orientation, however this could also relate to the creation of a $\sqrt{2} \times \sqrt{2} \times 2$ supercell due only to deviation from cubic symmetry. Oxygen associated with the Bi sites may be more labile than those adjacent to the Ba site and therefore O vacancies may be produced preferentially next to the Bi cations *(Allen and Bischofs 2002)*. The expected growth of superlattice with increase in Ba quantity is probably due to an increase in the number of Ba^{2+} ions in the B′-site of Ba_2 (B′)(B″) O6. Ba ions occupy the B-site because a Ba^{2+} ion can enter the B-sites, which contain smaller hexavalent cations. Superlattice and change in symmetry of $Ba_{1.4}Bi_{0.6}O_3$ suggest a change of arrangement of O vacancies within the composition or the ordering of cations of Bi and Ba.

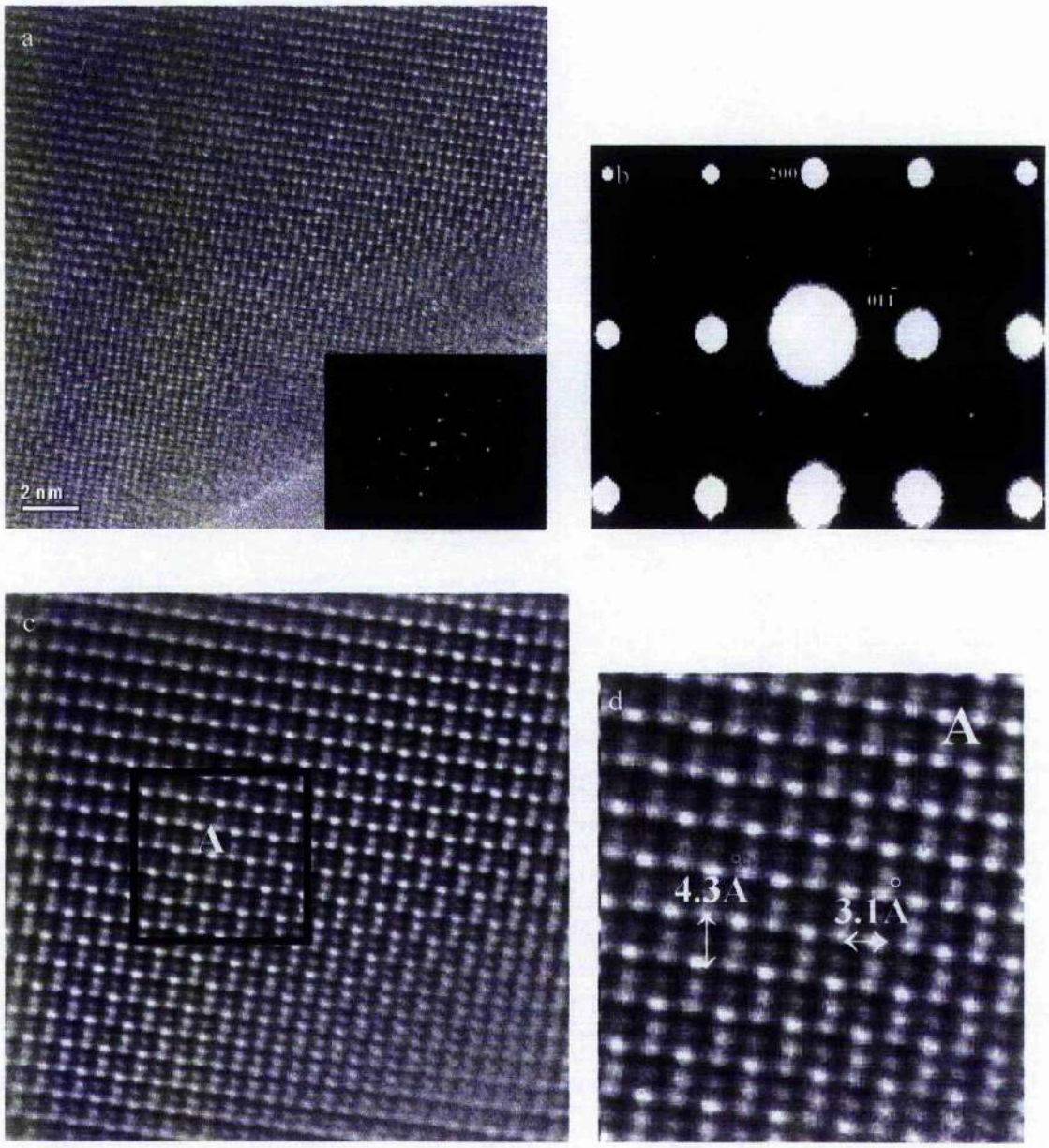

Fig. 3.18 (a) [011] image plus FFT inset, (b) Diffraction with extra spots, (c) Masked Area used for cropping, (d) Cropped enhanced area of $Ba_{1.4}Bi_{0.6}O_3$.

It was initially decided to synthesise the Bi rich compounds exactly as those of the Ba rich samples. $Ba_{0.8}Bi_{1.2}O_3$ was chosen as the starting sample. This composition was chosen as it was thought that the increase in Bi by this amount could lead to an altered state giving some interesting structural changes, without any excess Bi loss due to synthesis or beam exposure.

3.5 $Ba_{0.8}Bi_{1.2}O_3$

As with the standard material stoichiometric amounts of $BaCO_3$ and Bi_2O_3 were ground together in acetone, the powder appeared to be yellow at this point. The mixture was then pressed into a pellet, placed onto an aluminium boat on gold foil and heated in a tube furnace at 820°C for 48 hours with flowing pure O_2. A slow heating ramp was introduced of 5°C per minute. This time the sample was quenched under flowing O_2 as it was thought that the Bi rich samples were not as stable as the Ba rich samples. The appearance of the sample after firing was of a powder slightly blacker than that of the standard material.

The XRD study of this material (*Fig. 3.19)* was consistent with that of the standard, however a number of peaks (notably that at $2\theta \sim 20.4°$, corresponding to [100] reflections of the primitive pseudocubic cell) are reduced in intensity, suggesting that the primitive cell, based on $a_p \approx 4.34$Å is tending to-ward body-centring. However previous work on this composition suggests that this peak and others should be greatly diminished. This could arise from the problem of previous attempts to synthesise $Ba_{1-x}Bi_{1+x}O_3$ samples. All were unsuccessful and resulted in multiphase products, with the main perovskite phase having a pattern almost identical to that of $BaBiO_3$. Initially this problem was thought to have arisen from too high a temperature during the reaction, the sample may have simply melted or the reaction may not have gone to completion. One another scenario could be that the extra Bi in the sample may have disassociated in the high temperature furnace needed for this reaction and that the product was not a Bi rich solid solution but was in fact one which was nearer a sample of 1:1 Ba/Bi or indeed one which was Ba rich.

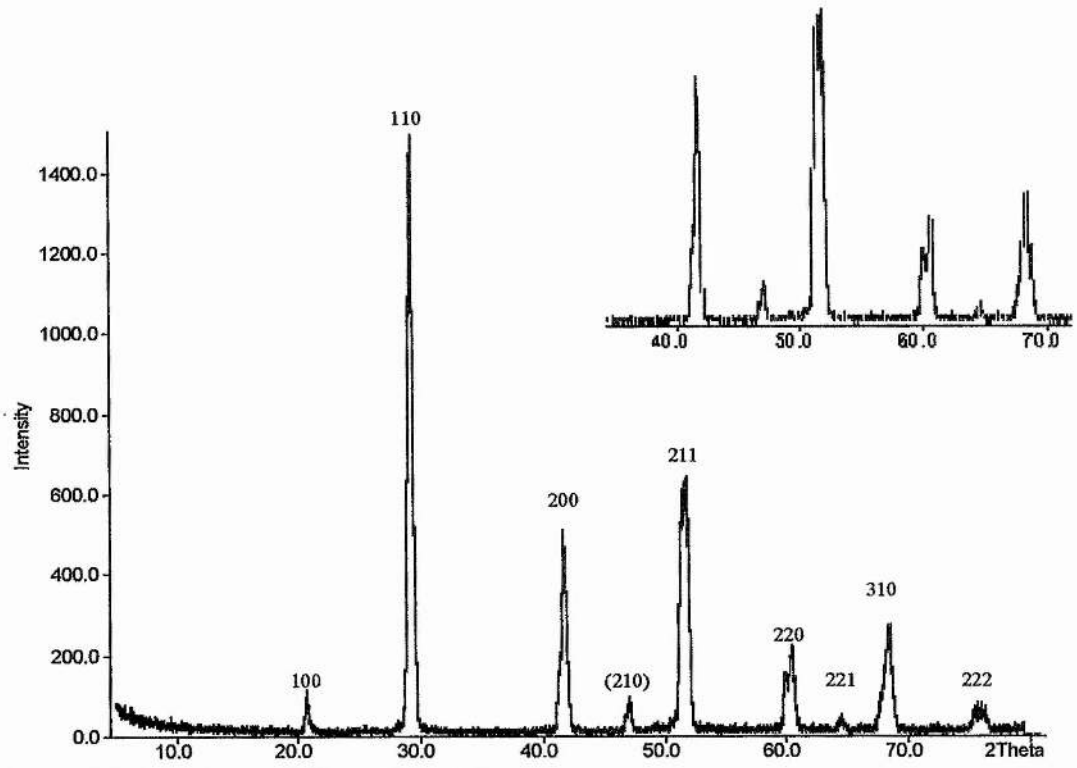

Fig. 3.19 XPD pattern of $Ba_{0.8}Bi_{1.2}O_3$.

Despite this apparent problem EDS microanalysis was performed on the composition to confirm its homogeneity. The calibration constant for the standard sample $BaBiO_3$ was used, K=0.691, CBi/Ba=1.1±0.1. The ratio should be near to the value 1.5 if it is a monophasic sample. The result obtained appeared to be out-with the margin of error and demonstrates that the perovskite phase observed had not the nominal Bi-rich stoichiometry assumed. Subsequent attempts to synthesise other Bi rich samples (x>0.2) were also initially unsuccessful leading to multi-phase non-homogenous samples.

The SAED study shows weak extra diffraction spots (*Fig. 3.20a)*. This pattern along with image (*Fig. 3.20b)* is based on the typical cubic perovskite unit cell. One reason for the absence of extra peaks in the XPD study could be hidden reflections from the stronger basic cell peaks.

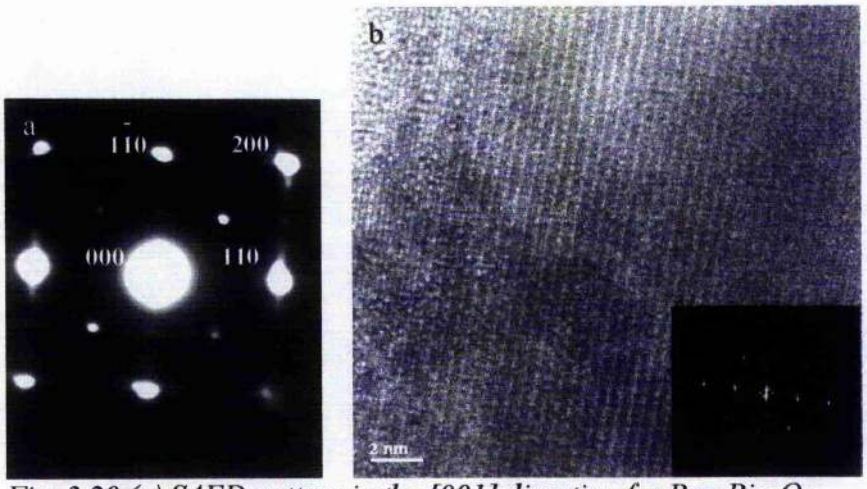

Fig. 3.20 (a) SAED pattern in the [001] direction for $Ba_{0.8}Bi_{1.2}O_3$, (b) Image and FFT inset in the [001] projection, image showing possible superlattice.

The HRTEM imaging supports the findings of the SAED results that a lattice exists with similar structural characteristics to that of the basic perovskite structure, with possible superstructure, however given the EDS results it has to be concluded that the sample is not monophasic and that it is inhomogeneous. The instability of the Bi rich solid solution appears to be related around the metal–insulator transition ($x \approx 0.4$), this may cause the problems experienced. This Bi rich sample was synthesised again involving a two-step method, initially heating in a furnace under flowing N_2 gas before annealing under flowing O_2 and quenching. A smaller step increase of Bi in each of the subsequent compounds was also decided.

The composition $Ba_{0.8}Bi_{1.2}O_3$, was prepared again, this time involving the two-step method; the samples appearance was one of a dark slightly metallic black powder. The powder XRD pattern. *Fig. 3.21* again shows a small change with respect to the pattern obtained for the standard composition. This was a much more encouraging result than the previous attempt to synthesise this sample. The implication was that the sample this time had indeed different structure to that of the standard. However only after microanalysis study and HRTEM diffraction and imaging could it be concluded that this sample of $Ba_{0.8}Bi_{1.2}O_3$ was indeed homogenous and possessed the ratio of Bi to Ba expected.

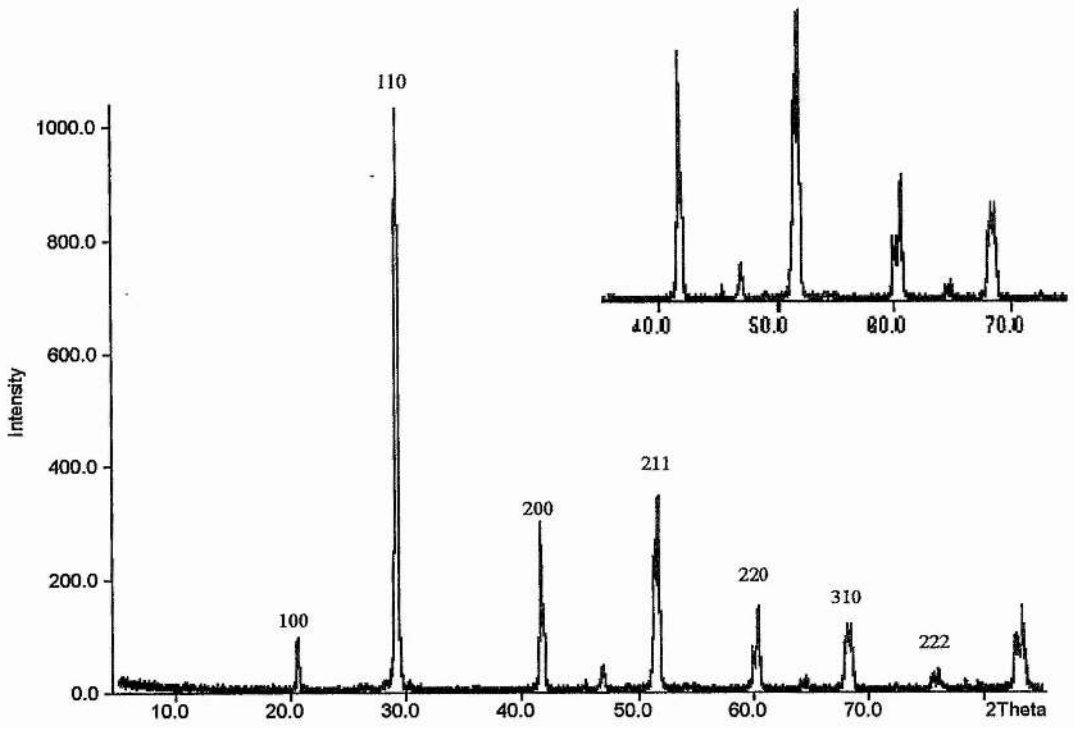

Fig. 3.21 XPD pattern of $Ba_{0.8}Bi_{1.2}O_3$.

The peaks in the pattern above seem rather less defined than those in the previous patterns, the peaks themselves seem to be many separate peaks, this may mean that the composition is tending to-wards asymmetry, however it could also imply that the reaction has not gone to completion and that the sample is not single phase. From the XRD pattern alone it is not possible to tell if there is symmetry splitting or two phases. Given the difficulties in the previous attempt to synthesise this composition, this gives some cause for concern.

With this in mind the EDX microanalysis became even more important to confirm the homogeneity of the sample, CBi/Ba=0.83±0.06. This result is down by some margin on the expected result for this sample of 1.5. It would appear from the small standard deviation result that the sample is homogenous, however the sample is not $Ba_{0.8}Bi_{1.2}O_3$. A large quantity of Bi has been lost either because of the high temperature required for the reaction, or possibly under the electron beam during microanalysis acquisition. This loss of Bi under the beam is significant and will be discussed in much more detail in a further section. The ratio calculated implies the sample to be $Ba_{1.1}Bi_{0.9}O_3$, a Ba rich sample rather than one, which is Bi rich.

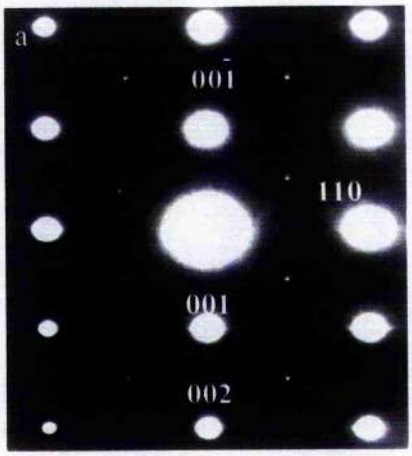

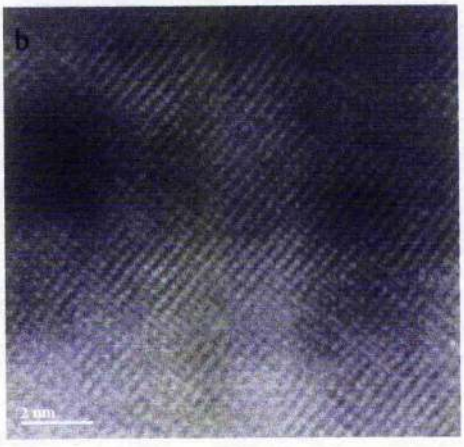

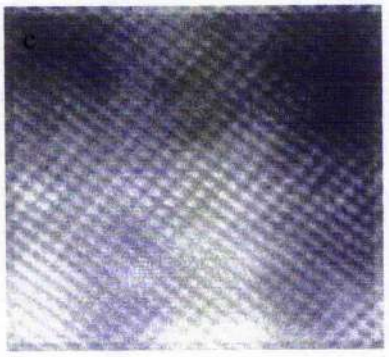

Fig. 3.22 (a) [110] Projection showing weak extra spots, (b) [110] Projection HRTEM image, (c) [110] Projection enhanced for $Ba_{0.8}Bi_{1.2}O_3$.

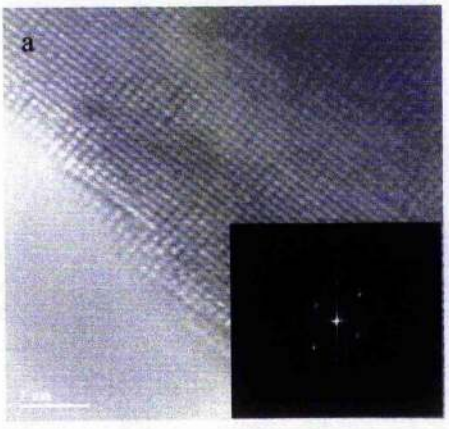

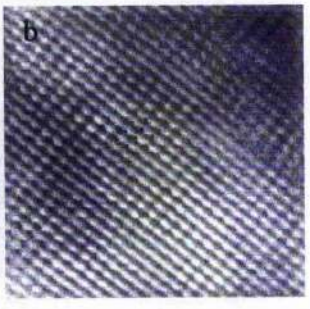

Fig. 3.23(a) [110] Projection image, corresponding FFT inset, (b) Image after masking from $Ba_{0.8}Bi_{1.2}O_3$.

This solid solution sample shows extra lattice spots along the [110] zone axis as can be seen from *Fig's. 3.22, 3.23*. This may account for the information obtained from the powder XRD pattern. *Fig. 3.22a* shows the original diffraction pattern obtained after tilting in the X and Y directions of the sample. The main strong spots of the basic [110] pattern can be seen along with weaker spots, which could not be indexed. *Fig. 3.22b is* the corresponding HRTEM image with the distinct [110] pattern; *Fig. 3.22c* shows the image after masking to reduce the background. *Fig. 3.23a* is an image taken on a separate crystal once again in the [110] direction, inset an FFT image showing a pattern identical to that of the original diffraction pattern. *Fig. 3.23b* is an image after masking showing clearly the [110] pattern. Although this is clear evidence that extra spots are present in some form in this sample, no other patterns were found with extra lattice spots after extensive study.

This composition may have to be the subject of further study, to reach the definitive conclusion that the sample is single-phase perovskite material. EDS results indicate a homogenous sample with a Bi:Ba ratio, tending to-ward a Ba rich sample. It appears that the more Bi rich a compound becomes the unstable under the electron beam it becomes. Because of this a smaller increase in the Bi cation was attempted.

3.6 $Ba_{0.95}Bi_{1.05}O_3$

After preparation involving the two-step method described above the samples appearance was one of a dark brown/black powder. The pattern obtained by powder X-ray diffraction *(Fig. 3.24)* apparently shows that even a small quantity of Bi substitution also causes a subtle change in the structure. This can possibly be explained either by the change in the ordering of the Ba and Bi cations or indeed the ordering of the Bi^{3+} and the Bi^{5+} cations. However the change in structure can also be determined by the very nature of the synthesis reaction itself and this has to be disproven before the cation ordering theory is further examined.

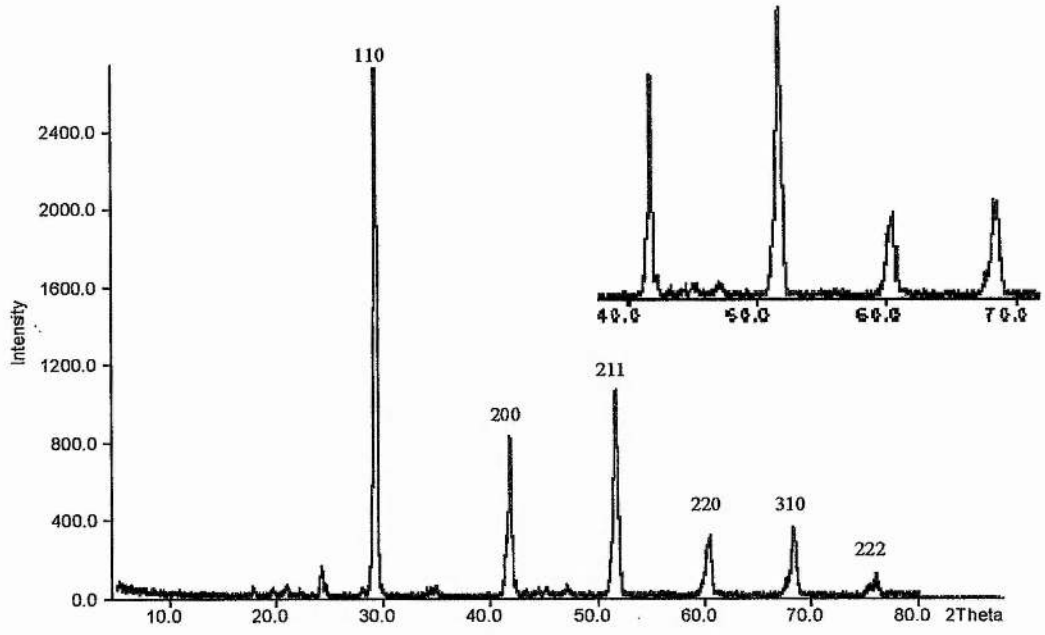

Fig. 3.24 XPD pattern of $Ba_{0.95}Bi_{1.05}O_3$.

The pseudocubic reflections appear to be split in comparison with the standard sample, this could be an indication that the difference between a, b and c is greater than in the standard material. At least two peaks present in $BaBiO_3$ appear to be absent or at very least diminished in $Ba_{0.95}Bi_{1.05}O_3$ (e.g. $2\theta \sim 20.471°$ and 64.4°), corresponding to the (100) and (221) reflections of the pseudocubic primitive cell.

A number of fairly weak extra peaks can be observed. Some of these fit with the $\sqrt{2}a_p \times \sqrt{2}b_p \times 2c_p$ cell e.g. ($2\theta \sim 22.9°$, 43.7°, 47.9°) but are systematically absent in $BaBiO_3$.This observation may imply that the symmetry of the cell in $Ba_{0.95}Bi_{1.05}O_3$ has changed, however further extra peaks are observed which do not relate to the $\sqrt{2}a_p \times \sqrt{2}b_p \times 2c_p$ cell. This may be consistent with the presence of a superlattice if the sample is single phase. The other possible cause of extra peaks is presence of impurity within the sample, the most likely being, in this case a small amount of $BaCO_3$ impurity. Higher temperatures may be needed to rid the sample of excess $BaCO_3$. EDS microanalysis was performed at 200kV on the sample to confirm its homogeneity, K=0.691, CBi/Ba=1.02±0.26. This result was very slightly down on that which would be expected, of a ratio of 1.1, however it is within the error. The standard deviation is also large which shows that there was a considerable difference in the CBi/Ba of the particles selected for

EDS analysis. The sample may consist of two phases. Although the CBi/Ba=1.02 can be attributed to systematic error, overlapping, absorption etc, the large anomaly between one crystal to another may mean that the sample is not monophasic or homogenous.

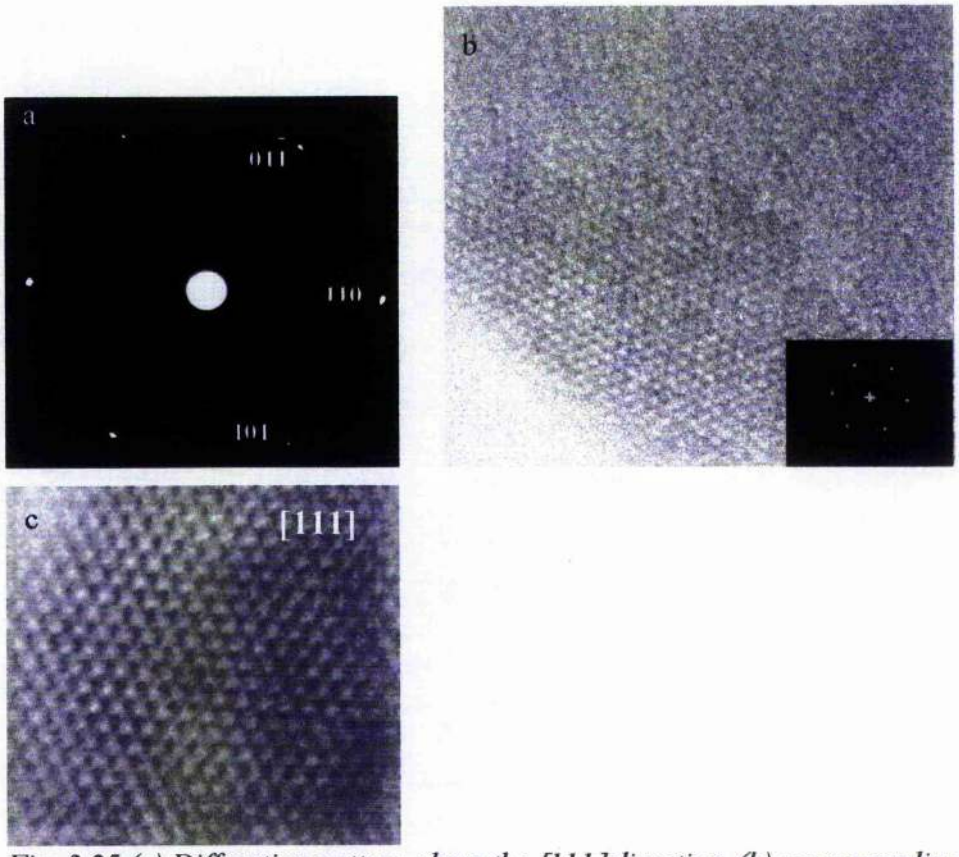

Fig. 3.25 (a) Diffraction pattern along the [111] direction, (b) corresponding Image and FFT along [111] direction, (c) Enhanced image with [111] projection in evidence for a solution of $Ba_{0.95}Bi_{1.05}O_3$.

The images above show the basic cubic pattern in the [111] projection. *Fig. 3.25a* is the original diffraction pattern in the [111] orientation obtained from one crystal of the $Ba_{0.95}Bi_{1.05}O_3$ sample. This was indexed to the basic structure. A high resolution image was taken using the CCD camera from the diffraction pattern site (*Fig. 3.25b)* showing the structure, which would be expected of the diffraction pattern (*Fig. 3.25a),* the FFT of the image is shown inset confirming the orientation. *Fig. 3.25c* is an image of the Inverse

FFT after masking and filtering of the original image, this enhances the image but it is not a simulation, it is a real image.

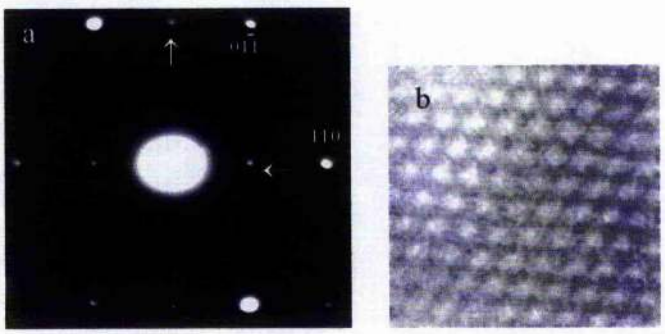

Fig. 3.26 (a)[111]direction SAED image with extra spots arrowed, (b) corresponding enhanced image from $Ba_{0.95}Bi_{1.05}O_3$.

One other crystal observed however did appear to have the presence of weak satellite spots *(Fig's. 3.26.a, b)* those could not be indexed to the basic cubic structure, (arrows). This could well explain the presence of the extra peaks in the diffraction pattern.

No further superstructure could be found in the composition $Ba_{0.95}Bi_{1.05}O_3$ however, and it can only be concluded that the small change in the Bi content had little effect on the structure of the composition. However the small extra peaks observed in the diffraction pattern along with the erratic EDS microanalysis results may suggest that the reaction has not gone to completion and that it is not single phase. One other suggestion may be that the superstructure exists as observed but that the lattice spots are too infrequent and or weak to observe in any great detail.

3.7 $Ba_{0.90}Bi_{1.1}O_3$

After preparation involving the two-step method described previously the samples appearance was one of a dark powder. The pattern obtained by powder X-ray diffraction *(Fig. 3.27),* apparently shows that a small quantity of Bi once again causes a subtle change in the structure, according to the diffraction pattern. The pattern shown appears to have less defined peaks, this could confirm that the sample is becoming more

asymmetrical. As with the previous sample the extra peaks could be an indication of impurity in the sample, an indication that the reaction has not been completed and is therefore not monophasic, or that there is a presence of a superstructure.

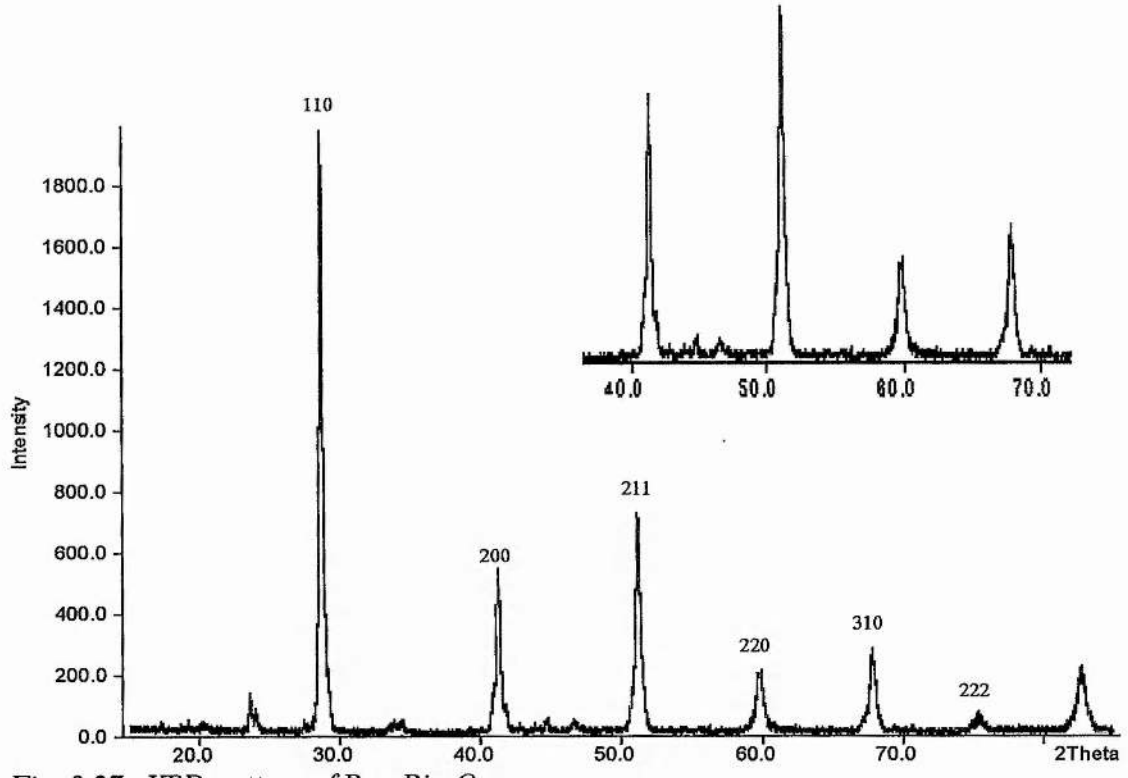

Fig. 3.27 XPD pattern of $Ba_{0.9}Bi_{1.1}O_3$.

EDX microanalysis was performed at 200kV on the sample to confirm its homogeneity, K=0.691, CBi/Ba=1.2±0.2. This result was as the expected result of 1.2, it therefore appears that the sample is homogenous and that it has the Bi-rich stoichiometry assumed. The rather high standard deviation however could imply a multiphase sample. It would appear from the early results obtained for the Bi rich samples that the synthesis of those solid solutions is problematic, this is due to the very high temperatures over a fairly long time required for the reaction to go to completion. It appears as if Bi can be readily lost over the period of the reaction.

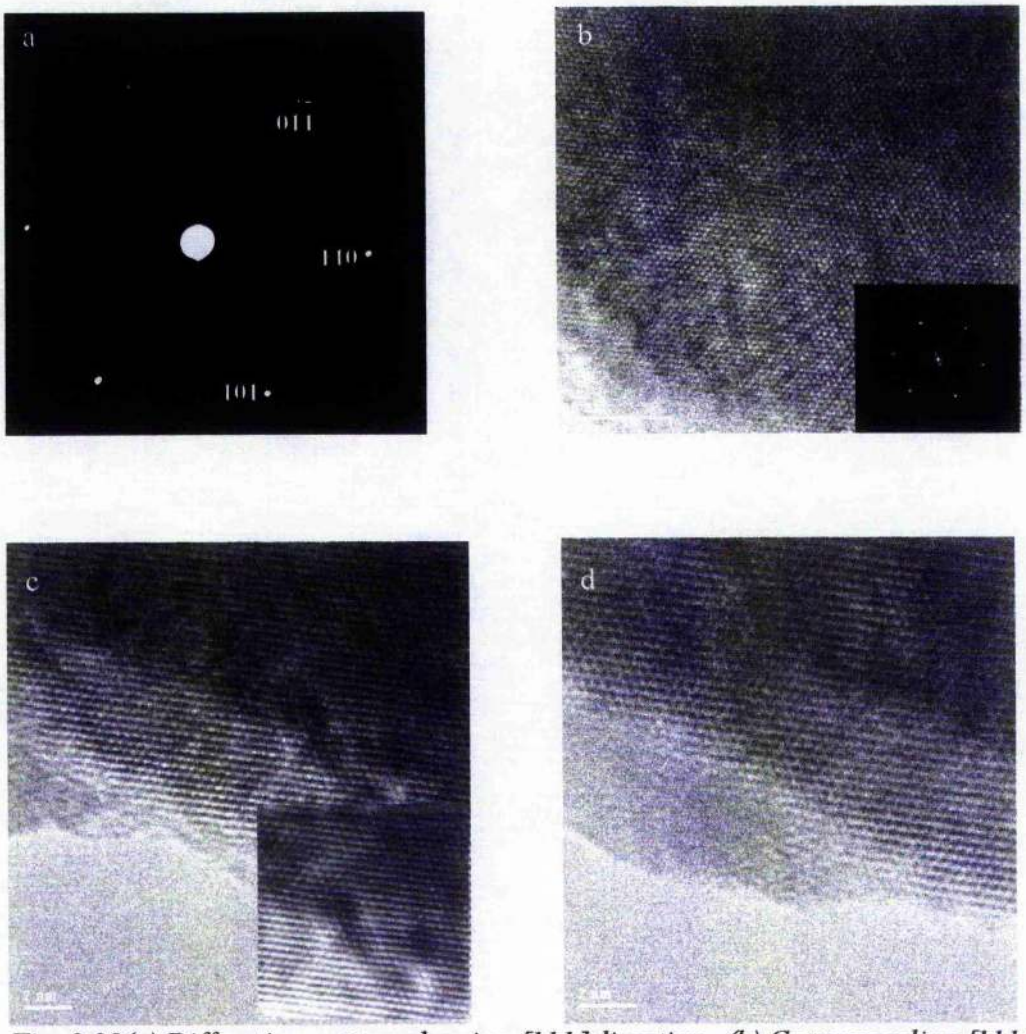

Fig. 3.28(a) Diffraction pattern showing [111] direction , (b) Corresponding [111] direction image with FFT, (c) [111] projection image with masked image inset, (d) Image showing ordered [111] direction structure in $Ba_{0.90}Bi_{1.1}O_3$.

Once again the sample above appears only to consist of the basic cubic structure, which would be expected of a composition of equal parts Bi and Ba, as the standard. *Fig. 3.28a* is the original diffraction pattern in the [111] orientation, also shown are three corresponding images taken from this [111] region (*Fig's. 3.28b-d*).

The fact that no other patterns other than that of [111] can be found, along with the absence of superlattice is of slight concern. This is especially so because there appeared to be some evidence of extra diffraction spots in the sample with very little extra Bi i.e.

$Ba_{0.95}Bi_{1.05}O_3$. The x-ray pattern is also more akin to that of the standard sample than is that of $Ba_{0.95}Bi_{1.05}O_3$. However the EDS microanalysis results imply that the sample is homogenous. It may be the case that as Bi replaces Ba the sample becomes much more unstable under the electron beam, with the loss of one or more of the cation atoms. In the scenario that it is Bi that is lost this could lead the composition reverting back to its primitive form. The evidence in this case being that only the basic structure appears to be in evidence.

3.8 $Ba_{0.5}Bi_{1.5}O_3$

Recent studies have shown that a wide range of Ba rich compositions exhibit the perovskite structure with oxygen vacancies induced by excess barium, however attempts to synthesis Bi rich perovskite phases $Bi \geq 1.2$ by firing a mixture of $BaCO_3$ and Bi_2O_3 in air results in multiphase compounds. The two-step method mentioned previously is used therefore to synthesise a single phase perovskite compound, which can be structurally analysed using firstly powder X-ray diffraction *(Fig. 3.29)* and then HRTEM.

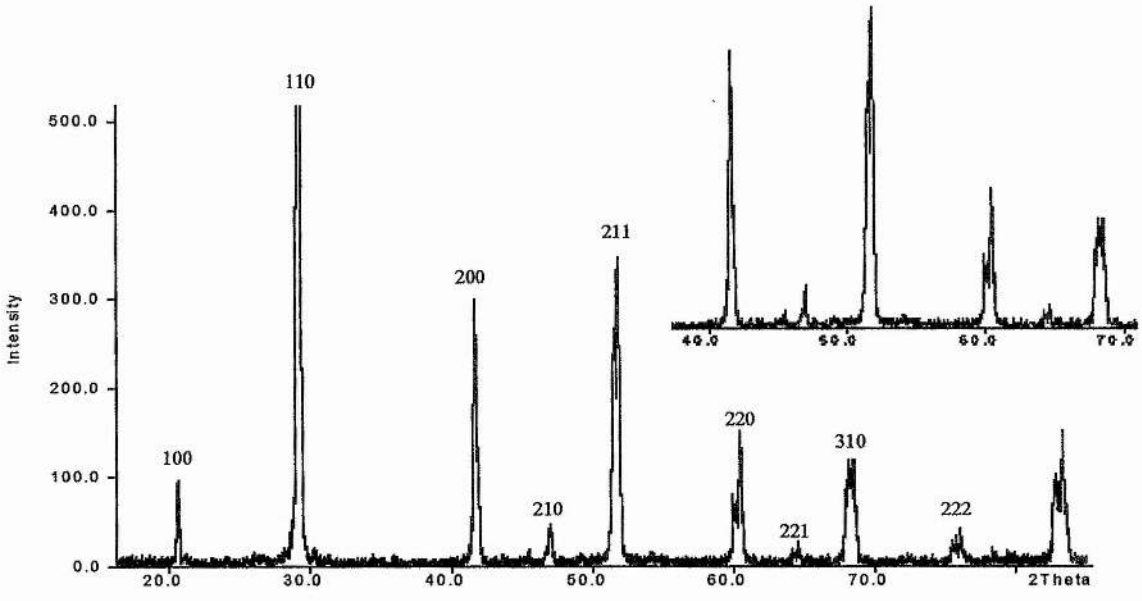

Fig. 3.29 XRD pattern of $Ba_{0.5}Bi_{1.5}O_3$.

The reactions that occur when this Bi rich compound is exposed to the electron beam of the transmission electron microscope will also be discussed. Ordering of the Bi and Ba cations in $Ba_{0.5}Bi_{1.5}O_3$ and indeed the O anions can be altered into a different ordered or disordered state after exposure to a strong electron beam. This is due almost totally to losing the Bi atoms in the crystal, which escape outwards (*Fig. 3.30).*

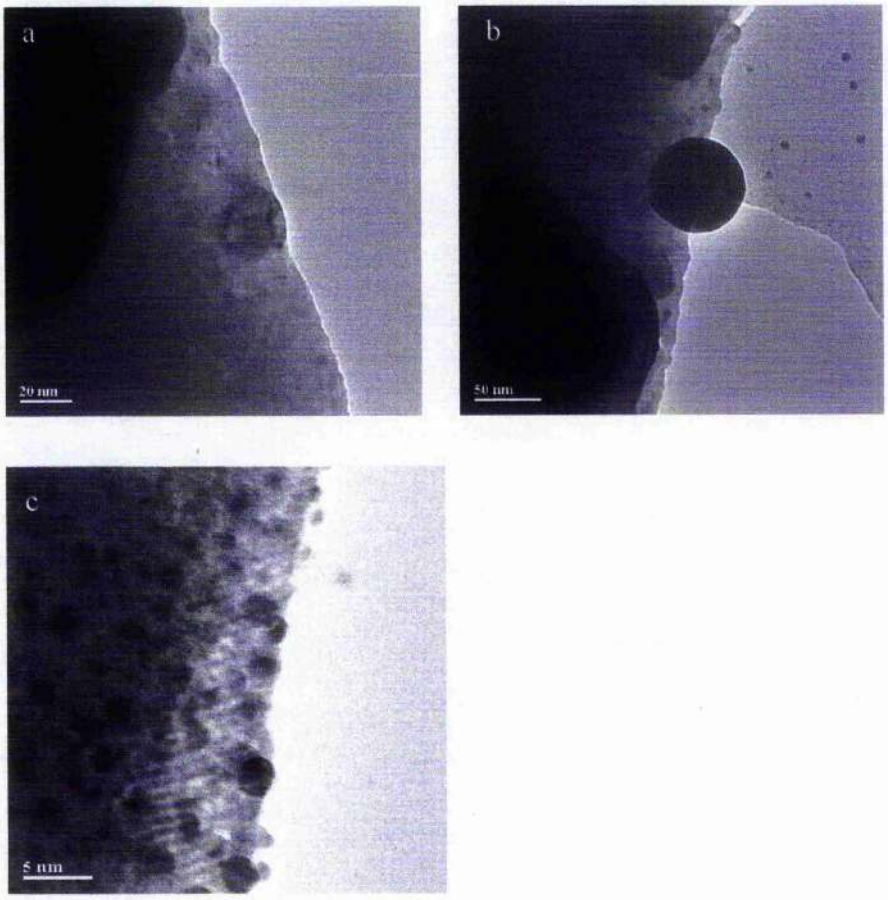

Fig. 3.30 (a) Start of beam exposure, (b) Exit of particles from the main crystal of a sample of $Ba_{0.5}Bi_{1.5}O_3$, (c) Extreme loss of one element from $Ba_{0.5}Bi_{1.5}O$.

The above images show the disassociation of the compound, the first two images (*Fig. 3.30a,b)* have the Bi rich structure forcing its way to the surface of the crystal and with the energy of the electron beam, forcing itself out of the crystal. In time continuous exposure to a strong electron beam will lead to Bi loss throughout the crystal *(Fig. 3.30c).*

This dramatic loss in the Bi cation will lead to a drastic change in ordering in the compound, either by losing Bi the compound will revert towards a 1:1 Ba to Bi ratio or indeed become Ba rich. However one other scenario could be that vacancies left by the Bi will be filled by Ba atoms. In either case the structure will be altered dramatically from the one studied initially.

EDS was undertaken on the dense particles escaping from the crystal to confirm that they were Bi in composition, the spectrum of which is shown in *Fig. 3.31.*

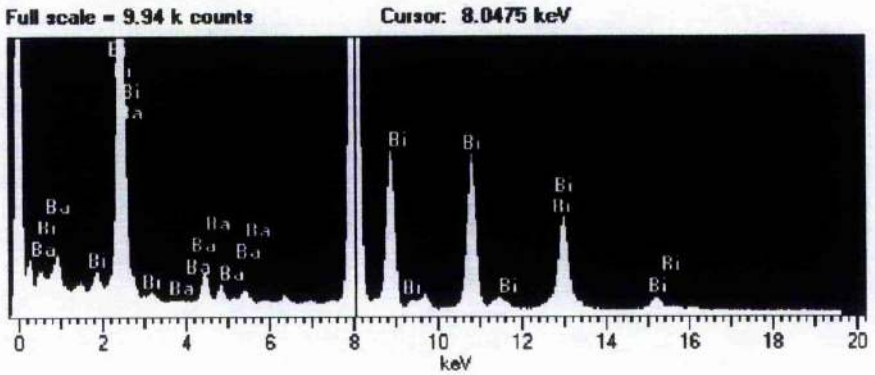

Fig. 3.31 EDS spectrum taken from escaping particles from $Ba_{0.5}Bi_{1.5}O_3$.

The peaks for the Bi series have increased while those for the Ba have decreased in magnitude. Quant analysis was then undertaken on this spectrum, with the expected results.

Elmt	Peak Area	Stat. Sigma	k Factor	Abs. Corrn.	Element weight %	Sigma %	Atomic weight %
Ba L	19417	536	2.029	1.000	14.11	0.36	19.99
Bi L	81369	957	2.947	1.000	85.89	0.36	80.01
Total					100.00		100.00

This shows clearly that the particle escaping from the crystal is made up almost entirely of Bi atoms, this segregated phase is pure Bi not an oxide of Bi. The small amount of Ba shown in the results is to be expected, as the EDS analysis area is in close

proximity to a compound with Ba present. Another possible effect of the disassociation of the crystal in one area is the formation of domains within a single crystal, one area may have a very different structure to that of an area next to it *(Fig. 3.32)*.

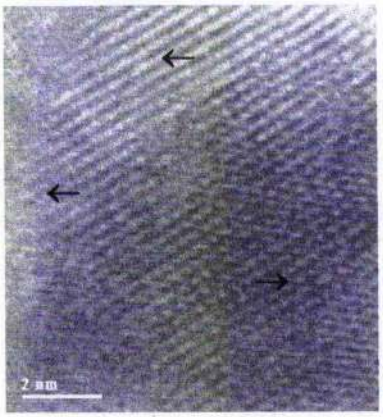

Fig. 3.32, Separate domains in a crystal of $Ba_{0.5}Bi_{1.5}O_3$ (arrowed).

This image shows two or possibly three different domain areas due to structural changes occurring within the one crystal after disassociation. This is a single crystal from $Ba_{0.5}Bi_{1.5}O_3$ exposed to a high intensity electron beam for two minutes. The following is an example of how easily and quickly the crystal can start to break down under a high intensity electron beam.

An area *(Fig. 3.33a)* from a single crystal of $Ba_{0.5}Bi_{1.5}O_3$ is chosen for an SAED study followed by structural images. This area proves to have a diffraction pattern *(Fig. 3.33b)* consistent with that of basic cubic with the [111] projection.

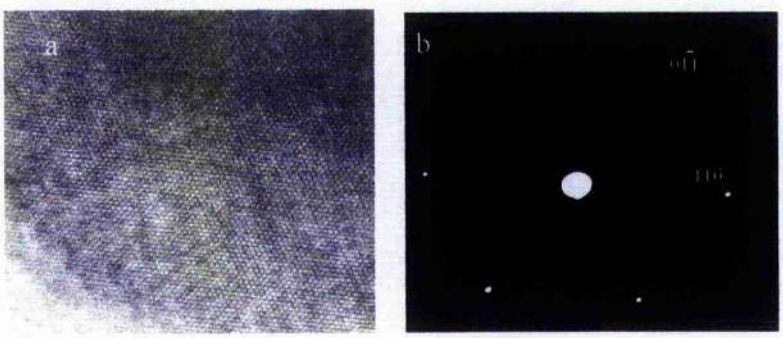

Fig. 3.33 (a) [111]projection image, (b) Diffraction showing associated [111]projection consistent with the basic cubic unit cell in $Ba_{0.5}Bi_{1.5}O_3$.

EDS quantitative analysis of this area confirms that the Bi and Ba levels are consistent with the stoichiometric compound.

EDX FROM BASIC CUBIC DIFFRACTION PATTERN

Elmt	Peak Area	Stat. Sigma	k Factor	Abs. Corrn.	Element weight %	Sigma %	Atomic weight %
BaL	33120	568	2.029	1.000	23.46	0.38	31.81
Bi L	74368	890	2.947	1.000	76.54	0.38	68.19
Total					100.00		100.00

After 1-2 minutes of exposure to the electron beam, high resolution imaging shows quite different results *(Fig's. 3. 34a,b)*.

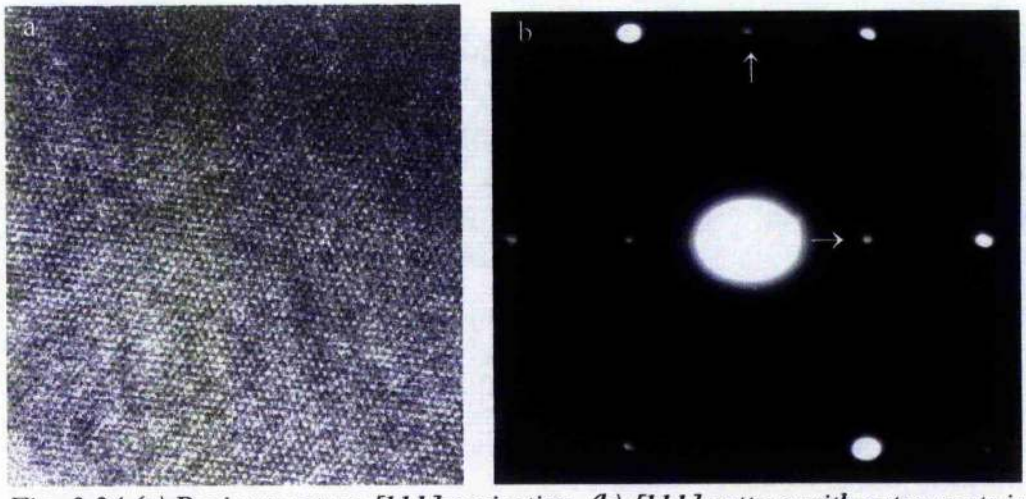

Fig. 3.34 (a) Basic structure [111] projection, (b) [111] pattern with extra spots in one crystal of $Ba_{0.5}Bi_{1.5}O_3$

The diffraction pattern above (*Fig. 3.34b)* is the basic cubic [111] structure, however there is also the presence of weak satellite diffraction spots, the structure has been

changed in some way in the two minutes elapsing from the capture of the original pattern to the imaging of that exact area at high magnification.

The EDS quantitative analysis of the area shows, a slight decrease in the Bi quantity.

EDX FROM AN AREA WITH WEAK SPOTS AND BASIC PATTERN DIFFRACTION

Elmt	Peak Area	Stat. Sigma	k Factor	Abs. Corrn.	Element weight %	Sigma %	Atomic weight %
Ba L	2118	151	2.029	1.000	25.39	1.68	34.11
Bi L	4284	225	2.947	1.000	74.61	1.68	65.89
Total					100.00		100.00

It is apparent that the strong electron beam has had an effect on the structural detail in the sample. The EDS analysis taken from 20 separate particles CBi/Ba=2.35±0.35 is down by a small margin on the expected result for this sample of 3. As has been mentioned, disassociation of the Bi leads to local structure change mainly due to loss of the Bi atoms. This may in turn lead to other Bi atoms or Ba and O atoms replacing the vacancies. One other hypothesis may be that the Bi loss at one specific area of the crystal leads to disorder and disruption at another, in other words a kind of "ripple effect"

An observed superstructure may revert back to the basic structure, as Bi quantity levels off with Ba. Conversely loss of Bi could also lead to a change in crystallography as in the case in the previous page *(Fig. 3.34)*.

These anomalies can be overcome using a weak electron beam and some haste in imaging at high resolution, after obtaining the original diffraction pattern. With the advancement of modern high resolution transmission electron microscopes, which are equipped with a double condenser and intermediate lens, it is possible to obtain good high resolution images at the atomic level along with SAED patterns. This is even the case for those samples which are most unstable under the electron beam. A small spot size is also very useful for such material. The diffraction patterns *(Fig. 3.35)* and the

corresponding images *(Fig's. 3.36, 3.37)* were taken using a fairly small SAED aperture and a small spot size.

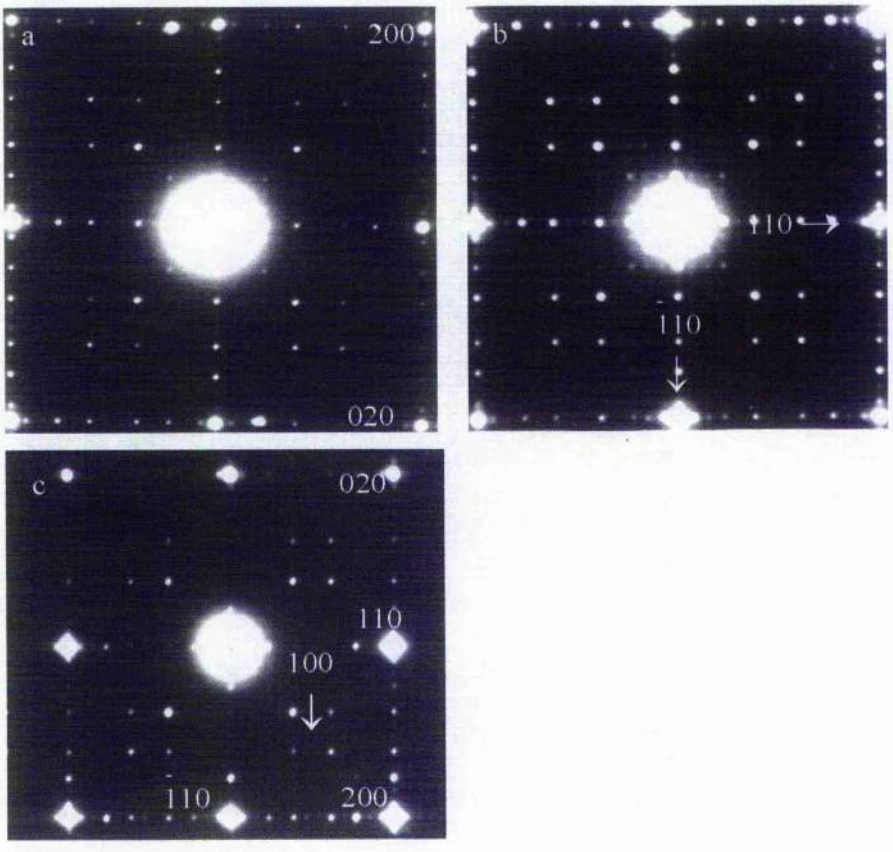

Fig. 3.35 (a) Shows the [001] projection with superlattice spots, (b) indexed [001] incommensurate pattern, (c) enlarged image showing pattern along [001] of an area of $Ba_{0.5}Bi_{1.5}O_3$ containing an incommensurate 5x5 island structure.

The diffraction patterns along the [001] transverse zone shown above (*Fig's. 3.35 a-c)* show a large diversity of details. The patterns consist of square arrays of relatively very intense spots with $h + k$ = even, revealing the basic perovskite lattice. The spots with $h + k$ =odd totals, such as [100] are shown along with their associated positions. The 000-110 line segment i.e., the diffraction vector [110]* and also the diffraction vector [200]* is divided into four non equal intervals by satellites spots. The structure

appears to be incommensurate. The intensities of the satellites decrease with the corresponding, either actually present or potentially present perovskite spot.

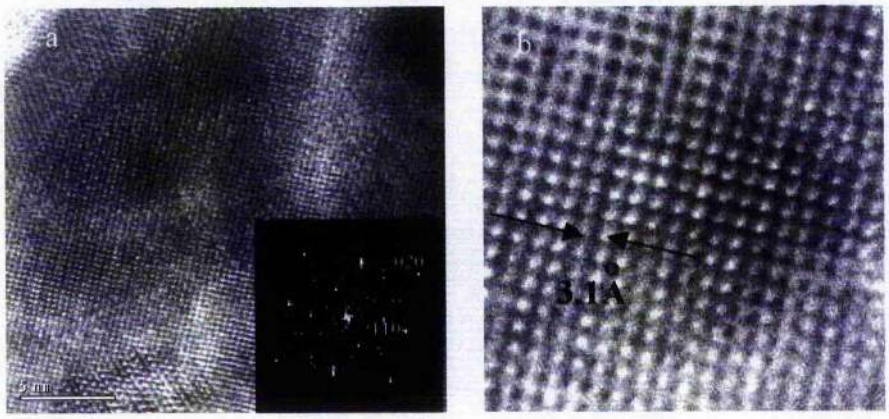

Fig. 3.36 (a) [001] HRTEM image, (b) Masked enhanced image of $Ba_{0.5}Bi_{1.5}O_3$.

Fig's. 3.36 show the corresponding HRTEM images for the diffraction patterns shown in *Fig's. 3.35*, the image is along the [001] zone. From the periodic arrangement of bright dots it can be deduced that the structure is fragmented into an incommensurate island structure.

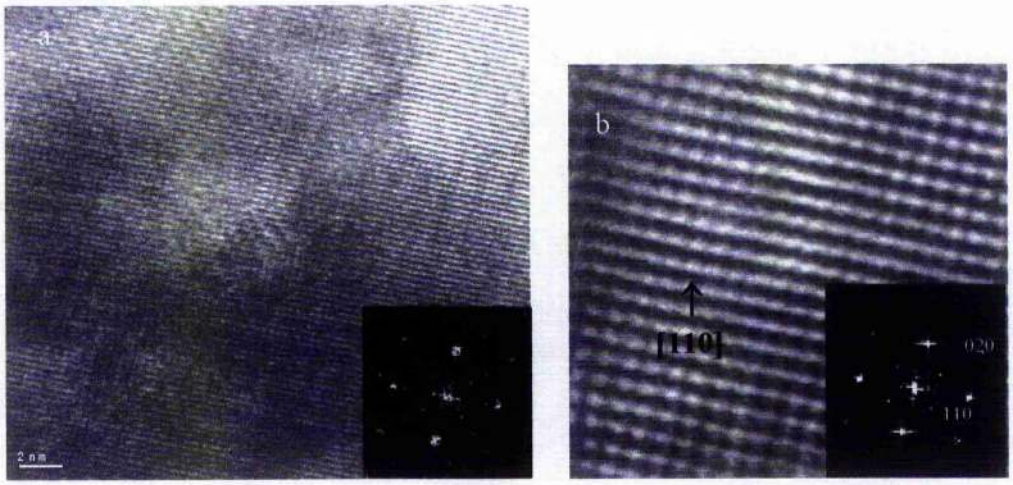

Fig. 3.37(a) [001] projection with FFT inset, (b) [001] zone axis Image from $Ba_{0.5}Bi_{1.5}O_3$ *after masking.*

Fig's. 3.37 show another area of the same crystal showing the same repeat pattern. These images along the [001] zone correspond to the diffraction patterns *(Fig's. 3.35)* showing an incommensurate island structure.

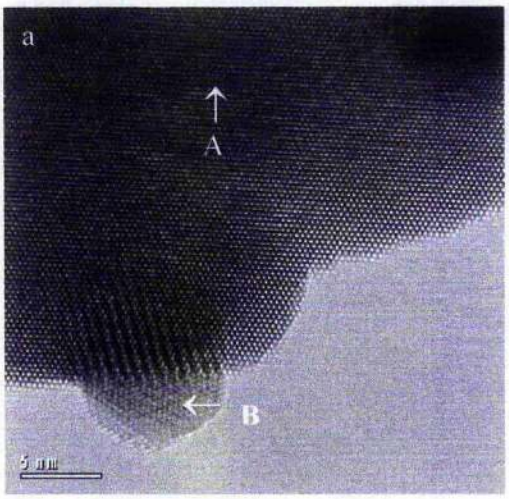

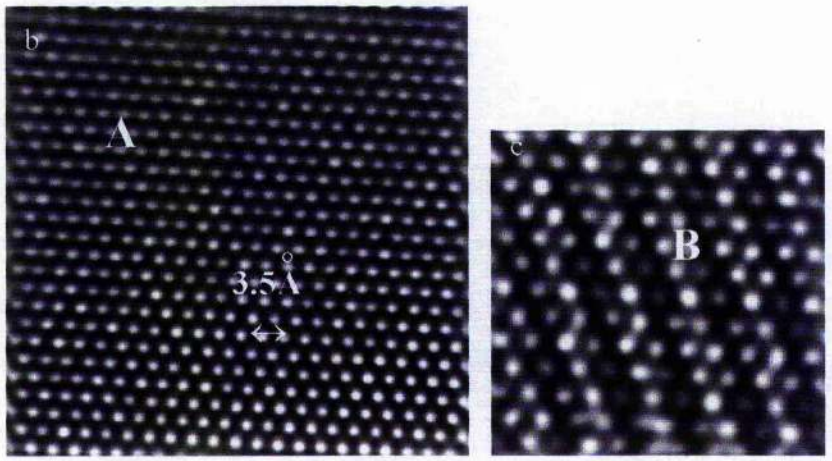

Fig. 3.38(a) Region A is basic [111] region, B is decomposing area of the crystal $Ba_{0.5}Bi_{1.5}O_3$, (b) enhanced image of region A, (c) Enhanced image of region B from $Ba_{0.5}Bi_{1.5}O_3$.

Fig's. 3.38a-c are images showing a crystal with two distinct areas. The main area A has the basic [111] perovskite structure, where area B has some evidence of distortion. The distortion appears in an area, which is dissociating from the main body of the crystal. It is thought, as discussed before, that Bi de disassociates under the electron beam and

escapes from the crystal. The composition of the material left behind may then be Bi deficient and revert back to its basic perovskite form.

Fig's. 3.38b,c show these areas in much clearer detail. The images are post masking. This phenomenon may be the reason that many patterns in this composition show basic perovskite structure (*Fig's. 3.39)* rather than the fact that the solid solution is not single phase or homogenous.

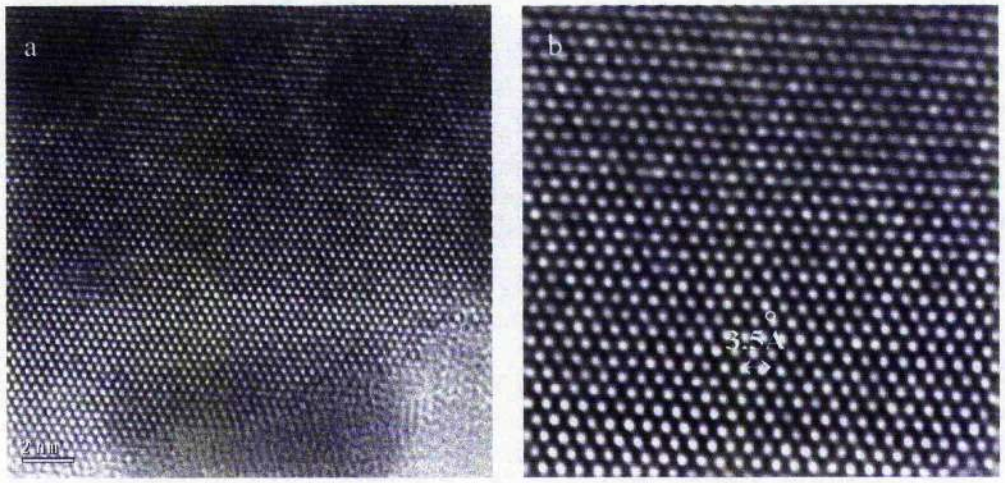

Fig. 3.39(a) [111]projection basic cubic structure, (b) Enhanced image from $Ba_{0.5}Bi_{1.5}O_3$.

The above two images show the basic [111] perovskite structure found in many crystals of $Ba_{0.5}Bi_{1.5}O_x$, this could be due to the disassociation of the crystal.

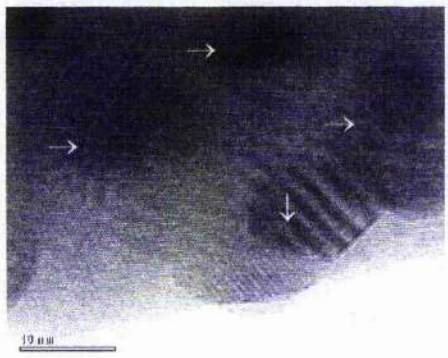

Fig. 3.40 Beam exposure leads to many structures (domains) within one crystal of $Ba_{0.5}Bi_{1.5}O_3$.

Fig. 3.40 is an image of a crystal after exposure to electron beam of only a few minutes. Many separate areas with differing structures can be seen (arrows). Each area is at a different stage of Bi disassociation. Elemental composition for each domain may also differ greatly, as was seen from the EDS study undertaken previously (*Fig. 3.31).*

One other diffraction pattern *(Fig. 3.41)* with strong superlattice was recorded from this Bi rich solid solution. *Fig's. 3.41* shows a diffraction pattern along the [111] zone, this pattern is divided into six equal parts of this hexagonal pattern. Each section consists of incommensurate diffraction spots.

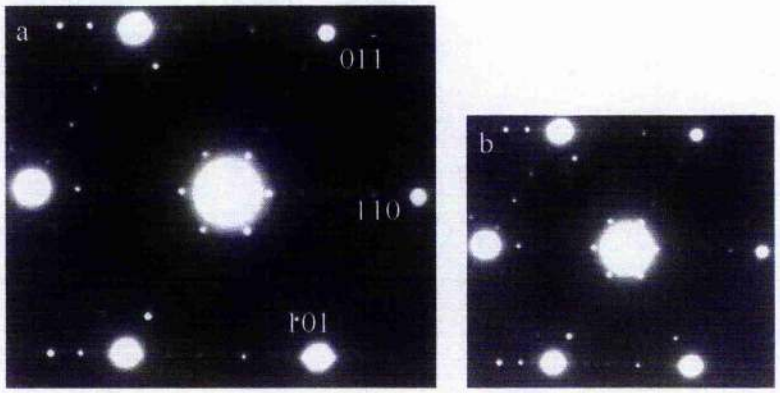

Fig. 3.41(a) Diffraction pattern in the [111] projection, (b) Superstructure (arrowed) from a sample of $Ba_{0.5}Bi_{1.5}O_3$ along the [111] zone axis.

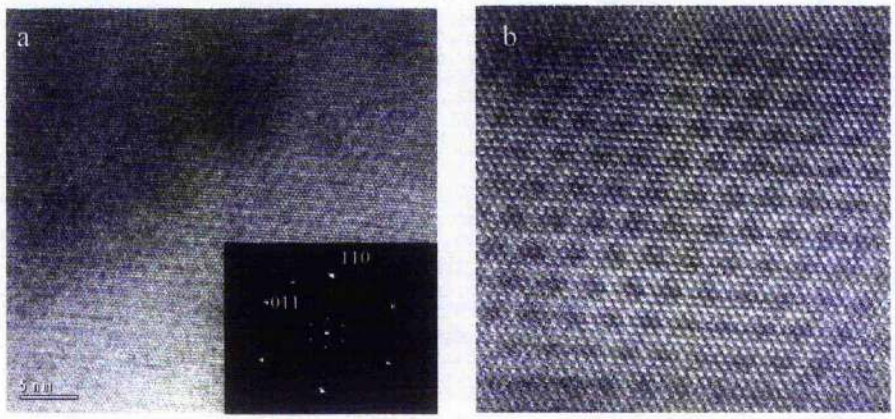

Fig. 3.42(a) [111] projection and corresponding FFT, (b) Image showing superstructure in $Ba_{0.5}Bi_{1.5}O_3$.

Fig's. 3.42a,b show the corresponding HRTEM images for the diffraction pattern shown in *Fig. 3.41* in the [111] zone. *Fig. 3.42a* is the original image with the FFT image inset. The FFT diffraction pattern clearly shows the extra superlattice spots in the [111] pattern. The superlattice fringes can also be seen in *Fig. 3.42b,* this second image is after masking of the FFT pattern.

Direct imaging by HRTEM such as the images taken above is well suited to gain information on the origin of the superstructures. It is important to note that along a cube direction of perovskite different sublattices of heavy atoms are imaged as dots of a different brightness. The various ordering patterns may also be in part due to the presence of Bi^{5+} and Bi^{3+} in various proportions in the different compounds. It is also possible that an anion deficiency can also lead to the formation of island structure such as those shown in *Fig. 3.35* and *Fig. 3.41.*

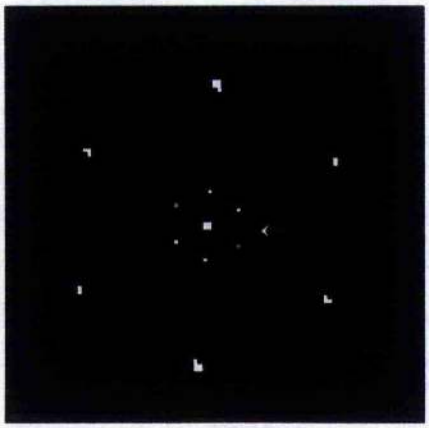

Fig. 3.43 is an enlarged image of the SAED pattern taken from a sample of $Ba_{0.5}Bi_{1.5}O_3$ in the (111)zone axis, the superstructure is arrowed.

This superstructure *(Fig. 3.43)* may also have arisen from the high proportion of defects within the composition due to greater deviation from stoichiometry. The superlattice may correspond to the distortion of the cubic unit cell, caused by the short term ordering of the cations and perhaps a displacement of the oxygen atoms *(Cox and Henrich 1994)*. If however the oxygen sites and the cation sites are fully occupied, the excess Bi cation may have been accommodated within the channels formed by the

corners of the columns giving rise to the superstructures seen in $Ba_{0.5}Bi_{1.5}O_3$. Defect ordering in $Ba_{0.5}Bi_{1.5}O_3$ could also have led to vacancies being assimilated into the structure thus leading to a large supercell of the basic cubic structure. However A site doping by excess Bi without question leads to B cation deficient perovskites (*Cox and Sleight 1976), (Microstructure in the* $BaPb_{1-x}Bi_xO_3$ *system*) and ordering of these vacancies may also lead to the formation of the superstructures observed in $Ba_{0.5}Bi_{1.5}O_3$.

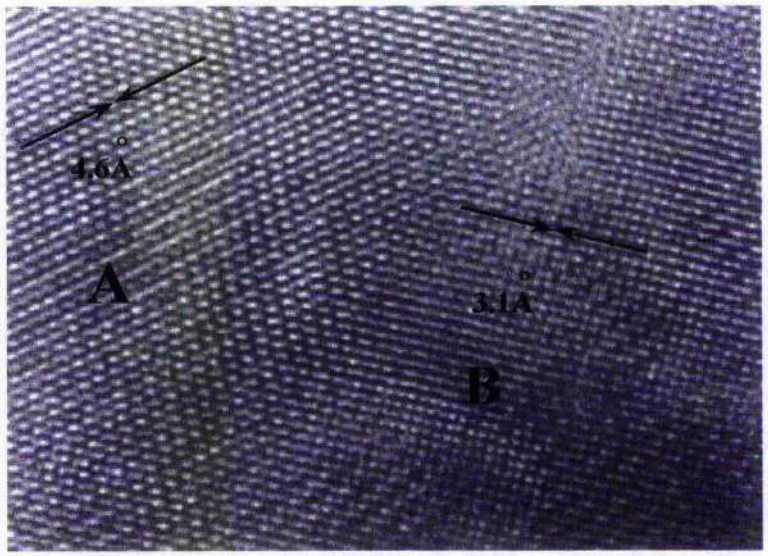

Fig. 3.44 Area showing two distinct domain regions (A+B) in $Ba_{0.5}Bi_{1.5}O_3$.

Finally *Fig. 3.44* is taken from one area of a single crystal from a solid solution of $Ba_{0.5}Bi_{1.5}O_x$ with two distinct domains, A and B. The d-spacing values for each show, that despite being supposedly of the same composition, the unit cell parameters differ. One theory as to why this has arisen suggests that successive perovskite blocks are related by a displacement of half $[111]_p$ caused by the presence of NaCl like bilayers of BiO *(Nikolaichik et al 2002)*. This is just another interesting structural phenomenon related to this particular composition, which merits further investigation. It may be that the structural changes in the crystal alter the electrical properties of the solid in significant ways.

3.9 Further research

Intended future work will involve continuing research on the structural analysis of the $BaBiO_3$ system and particularly the successful synthesis of Bi rich solutions and their subsequent structural analysis using powder XRD, EDS, Selected Area Diffraction and HREM imaging. It is hoped that future work to use smaller steps, e.g. x=0.03 or even x=0.02 for $Bi_{1\pm x}Ba_{1\mp x}O_3$

In addition future work will also include further micro and structural analysis of: 1. zeolites and 2. metal oxides and in particular the structural changes taking place around the metal-insulator transition in these compounds using the above techniques.

3.10 Further discussion and conclusions

For the Ba ($x \geq 0.2$) compounds there is a marked increase in structural change. This is due to the greater amounts of Ba substituted for Bi. Firstly in the XRD pattern the pseudocubic reflection split, suggesting that the difference between a_p, b_p and c_p is larger than in $BaBiO_3$. Secondly a number of extra peaks commensurate with the unit cell appear, this concludes that the symmetry of the cell has changed, peaks also appear that do not fit with the $\sqrt{2}a_p \times \sqrt{2}b_p \times 2c_p$ cell but appear to be consistent with a supercell based on the $\sqrt{2}a_p \times \sqrt{2}b_p \times 2c_p$ $BaBiO_3$ unit cell. These findings were once again confirmed by satellite spots present in the SAED patterns for these compounds. The satellite spots in the patterns could not be indexed to the basic unit cell.

Results suggest that a small proportion of Ba substitution on the A-sites ($x \geq 0.2$) result in the difference between the three crystal dimensions a_p, b_p and c_p and therefore to the formation of a supercell. This could be a consequence of the ordering of the Bi and Ba on the A-sites. These interesting structural properties require further study, using the above techniques in order to fully understand the effects of A and B site substitution by either Bi or Ba.

Prolonged exposure to a strong electron beam could result in the emergance of additional satellite spots as is the case in the Bi rich material. Bi is sensitive to a strong electron beam, it disassociates. However information can be gained from Bi rich solutions using a less strong beam. Using this method the electron doping of $BaBiO_3$ has been successfully studied by the preparation of phases in the $Ba_{1-x}Bi_{1+x}O_3$ system ($x \leq 0.5$).

The structure of these different phases proved to be of considerable interest. The substitution of Bi for Ba has a subtle effect on the symmetry of this perovskite material. There is a general trend towards a body centred pseudocubic cell. This is consistant with the presence of Bi ions on the A sites of the perovskite lattice. Ordering, possibly of the A-site cations is suggested by the observation of satellite spots in the SAED patterns.

For $Ba_{0.5}Bi_{1.5}O_3$, ordering may be observed by XRD, however this is much more conclusive in that many crystals display satellite spots in the SAED patterns.This may indicate long range incommensurate ordering. The Bi rich compounds studied in this thesis exhibit a variety of composition- dependent often "local" superstructures that are derivatives of the perovskite basic structure.

In the Bi rich x=0.5 sample the composition presumably differs from the simple ones. The (001) layer- like perovskite blocks are fragmented into square incommensurate islands and are limited by the (110) planes, creating a second level of superstructures accommodating these deviations from simple compositions. The various ordering patterns may be also in part due to the presence of Bi^{5+} and Bi^{3+} in various proportions in the different compounds.

ED and HRTEM images determine local structures, where as the chemical compositions refer to averages over much larger volumes, this may lead to differences between the expected structures and the supposed chemical composition. HRTEM imaging and SAED has provided an increased and important understanding of the structure of this system. Although the Bi^{3+} and Bi^{5+} are each co-ordinated to six oxygens in a slightly distorted octahedral arrangement, the Bi-O distances are different for the two B cations. Bi^{5+} being 2.12Å and Bi^{3+} in the region 2.35-2.4Å.

It appears that $BaBi^{3+}Bi^{5+}O_3$ represents not only the first example of Bi^{3+} cations

octahedrally coordinated to oxygen but also the first example of an ordered perovskite structure in which the ordered cations are the same element. Sometimes the B cations in $A^{2+}B^{3+}B^{5+}O_3$ are not completely ordered. The lack of order is due to kinetic rather than thermodynamic factors. In $Ba^{2+}Bi^{3+}Bi^{5+}O_3$ only ordering of Bi^{3+} and Bi^{5+} is required to attain an ordered structure. However this ordering is accompanied by lattice disorder, which stabilize the disproportionation of Bi^{4+} into Bi^{3+} and Bi^{5+}. Partial ordering of Bi^{3+} and Bi^{5+} and displacements of the Bi^{3+} cations or the oxygen anions could lead to the superstructures observed in the Bi rich solid solutions represented in this project.

When one of the two cations present in ternary compound such as $BaBiO_3$ is an **A** metal such as Ba, it will have empty orbitals considerably higher in energy than the transition metal *d* levels, and its influence on electronic structure will be limited. Post transition **B** metals such as Bi however have *s* orbitals which may be filled, in the same energy range as the *d* band.

Interaction between the two cations, Ba, Bi either by direct overlap or indirectly via an anion, can broaden the *d* band therefore it can be said to be metallic. This could be due to the involvement of the 6*s* electrons present in Bi^{3+}, therefore it could be the case that if there is increase in Bi there is more conductivity.

One other factor which may give rise to metallic behaviour occurs when extra electrons are added to a solid solution. This leads to increased motion of the electrons (or holes) without incurring additional electron repulsion, this in turn leads to lattice distortion and delocalisation.

These phenomena could be caused by increased levels of one cation over the other (Ba, Bi) and may also lead to the superstructure observed in the SAED patterns and HRTEM imaging. The various ordering patterns in the Bi rich samples may be in part also due to the presence of Bi^{3+} in various proportions in the different compounds. Oxygen content may also be important, in particular the presence of oxygen vacancies, which may also be responsible for the superstructures observed. Finally the unit cell size itself could be increased or decreased depending on the doping cation *(Appendices A and B)*. An increase in molar % of Ba increases the size of the unit cell, an increase in the molar% of Bi decreases the unit cell size.

Chapter 4 Mesoporous Solid Materials

4.1 Metal clusters in mesoporous materials

MCM-41 possesses a hexagonal arrangement of uniformly sized mesopores (15 to 100 Angstroms), which are controlled using a surfactant as the templating agent *(Fig. 4.1)*.

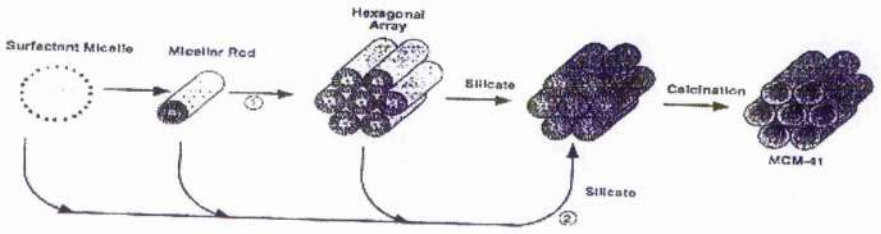

Fig. 4.1 Mechanism for the formation of MCM-41 using surfactant as the templating agent.

MCM-41 (Mobil Crystalline Material) is a silicate obtained by a templating mechanism. It is ordered to some degree, so that there are arrays of non intersecting hexagonal channels, identifiable by TEM, XRD, and vapour adsorption. By changing the length of the template molecule, the width of the channels can be controlled to be within 2 to 10 nm *(Beck et al 1992)*, the walls of the channels are amorphous SiO_2. This feature, together with its exceptional porosity (up to 80%), makes MCM-41 the least mechanically stable compared to, *e.g.*, other porous silica's, silica gels or zeolites.

One method to modify the physico-chemical properties of mesoporous materials is by introducing metal clusters into the channels. Small metal particles exhibit electronic, catalytic, optical and other properties, which differ from those of the corresponding bulk metals. Mono- and bi-metallic nanoparticles in the size range 0.5 – 5nm have a particular interest because of their catalytic properties *(Sinfelt 1983)*.

In the last few years or so various metal clusters i.e.: Ag_3 Ru_{10}, Ru_6, Ru_{10}, Ru_{11} etc have been loaded into MCM-41 silica by means of introducing their parent organo metallic compounds *(Zhou 1999)*. In the following samples ruthenium was loaded in the

form of metal clusters. Ruthenium is a hard white metal and has four crystal modifications. It does not tarnish at room temperature, but oxidises explosively. The metal is one of the most effective hardeners for platinum and palladium and is alloyed with these metals to make electrical contacts for severe wear resistance. A ruthenium-molybdenum alloy is said to be superconductive at 10.6K. HRTEM has been a powerful tool to investigate these nanoparticles within the porous channels.

It is important to know whether the clusters have been introduced into the actual mesopores. Since HRTEM can image local structures, it is not difficult to distinguish whether the clusters are inside the channels or merely deposited on the outer surface of the mesopores. Silicon is amorphous; it therefore follows that the samples with more free Si (not attached to the micelle framework) will have a more amorphous look while those with less free Si will be more structured. Si ions in these samples have regular tetrahedral co-ordination of oxygen. These SiO_4 units randomly join together by sharing of Oxygen atoms to form an amorphous framework, *(Zhou 1999)*. This should be clearly evident when EDS chemical analysis is undertaken. All samples were supplied by Prof Duncan Bruce, University of Exeter, Department of Inorganic Chemistry. The samples were **Racemic**. A Racemic sample is a mixture of equal quantities of the *d* and *l* forms (equal amounts of left and right-handed isomers) of an **optically active** compound. In all the cases studied the samples were synthesised by templating a silicate around a surfactant Ru complex using the **high concentration, true liquid crystal templating approach** *(Danks et al 2002)*.

$Ru_{42}C_{12}SiO_2$ (Racemic as synthesised)

EDS chemical microanalysis (*Fig. 4.2)* was carried out on the sample using ISIS on the 2011 TEM. This was done to ascertain whether Ru quantity within the sample was within the expected limits.

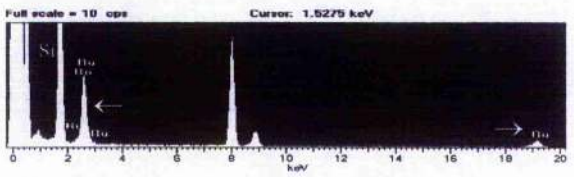

Fig. 4.2 EDS microanalysis $Ru_{42}C_{12}SiO_2$(Racemic) sample showing two ruthenium peaks (arrowed).

This sample was annealed above ambient temperature; the template was then partially washed out. The microanalysis spectrum shows two ruthenium peaks, Kα 19.2365keV and Lα 2.5586keV. Peak size for Ru in this sample is within the expected range. The Peak to the left of the Ru Lα is the Si Kα peak; this has a strong intensity and is expected. High-resolution images *(Fig's. 4.3a,b)* were taken using the Gatan CCD digital camera on the 2011 TEM.

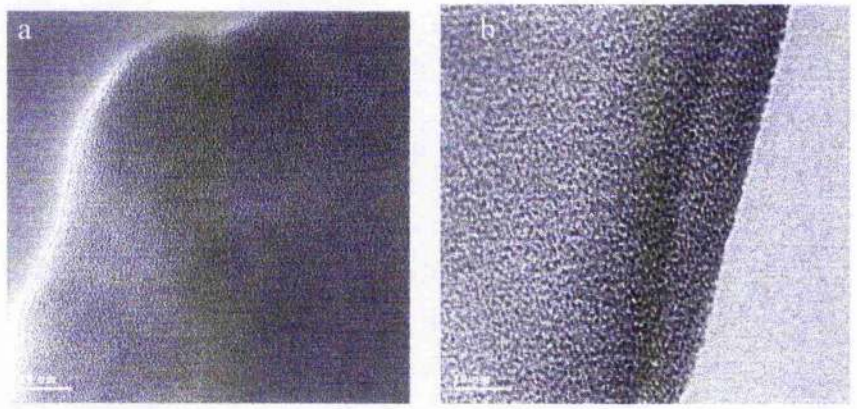

Fig. 4.3(a) No structure in evidence, (b) Underfocus amorphous image of $Ru_{42}C_{12}SiO_2$*(Racemic).*

No ordered structure can be seen in the $Ru_{42}C_{12}$ (as synthesised) sample, both of the above images are taken of an amorphous sample before extraction. The white line on the outside of the particle, confirms that the image has been taken at slightly under focus on the microscope, the supposed "ideal" conditions for transmission electron microscope images.

$Ru_{42}C_{12}SiO_2$ (Racemic extracted)

This sample was again annealed above ambient temperature however this time the template was washed out completely. EDS microanalysis *(Fig. 4.4)* was carried out on the $Ru_{42}C_{12}$ (extracted) sample to confirm that a proportion of the Ruthenium had been extracted along with the organic micelle structure. This was also a **racemic** sample, as opposed to a sample, which is **resolved**. A resolved sample is one that shows **optical activity** and has no plane of symmetry. The commonest case of this is in organic

compounds in which a carbon atom is linked to four different groups. An atom of this type is said to be a **chiral centre**.

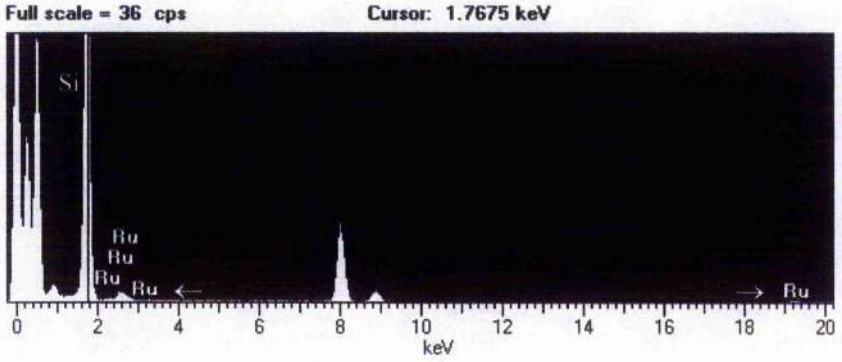

Fig. 4.4 $Ru_{42}C_{12}SiO_2$ (extracted) sample showing small Ru peaks.

The spectrum shows that the peak intensity for both Ru Kα and Lα has diminished markedly (arrows) from that of the "as synthesised " sample. The Si Kα peak is still very prominent.

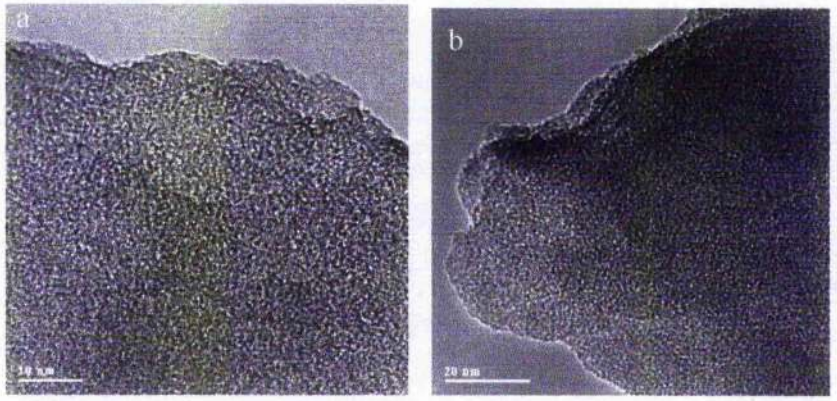

Fig. 4.5(a) Underfocus amorphous $Ru_{42}C_{12}SiO_2$ (Extracted) sample, (b) No visible structure is present.

As with the synthesised sample the extracted sample appears amorphous. There appears to be no apparent structure or mesoporous structure.

$Ru_{42}C_{19}SiO_2$ (Racemic as synthesised)

This sample was annealed at above ambient temperature and the surfactant partially washed out. The sample was analysed *(Fig. 4.6)* for Ru content.

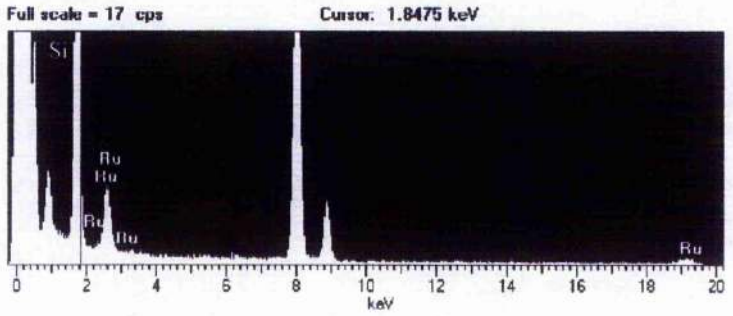

Fig. 4.6 EDS for $Ru_{42}C_{19}SiO_2$ (Racemic as synthesised).

The two Ru peaks, Kα and Lα, are once again prominent. The Si Kα peak is also showing strongly.

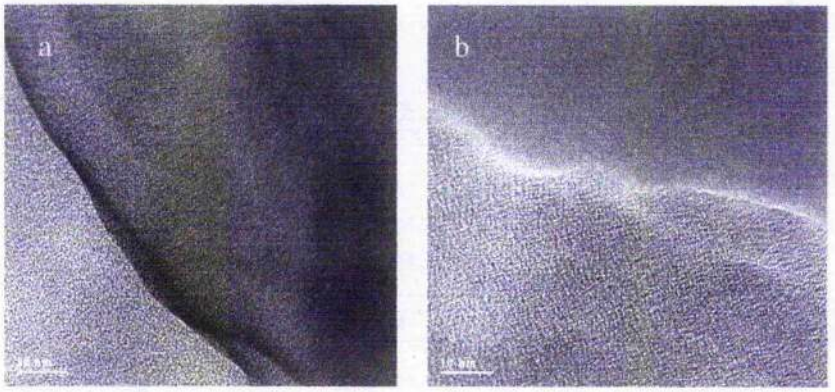

Fig. 4.7(a) On focus image, no structure, (b) Under focus image of $Ru_{42}C_{19}SiO_2$ (Racemic as synthesised).

The structure of Ru_{42} C_{19} (As synthesised) is amorphous *(Fig's. 4.7)*, no ordered structure is evident.

$Ru_{42}C_{19}SiO_2$ (Racemic extracted and calcined at 350°C)

This sample was synthesised as that above, annealed at above ambient temperature however the surfactant was then wholly extracted and the sample calcined at 350°C. Microanalysis *(Fig. 4.8)* was then once again performed to obtain information on the Ru and Si content of the sample.

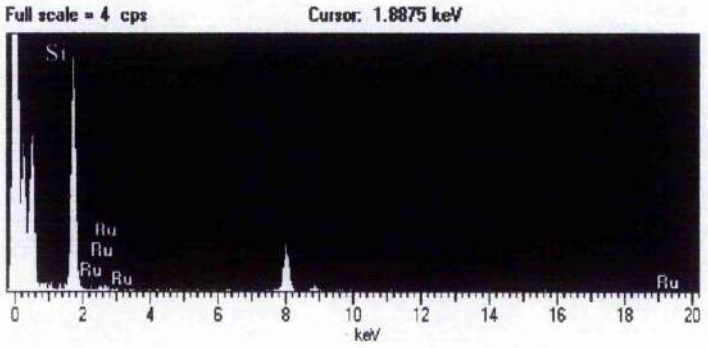

Fig. 4.8 EDS spectrum showing $Ru_{42}C_{19}SiO_2$ (Racemic extracted and calcined at 350°C).

The spectrum shows that the Ru peaks, Kα and Lα, have all but disappeared. The Si Kα peak is weaker than before. The micronalysis spectrum was acquired from an area on a crystal with distinct mesoporous channels.

There is a very strong interaction between the electron beam and the mesoporous specimens examined in this section. This interaction leads to multiple scattering of electrons, which in turn leads to a very complicated image contrast. Most mesoporous samples have a very large unit cell and therefore multiple scattering must be taken into consideration. These samples are generally not prone to problems such as moisture absorption as the inner surface of the samples are lyophobic and the pore size is large, this allows for fast desorption and diffusion of water. Because of this the samples are less sensitive to the electron beam. Since the unit cell is very large, low magnification images are usually sufficient for studying these materials. Only after many minutes under the beam will the material disassociate into amorphous silica. This can be overcome in some extent by using a weak beam in conjunction with a small spot size.

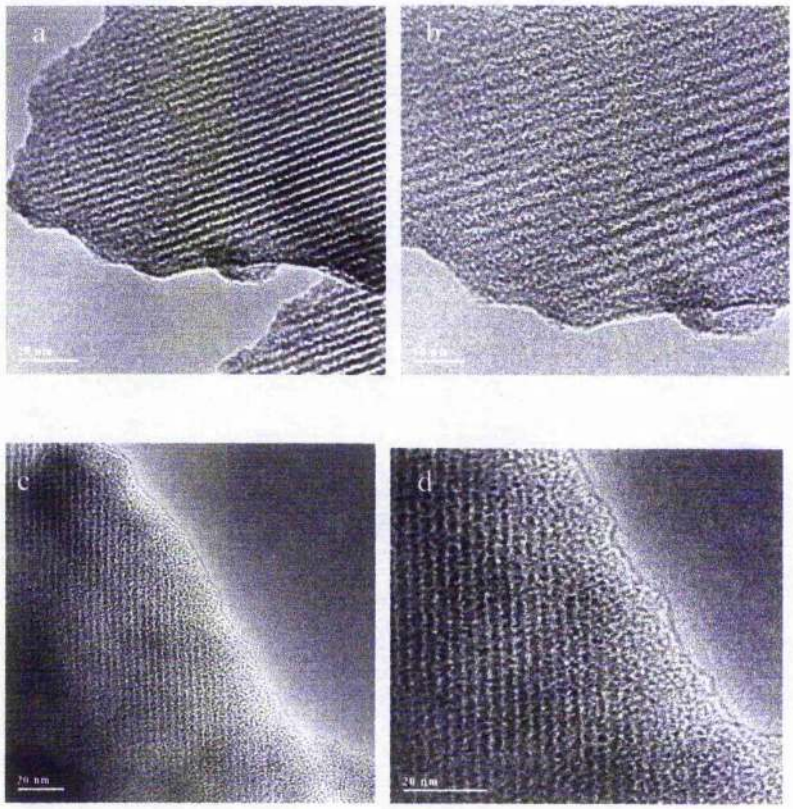

Fig. 4.9(a) Underfocus with channels, (b) Overfocus weak channels, (c) Overfocus with channels, (d) Overfocus image of $Ru_{42}C_{19}SiO_2$ (Racemic extracted and calcined at 350℃)

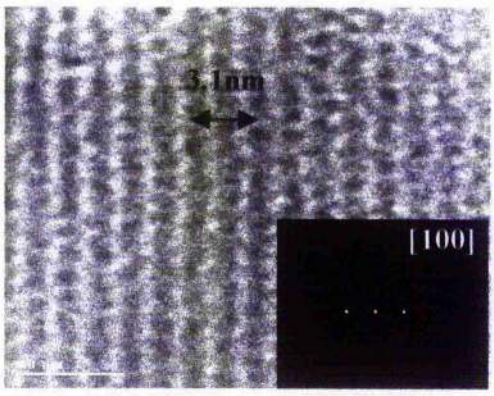

Fig. 4.10 Mesoporous channels are clearly seen. No evidence of Ru metal clusters within the channels from $Ru_{42}C_{19}SiO_2$ (Racemic, extracted and calcined at 350℃)

The images for this sample show strong structure in the form of mesoporous channels. The contrast is very strong in these channels and they are easily resolved using HRTEM. The difficult task of these microscopy studies is to detect metal clusters in the channels of these samples.

Fig's. 4.9a-d show the channels very clearly, the interline distance is approximately 3.3nm. *Fig's. 4.9c-d* show the mesoporous channels running from top to bottom of the image. Channel width appears to be approximately 3.1nm *(Fig. 4.10)*. The Fourier transform of *Fig. 4.10* is shown inset. From both the real space image and reciprocal space (diffraction) pattern an average repeat distance (3.1 nm in real space) is obtained. Despite the obvious structure in these particles there is no evidence of Ru clusters in the channels.

$Ru_{42}C_{19}$ SiO_2 (Racemic, extracted, surfactant reintroduced and calcined at 350° C)

In this sample the surfactant was firstly removed and then put back into the sample (to give an increase of loaded Ru in the channels). The sample was then calcined at 350° C, with the template probably firstly removed. The sample was analysed *(Fig. 4.11)* for Ru and Si content using the ISIS microanalysis system.

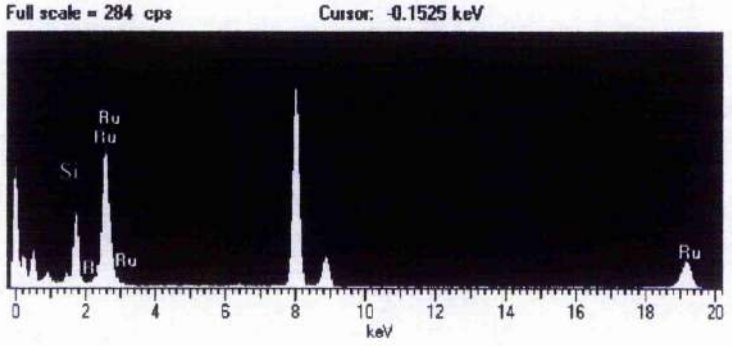

Fig. 4.11 EDS from $Ru_{42}C_{19}$ SiO_2 sample which is Racemic, extracted, surfactant reintroduced and calcined at 350°C.

The spectrum shows a higher Ru Lα peak and a lower Si Kα peak than that of the previous samples, the Ru Kα peak has also increased slightly in intensity. These are

encouraging conditions for channel formation; the question now to be answered, using TEM, is whether or not there are clusters of Ru metal particles within the channels. In some cases Ru clusters may be present but are not located within the channels. In such cases there may be a strong indication of Ru presence by EDS microanalysis, however HRTEM studies will show that the clusters are outside the channels. The following images show clearly that this is not the case and that the clusters are in the channels.

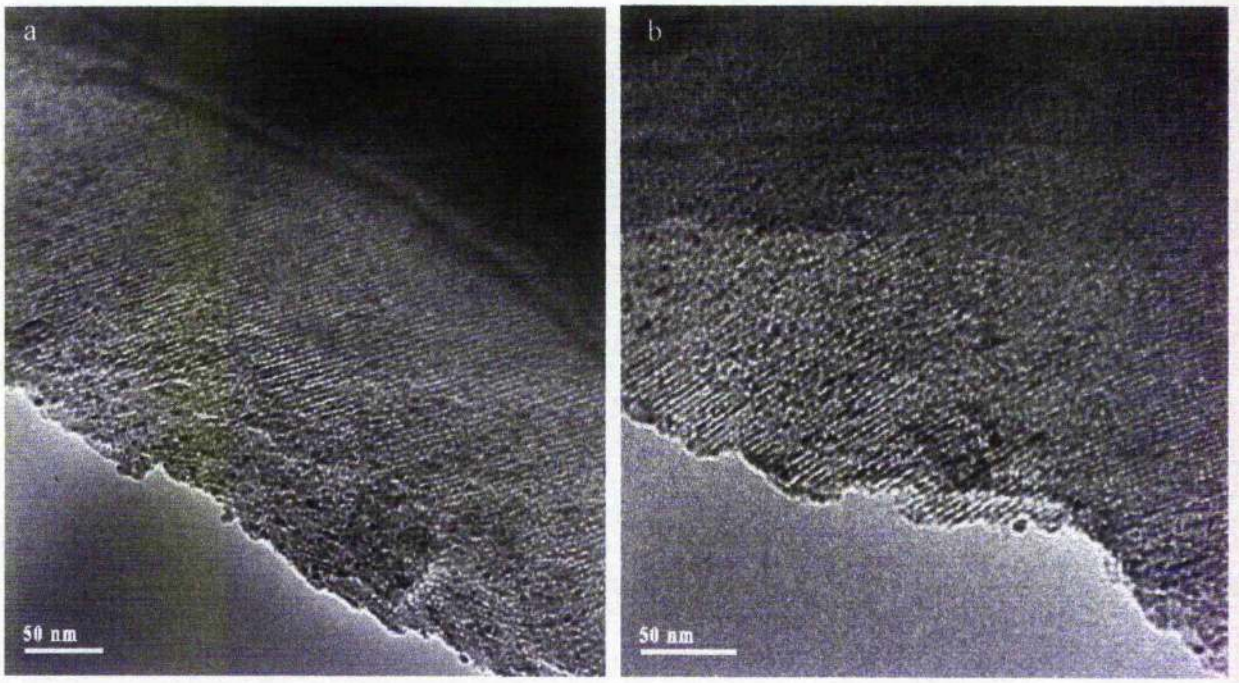

Fig. 4.12(a) Channels present with Ru, (b) Ru appears to be in the channels in $Ru_{42}C_{19}$ SiO_2 *(Racemic, extracted, surfactant reintroduced and calcined at 350°C).*

Fig's. 4.12a,b show HRTEM images of Ru loaded mesopore channels. The interline distance is about 3.1nm. The small Ru clusters appear to follow the route of the MCM-41 like channels. However these images are not in themselves enough to say whether the Ru particles are in the pores themselves. A very distinct white line is seen to border the crystal image, this is called a Fresnel fringe, this shows clearly that the image has been taken at the under focus position.

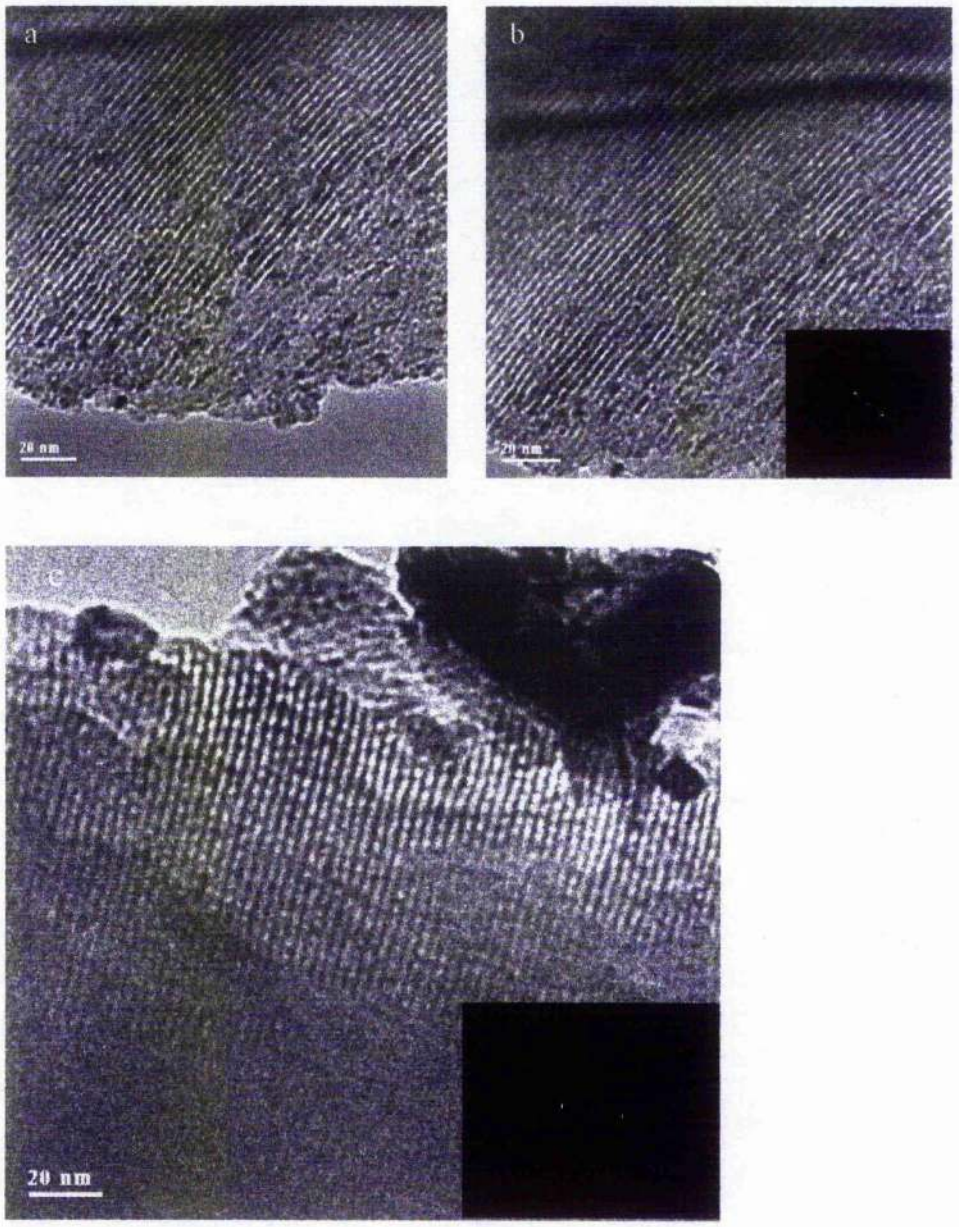

Fig. 4.13(a) Channels with Ru clusters, (b) Image with clusters and FFT inset, (c) Underfocus image with FFT inset taken from $Ru_{42}C_{19}SiO_2$ (Racemic, extracted, surfactant reintroduced and calcined at 350 °C).

Fig's. 4.13a-c show Ru metal clusters following the route of the mesoporous channels. The metal clusters show as the black dots partially ordered along the pore axis. The corresponding Fourier transforms with diffraction lines are shown inset. From both the real space image and reciprocal space (diffraction) pattern an interline distance of approx 2.8-3nm is obtained. The great advantages of HRTEM studies in this field is its ability to directly observe the mesopore systems, surface structures, local defects, morphology and sizes of the particles and even the metal nonoparticles loaded inside the mesopores. When viewed in a direction perpendicular to the pore axis a stripe pattern is observed only *(Fig. 4.9)*. However when metal nanoparticles are loaded into the mesopores the HRTEM images *(Fig's. 4.12,13)* show many extra black dots lined up along the channel direction, they may however be disordered or only partially ordered "Rosary pattern" *(Zhou 2000)*. When HRTEM images were recorded from underfocus *(Fig. 4.9a)* to overfocus *(Fig's. 4.9b,c)* structural differences were highlighted.

4.2 MCM-41-Like mesoporous materials

This material has the simplest structure of the mesoporous family. In HRTEM most information can be obtained when viewing down the pore axis and in a direction perpendicular to the pores. The main objective when looking at the following samples is to look for ordering in the wall.

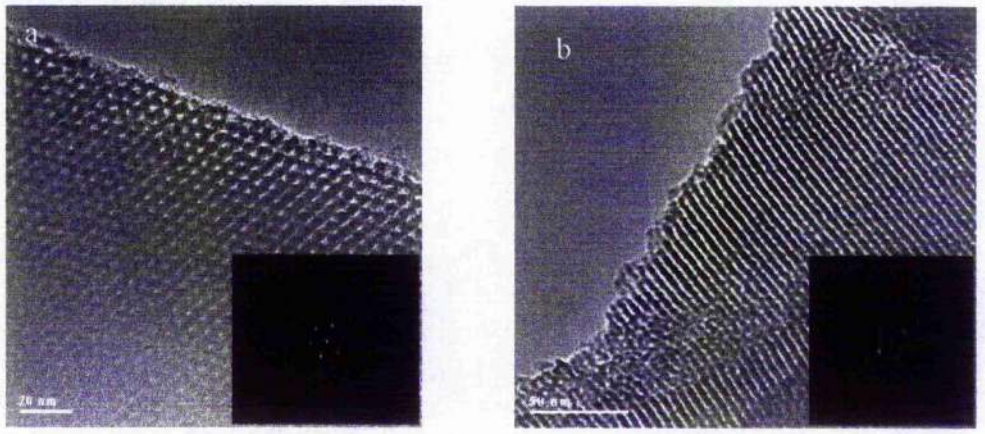

Fig. 4.14 (a) ordered pore structure with corresponding FFT, (b) different area of the same crystal with disordered structure of the pore walls.

Fig. 4.14a shows an image with an ordered pore structure; the pore diameter is approx 5nm. Inset of this image is the corresponding FFT. *Fig. 4.14b* shows disorder of the pore walls viewed down the (100) direction, the interline distance is approx 4.5nm long. Inset is the FFT image in the (100) direction.

MCM-41and related mesoporous materials have particular interest due to the work to expand the pore size's of zeotype materials from the micropore to mesopore region, this is in response to increasing demands in both industrial and fundamental studies. The images above seem to show a molecular sieve with exceptionally large uniform pore structures. The characteristic of this material is one of a well-defined pore structure with apertures in the range 4-6nm which can potentially be controlled by careful choice of surfactants, auxiliary chemicals, and reaction parameters.

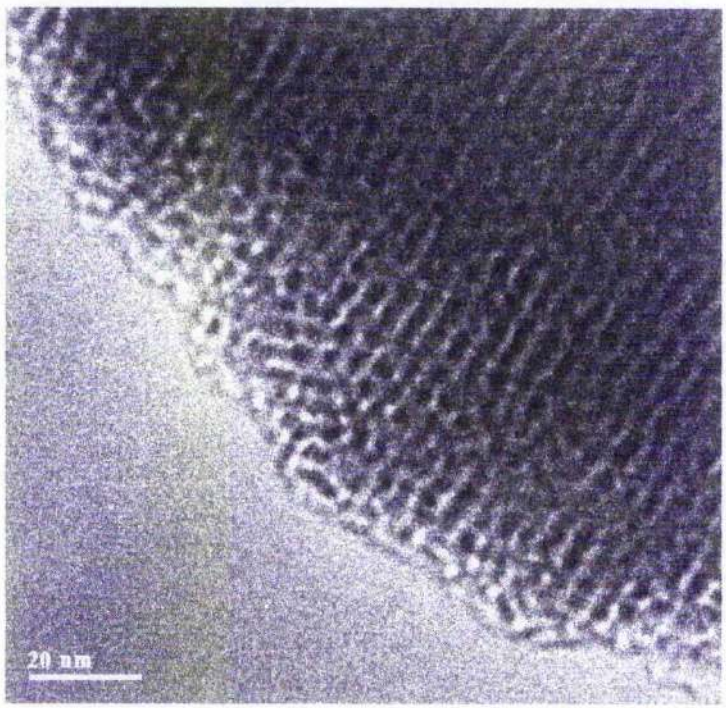

Fig. 4.15 overfocus image of porous material.

Fig. 4.15 is an image taken with over focus values on the 2011 TEM microscope. The image clearly shows visual artefacts, which are not in fact real. This leads to false information taken from an image that in all other respects appear valid.

4.3 Conclusions

The whole history of regular mesoporous materials is only approx ten years old. Many future investigations, with HRTEM at the forefront will be required. This chapter has shown that HRTEM can be used after the formation mechanism has taken place and can help in the improvement in the quality of these products, in the synthesis of new compounds and modification of these materials by chemical substitution or by the introduction of nanoparticles.

All these future programmes rely on the structural studies using HRTEM, as they involve scales ranging from nanometers to sub micrometers. As has been shown transmission electron microscopy is the most powerful technique in this field.

The mechanism of mesoporous sieve formation is still not fully understood. More detailed structural analysis may be carried out in future work on specimens synthesised at different conditions. Ordering of the silica framework along the *c*-axis of these materials was not detected, and whether ordered framework in pure or chemically substituted mesoporous materials can be prepared is problematic.

In the metal cluster-loaded mesoporous materials, the nature of the 3D ordering and exact locations of the metal nanoparticles are still awaiting detailed study. The nature of the ordering was not conclusive in this study. Further detailed study will have to be undertaken.

Silica forms on the surfactant templates and it can serve as a template too for preparing materials such as semi conducting or super conducting "molecular wires" *(Wu and Bein 1994)*. If these molecule-scale products contain heavy atoms, electron microscopy as this study has shown is one if not the best technique to monitor the formation of the products at different stages.

Thin film mesoporous materials are a developing interest of research, however preparation of the specimens for TEM studies without structural damage is difficult.

As has also been shown various metal clusters can be loaded into some mesoporous substances to develop new catalysts and HRTEM again was shown in this chapter to play an important role in the structural characterisation of these materials.

SECTION 2

SCANNING ELECTRON MICROSCOPY AND CHEMICAL ANALYSIS OF SOLIDS

Chapter 5 Introduction and aims

5.1 Scanning Electron Microscopy

What is S.E.M? The Scanning Electron Microscope (SEM) is a microscope that uses electrons rather than light to form an image. There are many advantages to using the SEM rather than a light microscope.

The SEM has a much greater depth of field, which allows a large amount of the sample to be in focus at one time. The SEM also produces images of high resolution, which means that closely spaced features can be examined at a high magnification *(Everhart and Thornley 1960)*. Preparation of the samples is relatively easy since most SEMs only require the sample to be conductive. The combination of higher magnification, larger depth of focus, greater resolution, and ease of sample observation makes the SEM one of the most heavily used instruments in solid state chemistry and materials science research today.

The electron source

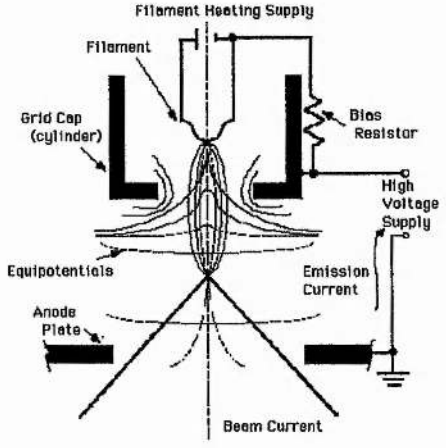

Fig. 5.1 Diagram showing source and passage of electrons.

The electron beam comes from a filament, made of various types of materials. The most common is the tungsten hairpin gun. This filament is a loop of tungsten, which functions as the cathode. A voltage is applied to the loop, causing it to heat up. The anode, which is positive with respect to the filament, forms powerful attractive forces for electrons. This causes electrons to accelerate toward the anode. Some accelerate right by the anode and on down the column, to the sample *(Fig. 5.1)*. Other examples of filaments are lanthanum hexaboride filaments and field emission guns *(Broers 1967)*.

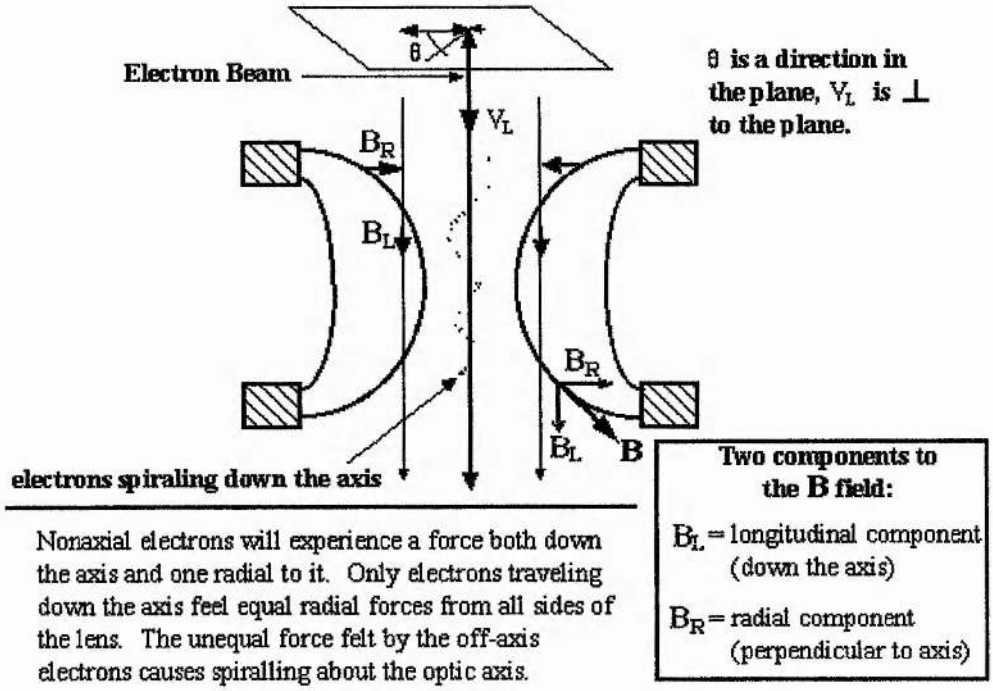

Fig. 5.2 Forces in a cylindrical magnetic lens.

Fig. 5.2 shows only electrons travelling down the axis feel equal radial force from all sides of the magnetic lens; these are the electrons that will form the image.

Beam's Path through the column

A beam of electrons is generated in the electron gun, located at the top of the column, which is pictured on the following page. This beam is attracted through the anode,

condensed by a condenser lens, and focused as a very fine point on the sample by the objective lens *(Fig. 5.3)*. The scan coils are energized (by varying the voltage produced by the scan generator) and create a magnetic field, which deflects the beam back and forth in a controlled pattern. The varying voltage is also applied to the coils around the neck of the cathode-ray tube (CRT), which produces a pattern of light deflected back and forth on the surface of the CRT. The pattern of deflection of the electron beam is the same as the pattern of deflection of the spot of light on the CRT.

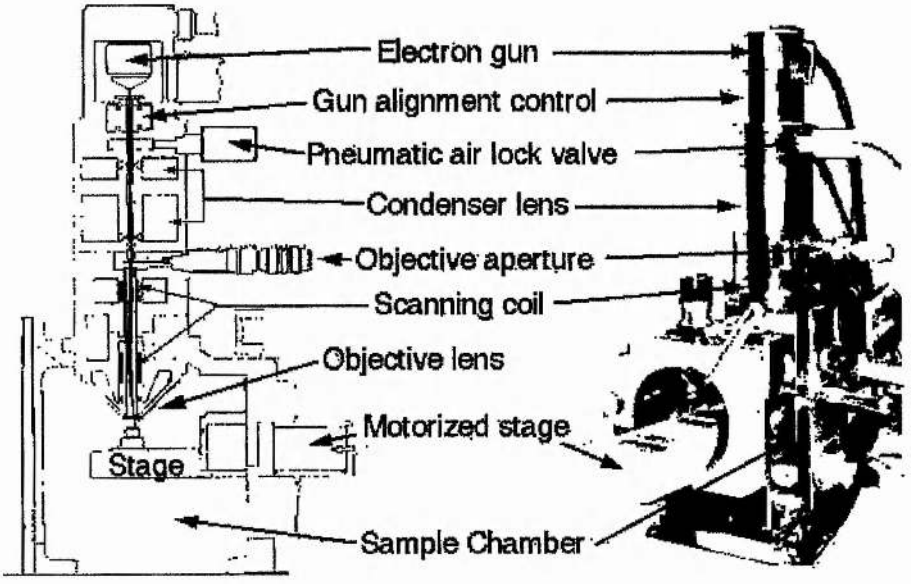

Fig. 5.3 Diagram of showing the mechanics of typical SEM.

The electron beam hits the sample, producing secondary electrons from the sample. These electrons are collected by a **secondary detector** or a **backscatter detector**, converted to a voltage, and amplified. This amplified voltage is applied to the grid of the CRT and causes the intensity of the spot of light to change. The image consists of thousands of spots of varying intensity on the face of a CRT that correspond to the topography of the sample.

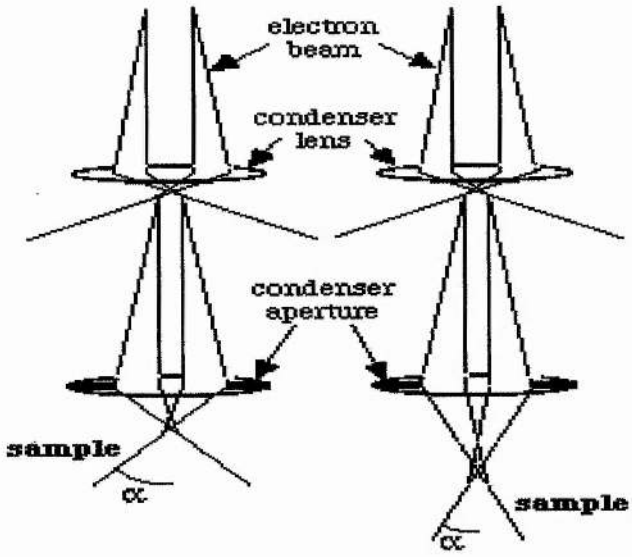

Fig. 5.4 SEM ray diagrams.

These schematics *(Fig. 5.4)* show the ray traces for two probe-forming lens-focusing conditions: small working distance (left) and large working distance (right). Both conditions have the same condenser lens strength and aperture size. However, as the sample is moved further from the lens, the following occurs:

- **the working distance *S* is increased**
- **the demagnification decreases**
- **the spot size increases**
- **the divergence angle *alpha* is decreased**

The decrease in demagnification is obtained when the lens current is decreased, which in turn increases the focal length *f* of the lens. The resolution of the specimen is decreased with an increased working distance, because the spot size is increased. Conversely, the depth of field is increased with an increased working distance, because the divergence angle is smaller.

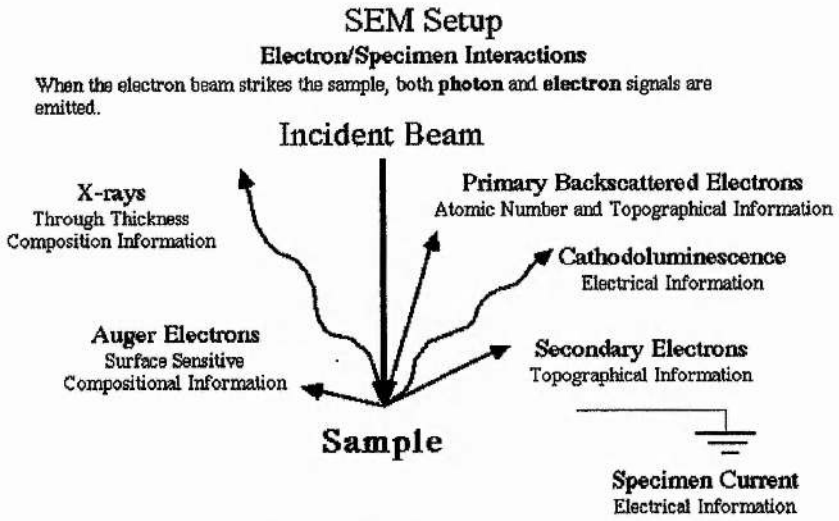

Fig. 5.5 Electron /specimen interactions.

While all these signals (*Fig. 5.5)* are present in the SEM, not all of them are detected and used for information. The signals most commonly used are the secondary electrons, the backscattered electrons and X-rays.

Using a vacuum

When a SEM is used, the column must always be at a vacuum. There are many reasons for this. If the sample is in a gas filled environment, an electron beam cannot be generated or maintained because of a high instability in the beam. Gases could react with the **electron source**, causing it to burn out, or cause electrons in the beam to ionise gas phase atoms, and cause random discharges which then in turn lead to instability in the beam. **The transmission of the beam** through the electron optic column would also be hindered by the presence of other molecules. Those other molecules, which could come from the sample or the microscope itself, could form compounds and condense on the sample. This would lower the contrast and obscure detail in the image. Another factor to be taken into consideration when a beam of electrons strikes a solid is the interaction volume.

Interaction volume

The interaction of the beam with the specimen is known as the **interaction volume**, and is the volume below the surface of the material, in which, primary electrons interact with electrons orbiting around atoms of the incident material. Secondary electrons are detected from a near-surface region of this volume, while backscattered electrons can be detected from this and much deeper parts of the specimen. Many electrons escaping from this region are absorbed into the material or not detected at all, as is the case with a small number of x-rays. The range of detected electrons and x-rays is said therefore to have come from the *sampling volume*. The sampling volume for x-rays is similar in size to the interaction volume because x-rays are less easily absorbed by the material *(Goodhew et al 2001)*. The diagram *Fig. 5.6* is a simple illustration of the interaction volume and particle detection zones.

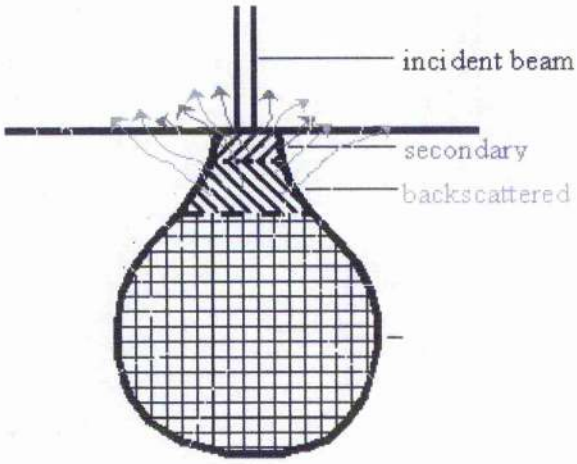

Fig. 5.6 Diagram showing the interaction volume and particle detection zones.

5.2 Energy dispersive X-Ray (EDX) analysis

Generation of X-Rays

The displacement of target material electrons by primary electrons triggers the release of an x-ray photon, which is characteristic of the atom (element) from which it was released. Atoms hold electrons in orbit around their nuclei as a result of electrical charge differences between them, the nucleus carrying a positive charge and the electrons carrying a negative charge. These charges exactly balance each other. The

arrangement of electrons around the nucleus of an atom is conventionally considered as a sequence of 'electron shells', with the innermost shell electrons possessing the lowest energy but with higher bonding energies, and the outermost electrons possessing the highest energies with lower binding energies. The shells are, also conventionally, labelled K, L, M, N, O, P, and Q from innermost to outermost. Because of the differing binding energy levels of the electrons around the nucleus, primary electrons of a higher potential energy (electron volts - eV) are required to displace K-shell electrons than are required to displace L-shell electrons, which is higher than that required for M-shell electrons etc. A simple diagram of the first three shells is illustrated below *(Fig. 5.7)*

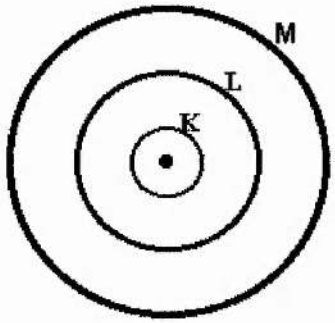

Fig. 5.7 Sequence of 'electron shells'.

Primary electrons bombarding the atom are able to 'knock' shell electrons out of their orbits, which can be replaced by electrons from shells further out, that are able to 'jump' into the inner shell vacancies. There are a number of reactions that occur as a result of this, but for the purposes of explaining the generation of x-rays, only the following points are considered. The knocking out of an inner shell electron causes the atom to take on an **excited**, high energy state until the missing electron is replaced and the atom **relaxes**. There is therefore a difference in energy states. This difference can be large, and if it is, the excess energy can be released in the form of an x-ray (it can also be released in the form of an Auger electron, but is not considered here), which carries this energy difference, and has a wavelength that is characteristic of the atomic species from which it came *(Echlin et al 1986)*. The following diagram *(Fig. 5.8)* is an illustration of this-

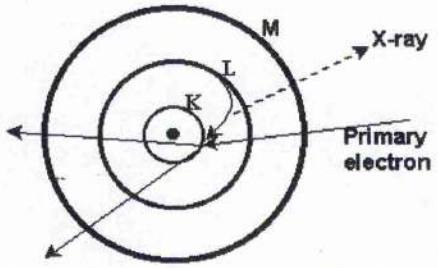

Fig. 5.8 Excess energy released in the form of an x-ray.

It should be noted that replacement of L and M shell (etc.) electrons can also be achieved by electrons jumping in from shells that are further out again, and can lead to a large number of generated x-rays of differing wavelengths. There are therefore a number of possible **lines** of x-rays available for analysis, but again this is not considered here.

Analysis of the X-rays

The most significant issue to note from this is that the x-rays generated from any particular element are characteristic of that element, and as such, can be used to identify which elements are actually present under the electron probe. This is achieved by constructing an index of x-rays collected from a particular spot on the specimen surface, which is known as a spectrum. An example spectrum for phosphorous with fluorine, (*Fig. 5.9*), the element peaks for analysis have been marked in red. Where two peaks are shown for the same element, the smaller peak corresponds to one of the other lines of electron replacement, such as an 'M' shell electron jumping into the 'K' shell. The y-axis is an arbitrary pixel count.

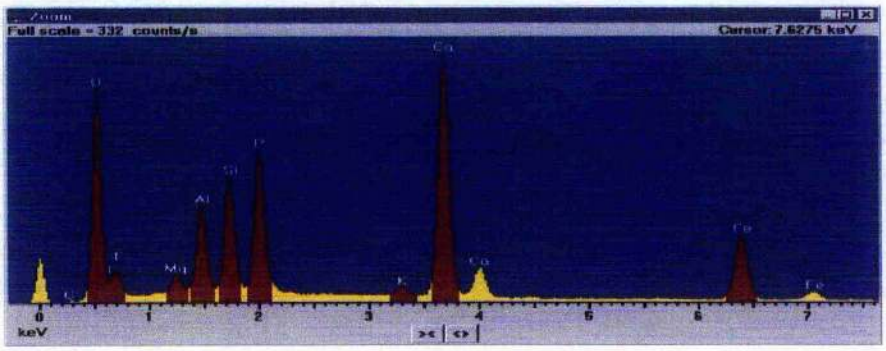

Fig. 5.9 Typical spectrum from the Oxford Instruments Isis-Link software.

The x-axis of the spectrum is the x-ray energy scale, along which x-rays collected from various elements are registered, and in which turn form a series of peaks along the x-axis where each peak corresponds to a particular element. With modern software it is possible to collect a series of spectrums for each point (pixel) analysed by the electron beam probe, as it is scanned across the surface of the specimen. If one spot only is analysed, quantification of the relative proportions of elements under that spot is possible, which is known as **point analysis**. If however a line of pixels is analysed, a line-traverse analysis can be performed which can highlight changing proportions of elements along that line. This is known as **line–scanning**. Finally each pixel in an image can be analysed which illustrates the distribution of a given element across the image. This is known as **dot-mapping** of the elements and can take up considerable time as the electron probe is required to dwell on each separate point for a pre determined period of time in order to collect enough data for analysis.

Efficient x-ray analysis usually requires a flat polished surface where there are few obstructions to x-rays leaving the surface of the specimen that may cause contamination to the signal. In this section it will be shown that in the real world this is not always possible and in some cases not practical. The software usually needs calibrated to a known standard before use.

5.3 Aims

By scanning an electron probe across a specimen, high resolution images of the morphology or topography of a specimen, with great depth of field, at very low or very high magnifications can be obtained. Compositional analysis of a material may also be obtained by monitoring secondary X-rays produced by the electron-specimen interaction.

Detailed maps of elemental distribution can be produced from multi-phase materials or complex, bioactive materials. Characterisation of fine particulate matter in terms of size, shape, and distribution as well as statistical analyses of these parameters, may be performed. However at present little is known as to the limitations of the present software used in modern chemical analysis of solids and of high resolution imaging using SEM.

In this section it will be shown by using different specimens the advantages and the disadvantages of such a system when the latest microanalysis software and SEM hardware is pushed to its limits.

Chapter 6 Experimental

6.1 Scanning Electron Microscope (SEM)

The Microscope

The microscope used for all the subsequent samples in this thesis is the Jeol-JSM 5600 scanning electron microscope (*Fig. 6.1)* this was operated at accelerating voltages from 5 to 30keV, Resolution: 3.5nm and magnification up to 300,000x. Specimen size: up to 125mm in diameter. In addition the microscope is capable of specimen tilt of –10 to +90° and specimen rotation of 360°. Working distance varies from 5 to 48mm.

Fig. 6.1 Jeol JSM 5600 scanning electron microscope.

The Jeol JSM-500/5600LV suite version 2.11 was installed on the computer, running operating system windows 95. All microscope commands are then undertaken using the computer. All images taken could be saved in the BMP or TIFF format and the computer is networked for remote access to images and other information.

6.2 Energy dispersive X-ray analysis system (EDS)

The system used on this project is the Oxford Instruments INCA Energy 200 Microanalysis System together with an external Scan Interface and Energy Integration software from Jeol. This package was installed on the JSM 5600 SEM, the External Scan Interface allowing the Oxford System to take control of the electron beam in the SEM, for mapping etc, and the integration software allows the Oxford system to acquire information regarding the operating parameters of the microscope, kV, working distance etc.

The Inca Energy 200 allows the user to carry out qualitative and quantitative analysis from an image from the microscope, acquire digital images and elemental maps and linescans. The standard detector used for the system is the Si (Li) 138 Ev, 10mm2 detector with SATW *(Fig. 6.2)* and the software includes three sections or navigators, **Analyzer, Point ID** *(Fig. 6.3)* and **Mapping**.

Fig. 6.2 Standard Si detector attachment for the SEM 5600.

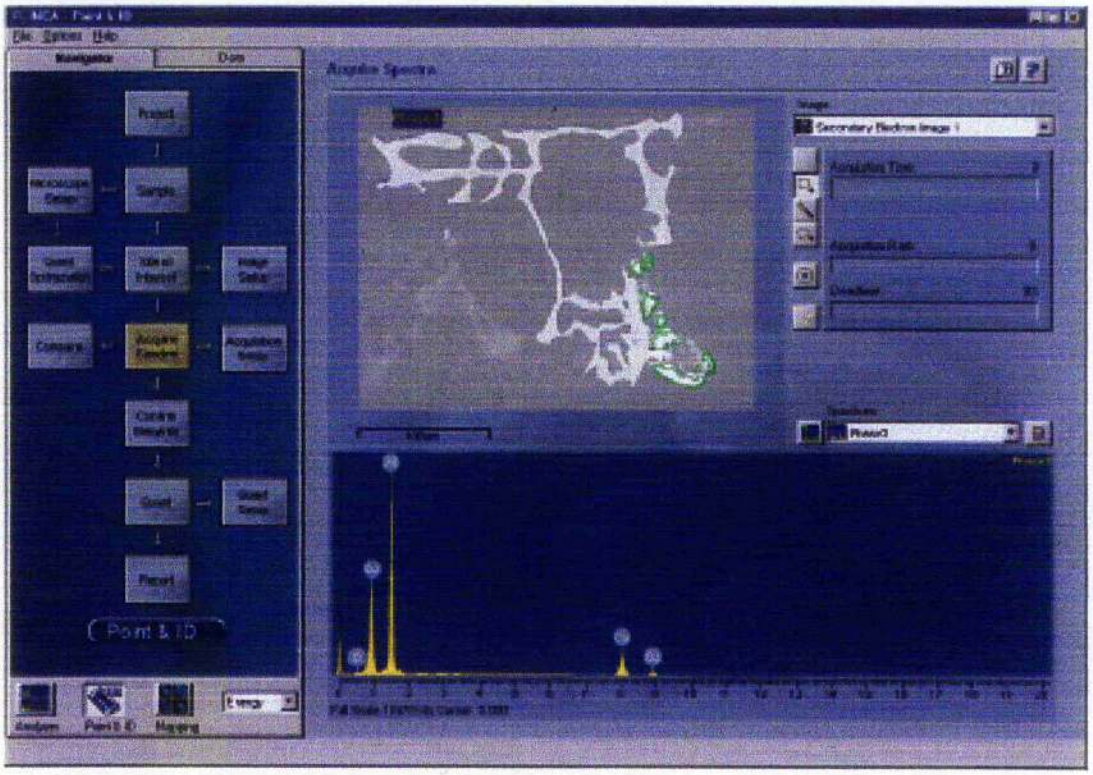

Fig. 6.3 A typical window from INCA Energy 2000.

Once the initial site of interest is located on the scanning electron microscope, all the subsequent x-ray analysis takes place on one monitor with one interface. Suitable areas for analysis are not always obvious on the electron image. **Cameo** images can compliment the electron image and often point the way to the analysis area much more clearly than the electron image alone. Point ID allows the operator to use the electron, x-ray or the cameo image as the reference to locate analysis points. This provides an accurate record of the precise analysis points.

Chapter 7 Results and discussion

7.1 NH_4Cl sample (Determination of optimal voltage for light elemental EDS analysis)

For the majority of samples undergoing EDS chemical analysis in SEM the optimal accelerating voltage is the maximum for the microscope, that is to say 30kV. Thus more X-rays generated and therefore greater acquisition rate, stronger peaks. However this is not the case with the light elements. It has long been assumed that EDS chemical analysis using SEM for hydrogen was impossible and that at best for nitrogen useless. However for N there may be a way to optimise the conditions of the microscope so as to make the results for this light element relevant to the whole project.

A sample of NH_4Cl was analysed under standard optimal conditions for EDS:

Working distance 20mm

Condenser Aperture 3

Spot Size 30-50

Accelerating voltage 30kV

On Inca, **Process time** of 5 seconds, **Acquisition rate** of between 2 and 5 Kcps and **Dead time** of < 30% (that is the time that the processor is not doing anything)

A spectrum was acquired using **Analyzer** *(Fig. 7.1)*

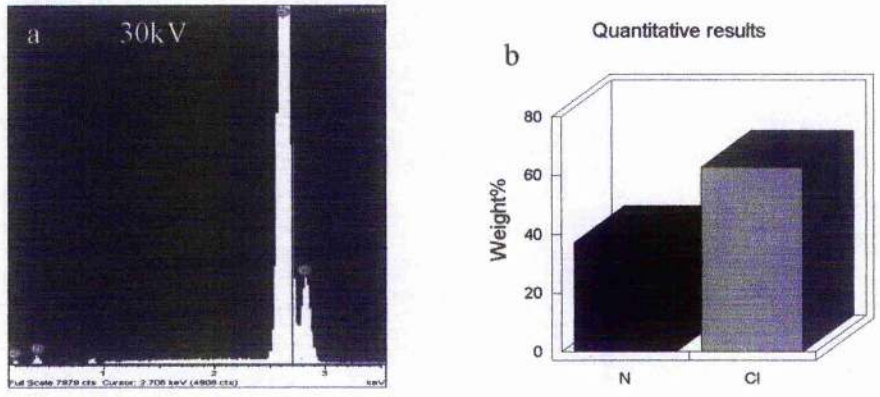

Fig. 7.1(a) Spectrum for NH_4Cl showing very strong peaks for Cl and one unexpected very weak peak for N, (b) Bar chart showing quantitative results.

Pro Accelerating voltage **30kV**
No peaks omitted
Processing option: All elements analyzed (Normalised)
Number of iterations = 3

Standard:
N Not defined 1-Jun-1999 12:00 AM
Cl KCl 1-Jun-1999 12:00 AM

Element	App Conc.	Intensity Corrn.	Weight%	Weight% Sigma	Atomic%
N K	5.57	0.0674	37.23	1.36	60.02
Cl K	130.1	0.9338	62.77	1.36	39.98
Totals			100.00		

Even allowing for the absorption problem, which confront peaks at the low energy range of the spectrum, the peak size for N is very much lower than would be expected this is due to the interaction of the light atoms with electrons, the interaction of heavy atoms and e^- is very different. The hydrogen in this sample as in all other samples cannot be analysed by EDS and there is no peak in the spectrum. Given all the problems with the spectra the quantitative results were nearer to the expected in the atomic %, approx 60%N to 40% Cl although vastly different in the Weight%. It would appear that if we can raise the intensity of the N peak then the results should approach a 1:1 ratio at least for the Weight intensity. By lowering the accelerating voltage from 30kV downwards the elemental peak at the low energy level (ie: N) of the spectrum should be raised and that at the higher energy range (ie: Cl) lowered. The same conditions as above were used for 20Kv *(Fig. 7.2)* and 10kv (*Fig. 7.3)* a spectrum was collected in Analyzer for both.

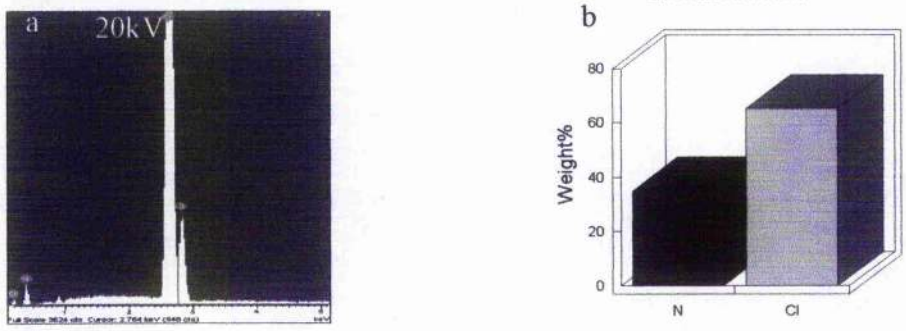

Fig. 7.2(a) Spectrum for NH_4Cl collected at 20kV, (b) Bar chart showing quantitative results.

Pro Accelerating voltage **20kV**
No peaks omitted
processing option: All elements analyzed (Normalised)
Number of iterations = 3

Standard:
N Not defined 1-Jun-1999 12:00 AM
Cl KCl 1-Jun-1999 12:00 AM

Element	App Conc.	Intensity Corrn.	Weight%	Weight % Sigma	Atomic%
N K	3.88	0.0796	34.86	1.24	57.53
Cl K	85.05	0.9343	65.14	1.24	42.47
Totals			100.00		

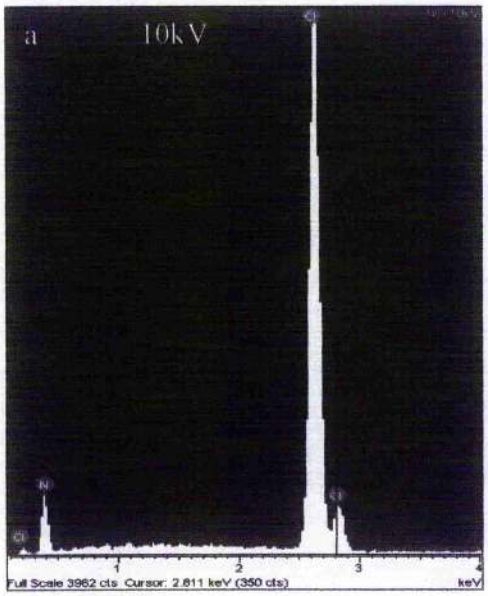

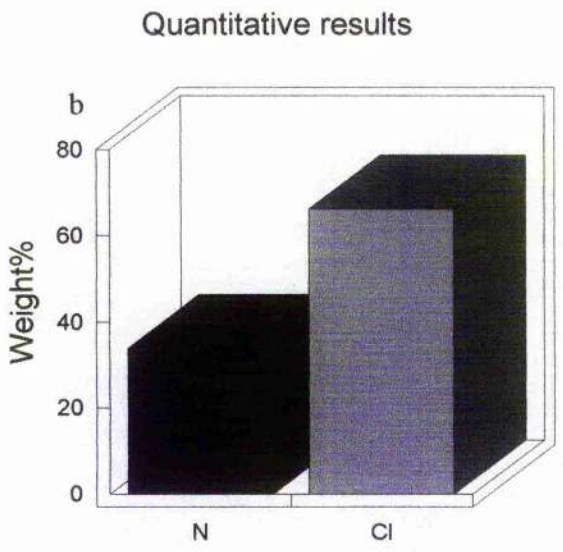

Fig. 7.3(a) Spectrum for NH_4Cl collected at 10kV, (b) Bar chart showing quantitative results.

The quantitative results for elemental % shown above are shown in both weight % and atomic %, the bar chart shown in *Fig7.3b* is shown in weight % only.

Accelerating voltage **10kV**
No peaks omitted

Processing option: All elements analysed (Normalised)
Number of iterations = 3

Standard:
N Not defined 1-Jun-1999 12:00 AM
Cl KCl 1-Jun-1999 12:00 AM

Element	App Conc.	Intensity Corrn.	Weight%	Weight% Sigma	Atomic%
N K	1.35	0.1879	33.83	1.01	56.41
Cl K	13.01	0.9260	66.17	1.01	43.59
Totals			100.00		

From the above results it appears that the decrease in voltage improves the percentage ratio for Atomic % and also for the Weight %.

The voltage was decreased twice more once to 5 kV *(Fig. 7.4)* and then to 3kV *(Fig. 7.5)*

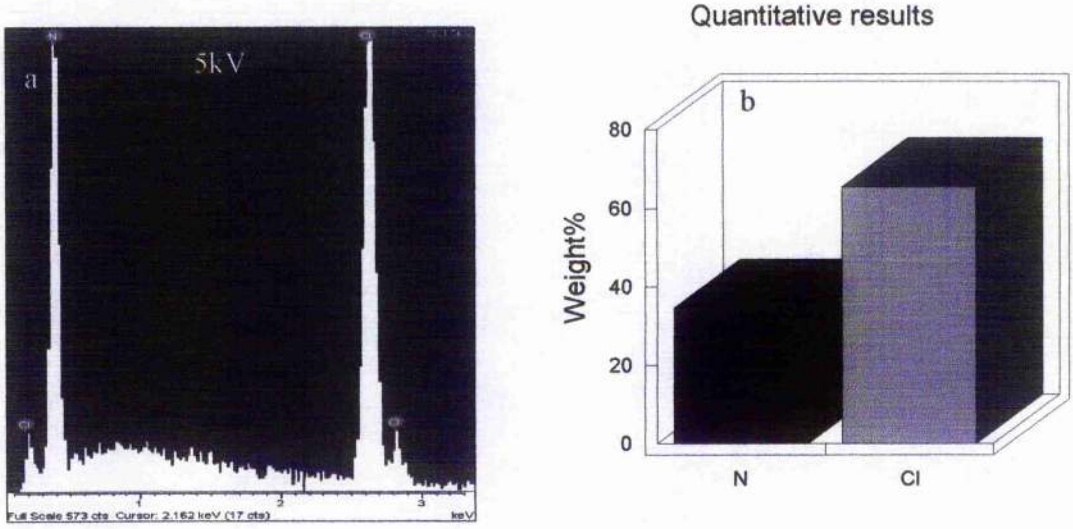

Fig. 7.4(a) Spectrum for NH_4Cl collected at 5kV, (b) Bar chart showing quantitative results.

Accelerating voltage **5kV**
No peaks omitted

Processing option: All elements analysed (Normalised)
Number of iterations = 3

Standard:
N Not defined 1-Jun-1999 12:00 AM
Cl KCl 1-Jun-1999 12:00 AM

Element	App Conc.	Intensity Corrn.	Weight%	Weight% Sigma	Atomic%
N K	222.29	0.4882	34.55	1.08	57.20
Cl K	783.75	0.9087	65.45	1.08	42.80
Totals			100.00		

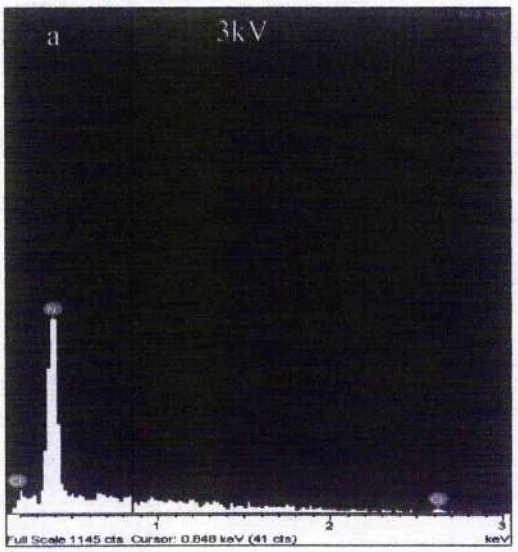

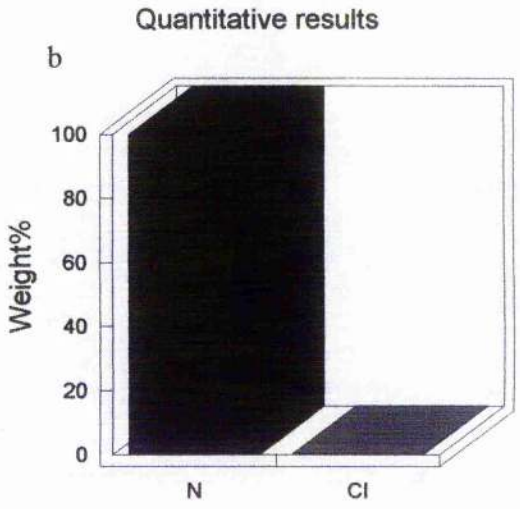

Fig. 7.5(a) Spectrum for NH_4Cl collected at 3kV, (b) Bar chart showing quantitative results.

Accelerating voltage **3kV**
No peaks omitted

Processing option: All elements analysed (Normalised)
Number of iterations = 2

Standard:
N Not defined 1-Jun-1999 12:00 AM
Cl KCl 1-Jun-1999 12:00 AM

Element	App Conc.	Intensity Corrn.	Weight%	Weight% Sigma	Atomic%
N K	837.04	0.9991	99.82	0.06	99.93
Cl K	1.10	0.7389	0.18	0.06	0.07
Totals			100.00		

At 5kV it appears that the Atomic% is beginning to drift away from the1:1 ratio again, although the Weight % has recovered slightly and visually the peak intensity for the first time look almost equal. The 3kV proves that at this voltage there is no value in the data either quantitatively or visually, the Cl peak has almost disappeared and for both Atomic and Weight % the data is biased to the benefit of the light element. The actual intensities of the peaks have to be taken into consideration at all voltages as can be seen in the next two figures (*Fig's. 7.6, 7.7).*

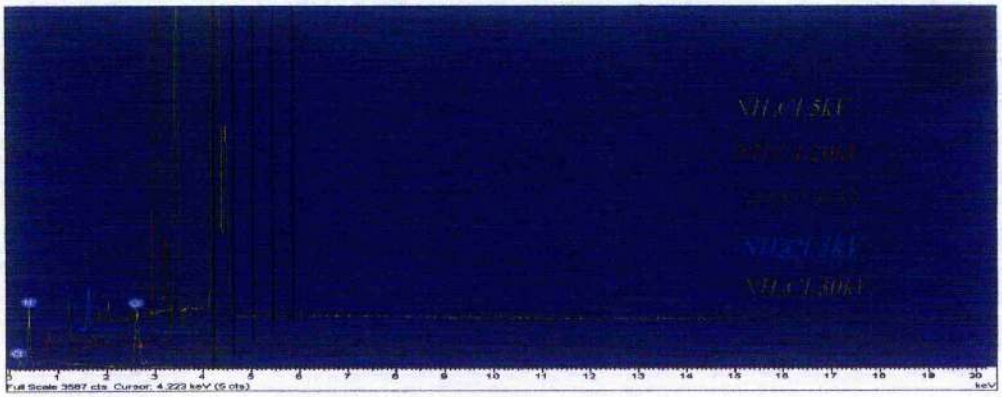

Fig. 7.6 Relative intensities of voltages when stacked.

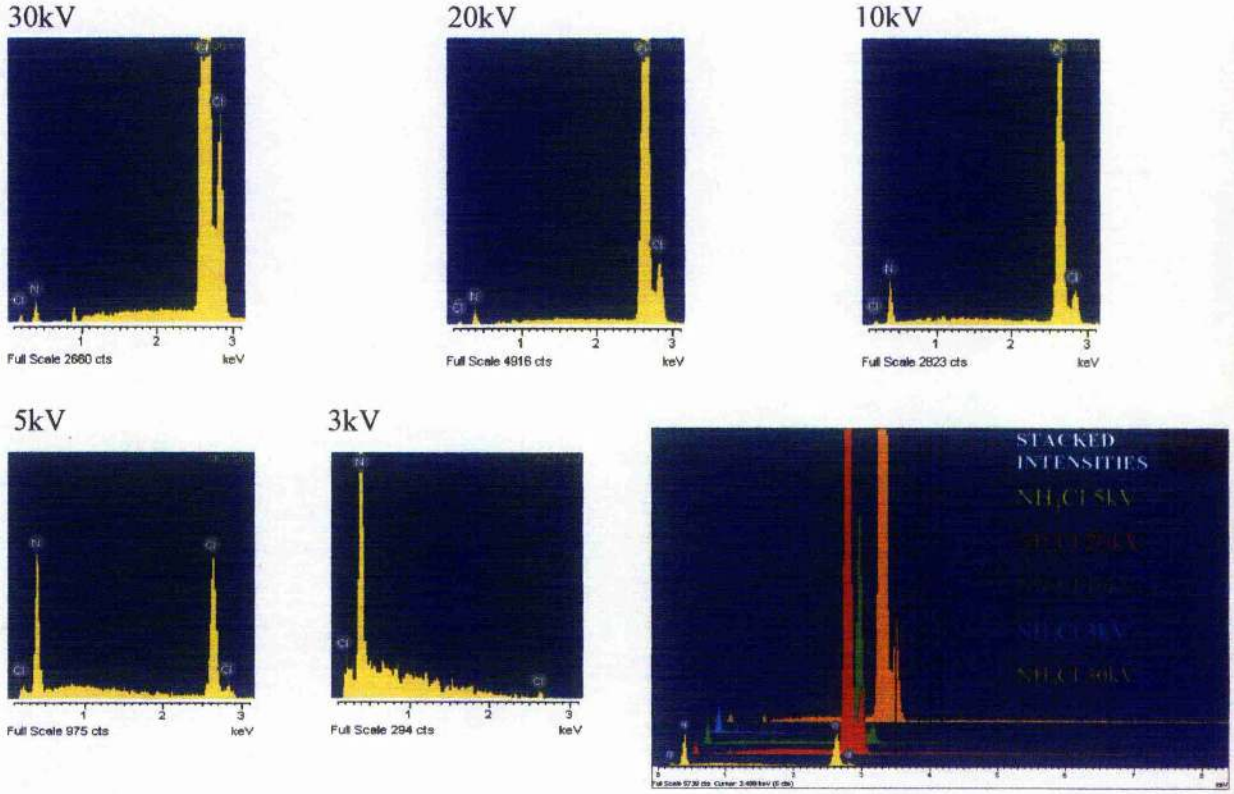

Fig. 7.7 All spectra with decreasing voltages including the intensities of elements at all voltages when stacked together.

It would appear that EDS chemical analysis of light elements by SEM is problematic. However the atomic % and the weight % of a light element such as N can be improved to a certain degree by decreasing the accelerating voltage. The weight % appears to change very little with voltage decrease as to be almost insignificant as can be seen from the results shown previously. The Atomic% can be improved fairly significantly with a decrease in voltage to about 5kV. In the 5kV spectrum it can be seen that the intensities of the N and the main Cl peak are equal, however this is relative, the intensities for both peaks are very weak this is shown in *Fig. 7.6* which shows all intensities of peaks at all voltages studied. The peaks at 30, 20, 10kV are relatively similar where as the low voltage of 5kV has improved the N peak slightly at great expense of the main Cl peaks intensity. The 3kV spectrum shows also severe loss of information both visually and quantitatively from the higher energy range of the spectrum. The light element peak has

greater intensity at the expense of the Cl peak, and in fact the third Cl peak has disappeared. This has to be taken into consideration.

From the results obtained it would appear that the best voltage for a sample with N, suspected or known is 10 kV, visual information may not be as helpful as one would like, however the peak intensity and Atomic % are probably more realistic than those obtained for the 5kV conditions.

In conclusion if a sample with a light element such as nitrogen but not hydrogen is to be analysed using EDS under SEM conditions, 10-15 kV accelerating voltage should be used for acceptable light element results and to give proper and real results for elements at the higher energy range in the spectrum.

In this chapter of the project it has been shown that the optimal conditions usually set for SEM EDS i.e.: Accelerating voltage 30kV, working distance 20mm and spot size 30-50 can be altered with consideration to the sample being analysed. In the remainder of this section It will be shown using samples of differing compositions and structures the optimal conditions needed for SEM imaging and chemical analysis.

7.2 SEM Imaging and EDS chemical analysis of a contaminated paper sample.

7.2a Introduction

SEM imaging and Chemical analysis of solids may come in many varied forms, the majority of samples received are in powder form but some non powder samples such as paper, rubber and ceramics are regularly received for analysis. Each of these samples has to be treated as individual cases with different criteria for optimal imaging and analysis.

7.2b Experimental

Two small strips (2-3mm) were cut from areas of the paper, **normal** non-contaminated and **contaminated** paper. Each of the samples were mounted on brass stubs with double sided carbon paper to enhance conduction and inserted into the Jeol JSM 5600 SEM. Digital images of the three areas were then acquired followed by EDS chemical analysis

7.2c Results

Normal Paper

At high voltages the paper reacted detrimentally with the beam, this made imaging difficult but not impossible if a faster scan such as scan mode 2 on the microscope software was used. At a lower voltage satisfactory images could be obtained with a low spot size <25 and slower scan such as scan 4. If an area was reacting so badly with the beam that acquiring a respectable image was impossible with scan 3 or 4, then the image was successfully obtained by using scan 2 and freezing the image. However where possible an image was taken at 30kV, because in general the resolution is much better and also EDS chemical analysis is usually undertaken at 30kV voltage for best results. The following images *(Fig's. 7.8a,b)* show low magnification images of normal paper taken at 30kV under optimal working conditions:

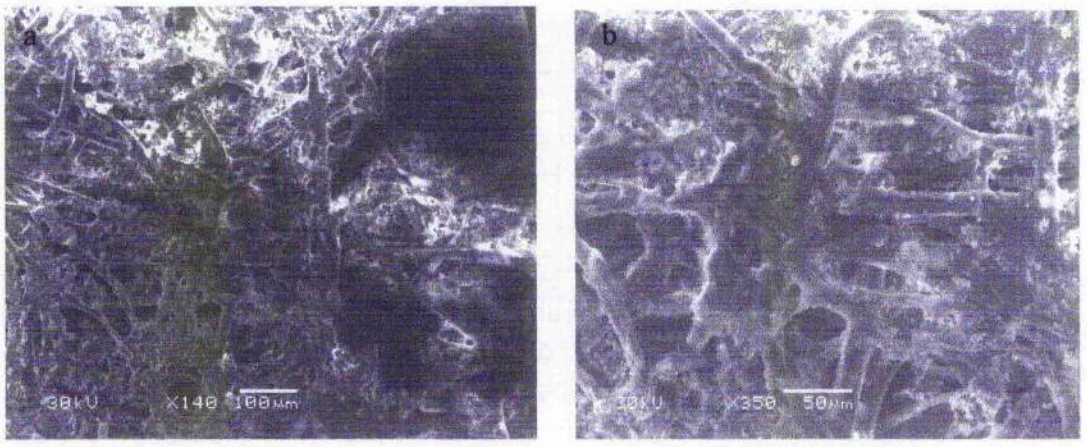

Fig's. 7.8 (a) A low magnification image x140 showing the fibrous nature of the sample, (b) a similar area at a higher magnification, x350.

The images *Fig's. 7.8a, b* show the expected fibrous morphology of normal paper, no defects are present and the appearance is that of well-structured paper. A contaminant need not be visually evident, the presence or otherwise of a foreign body can only be ruled out or confirmed using EDS.

Point ID analysis

Three points taken from different areas on an image were chosen for point ID analysis and the spectra then acquired (*Fig. 7.9a-c)*

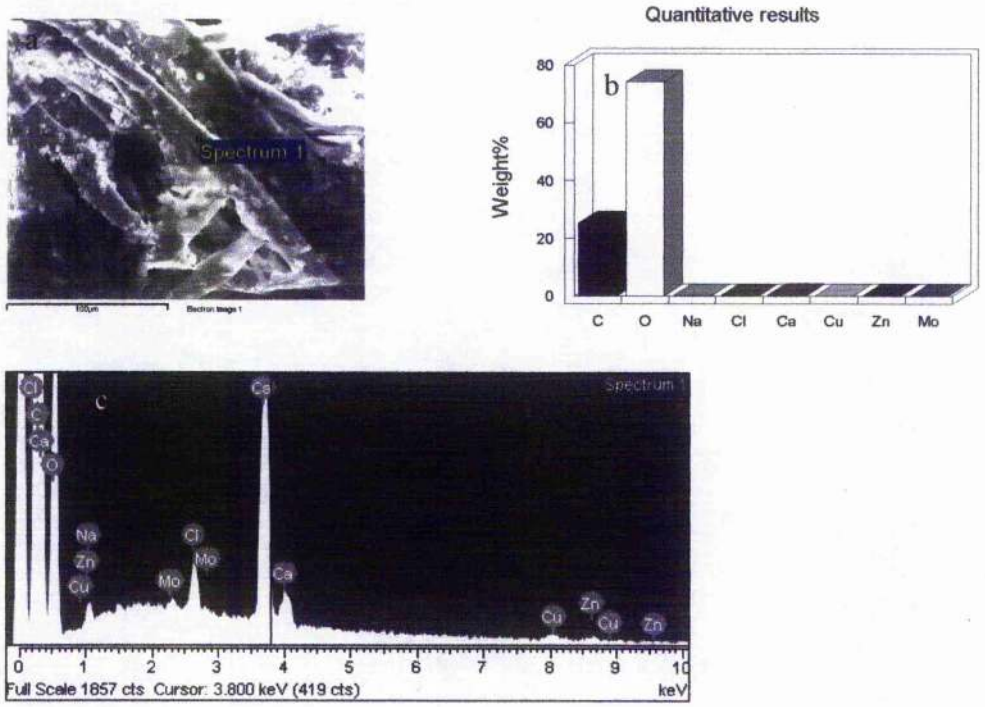

Fig. 7.9 (a) the original image with the point of which the spectra is acquired shown, (b) the quantitative results showing all elements by weight % as a bar chart, (c) is the original spectrum after a period of acquisition.

The results show elemental composition expected of paper, some residual element show from the pulp paper mix. These may arise from the water used in this process. No strong contaminant is evident. Two further point ID spectra were taken from different areas on this image (*Fig's. 7.10, 7. 11).*

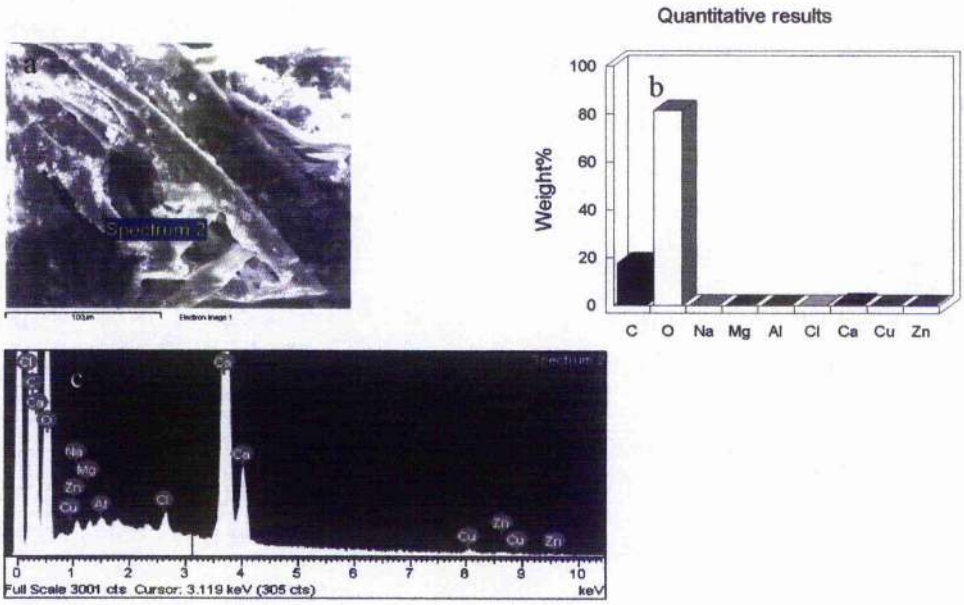

Fig's. 7.10 (a) the original image of normal paper with the point of which the spectra is acquired shown, (b) the quantitative results showing all elements by weight % as a bar chart, (c) the original spectrum after a period of acquisition.

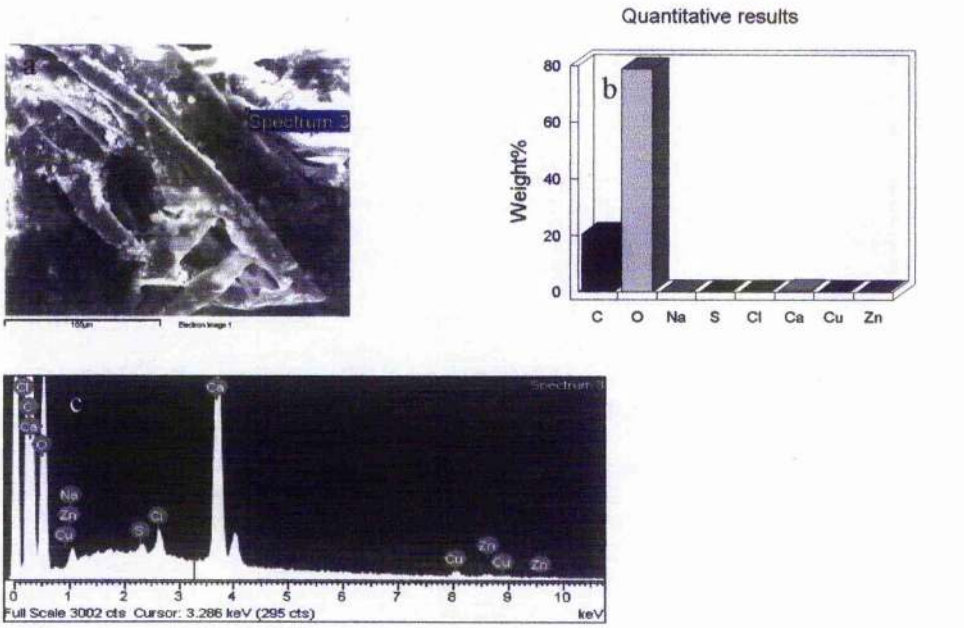

Fig's. 7.11 (a) the original image of normal paper with the point of which the spectra is acquired shown, (b) the quantitative results showing all elements by weight % as a bar chart, (c) the original spectrum after a period of acquisition.

From the above results it can be ascertained that the three areas are of similar elemental composition, this is clearly seen when the three spectra are superimposed on one another (*Fig. 7.12)*.

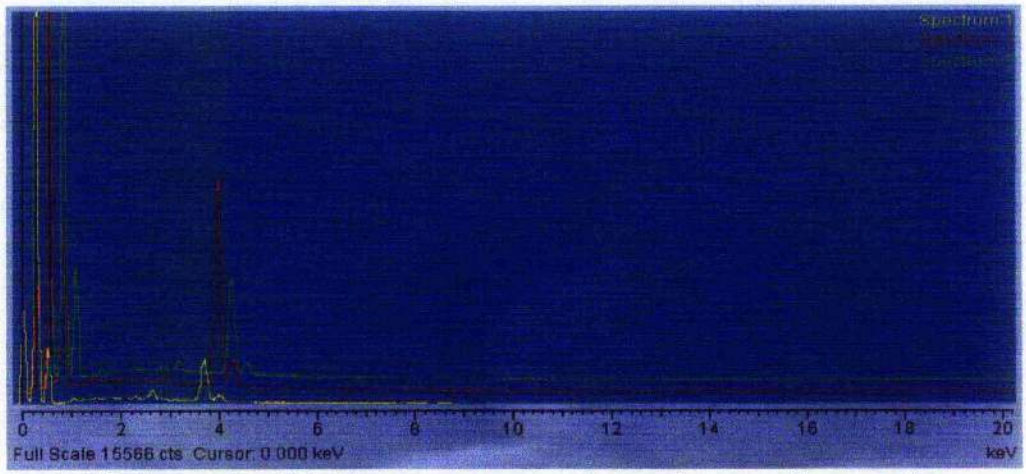

Fig. 7.12 The results of the three spectra superimposed on top of one another.

Fig. 7.12 shows that the spectra are similar although the intensities may differ; this could be due to the thickness difference of the three areas or the acquisition rate of X-rays, which tend to be different from area to area.

To determine the locality of specific elements, **mapping** of an area may be used. This is particularly useful when a powder compound is suspected of being homogenous, however a peak of another element is present. Mapping can show if such an element is local and not present throughout a sample. In this case it is used as corroborating proof that no "foreign" element is present in the paper sample (*Fig. 7.13)*. Mapping on its own may not give enough information about or indeed its exact location a particular elements quantity within a given sample or indeed its exact location, however along with the point analysis technique it is a powerful analysis technique. The map shown in *Fig. 7.13* was originally taken over a period of approximately 30 minutes at 30kV, spot size 30-40 and working distance approximately 20mm.

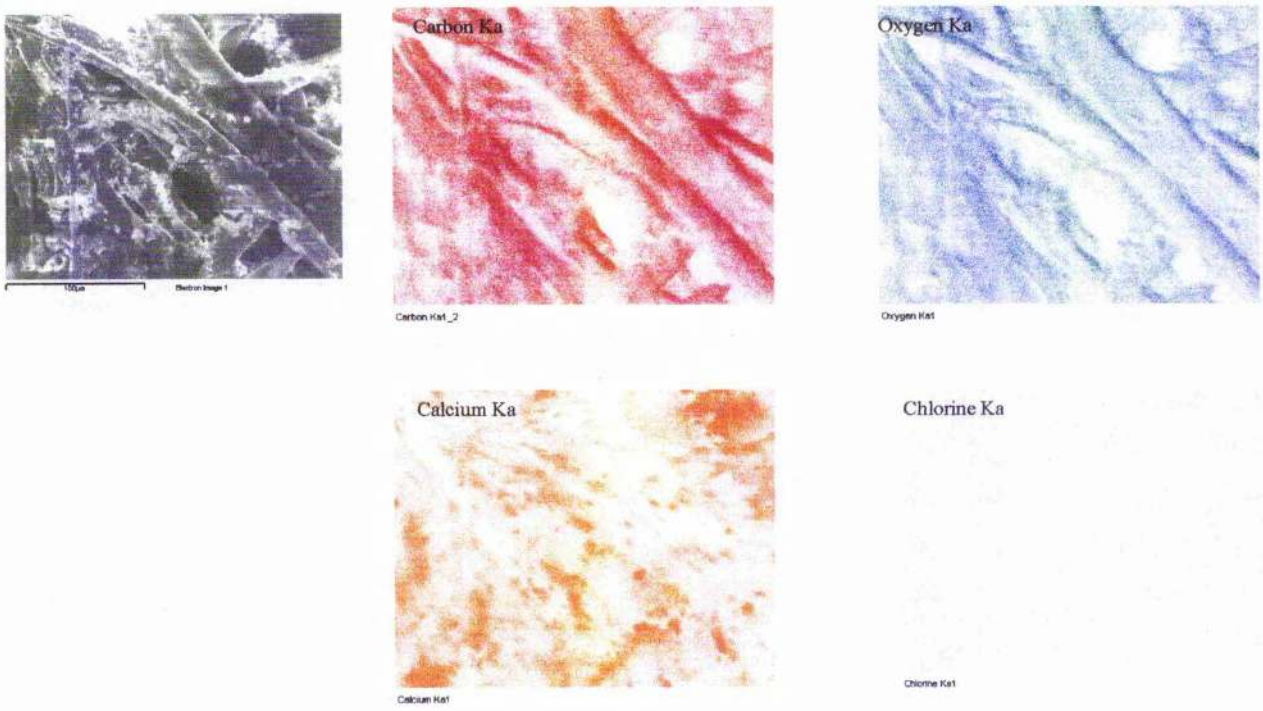

Fig. 7.13 Mapping of individual elements in a specific area of the sample at 30kV and an acquisition time of 30 minutes.

The mapping of this particular area of the sample shows that the paper fibres are homogenous for oxygen and carbon, this would be expected. The sample also has a high calcium content, which is consistent with the pulp process, with some local "hot spots" with very high calcium content. There is also a background trace of chlorine although it is too small to be of any interest. The results in all show an uncontaminated normal sample of paper.

Contaminated Paper

A strip of paper <3mm was cut from an area of the paper sample where a contaminant was suspected, images were then taken at 5-30kV accelerating voltage (*Fig. 7.14).*

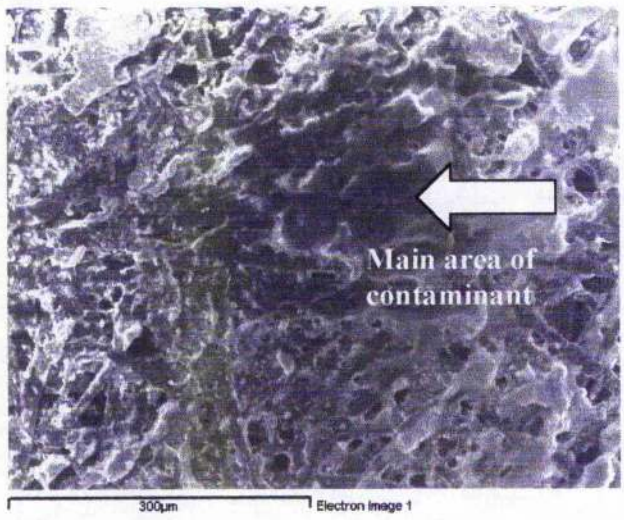

Fig. 7.14 Image showing the main area of contaminant.

This image shows very clearly the differing morphology of the contaminated paper to that of the normal. The affected area can be clearly seen in the central right position of the image. The fibres of the normal paper have been replaced by a smooth ruptured mass, of which its appearance does not resemble that of paper fibre. Point ID was then undertaken on this area *(Fig. 7.15, 16).*

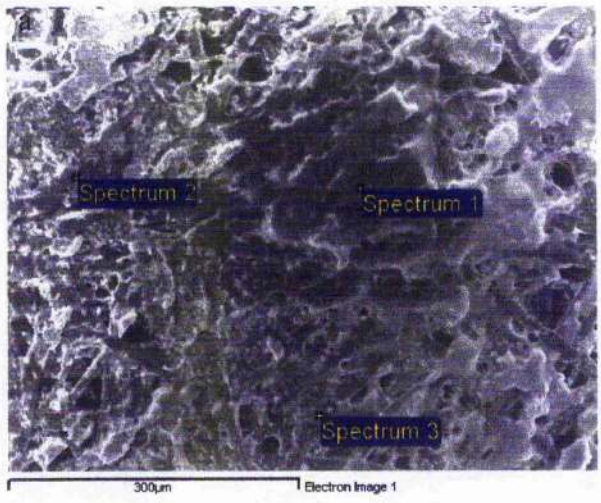

Fig. 7.15(a) Areas of interest for Point ID.

b

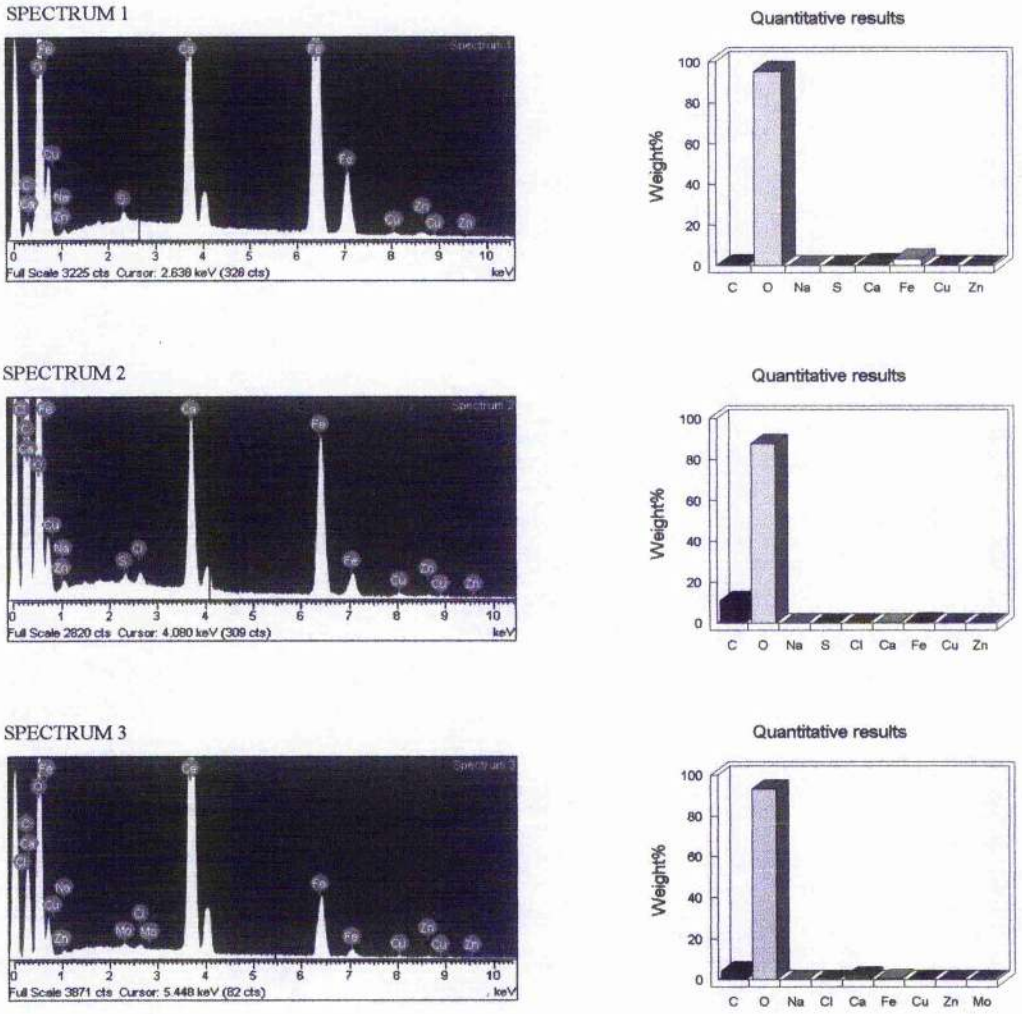

Fig. 7.15 Point ID undertaken on three points on the sample (a) and the resulting spectra and quantitative bar chart shown in (b).

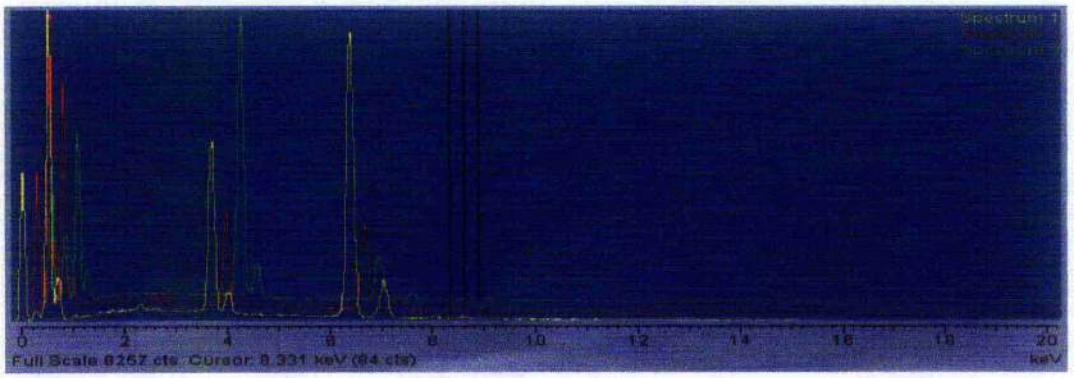

Fig. 7.16 Spectra comparison of the three points analysed.

From the results *(Fig. 7.15,16)* it is almost conclusive that the contaminant is iron based, what cannot be ascertained from these results is, if the iron is localised, therefore showing strong peaks in the point ID spectra over specific points, or if it is homogenous and spread evenly over the whole area. Mapping *(Fig. 7.17)* of the same area is the next logical step to confirm elemental locality.

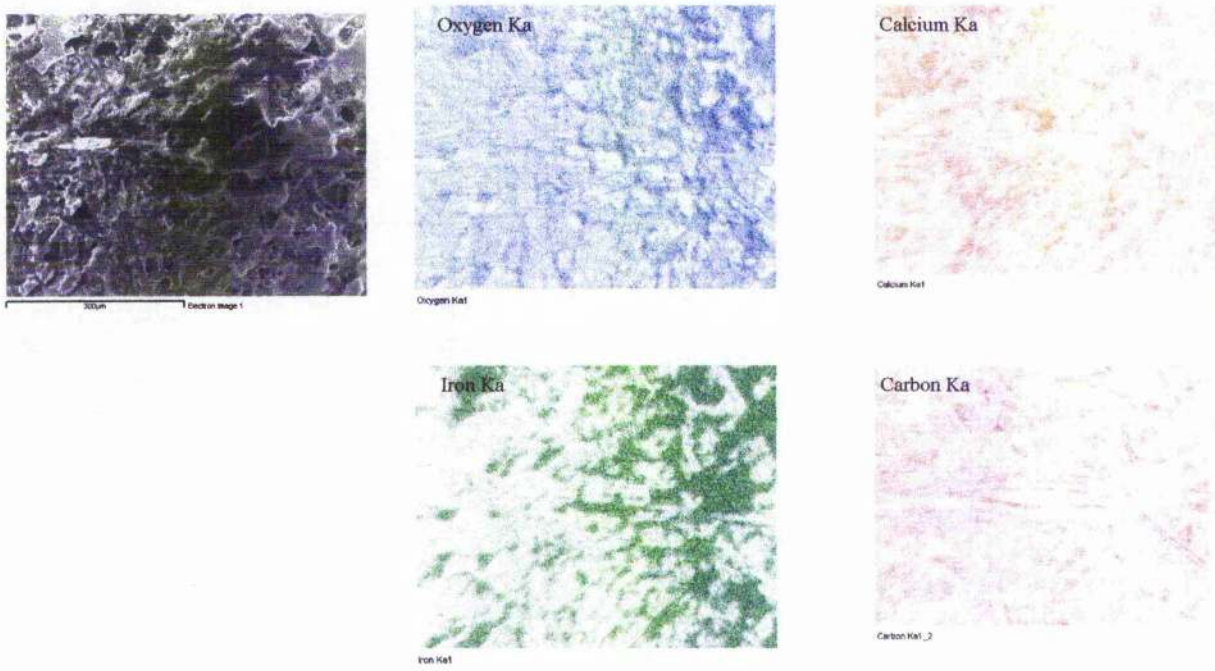

Fig. 7.17 Mapping of elements from the area of contamination.

This proves conclusively that the contaminated area of the paper sample is of iron in content and also widespread evenly through the area, although stronger to the right of the image. There is a strong signal for oxygen, carbon and calcium (normal paper) in the areas devoid of, or having little iron present, towards the left of the image. It has to be concluded from this result that the area which is predominately on the left hand side of this image and which is devoid of any iron is normal composition paper.

7.3 Quant calibration of the INCA system before EDS analysis

Ambient temperature changes will alter the gain of the system and this will affect where peaks appear in the spectrum. The microscope beam current also may vary with time and the peak positions may not be exact. The high resolution of the system is needed to precisely identify individual peak components in the spectrum. If the peaks overlap, the relative sizes of individual peaks can only be calculated accurately if the width and position of each peak is accurately known by measuring the position of one known peak, the system can be optimised to determine the position of all other peaks. If we want to measure the absolute concentrations, we need to make a comparison of the intensity of a peak with that from a known material. If we measure a known material, we can then make accurate intensity measurements of the unknowns, provided the beam current doesn't alter after the optimisation.

The necessary information was automatically measured by performing a Quant Optimization, which required the acquisition of a high quality spectrum from which details of a beam current and spectrometer gain was measured. Quant Optimization requires acquisition of a high quality spectrum from a suitable element from which details of the beam current and spectrometer gain are calculated and stored. If accurate qualitative identification of peaks and no substantial overlaps in the spectrum is sought then gain optimization should be carried out. If it is more than relative concentrations that is needed and you cannot work with the normalized total, the selection of beam current correction standard becomes much more important.

At least one Quant Optimization was performed every two hours for the samples in this section of the thesis. The spectrum was then processed by selecting Normalization and either "All elements" or "Element by Stoichiometry". If more than two hours had elapsed since the last Quant Optimization was carried out the "Last Quant Optimization performed more than two hours ago" warning was shown.

The electronics used in INCA are carefully designed to provide good temperature stability. Since a change of 10° C produces only a 1eV shift in the peak position, most routine analysis can be performed without re-optimizing peak position. However, if you need the software to resolve very closely overlapped peaks, a Quant Optimization should be performed and re optimized if the ambient temperature changes by a few degrees. With a

good laboratory temperature control you may not need to Quant Optimize for many hours. If you wish to calculate un-normalized totals, the frequency with which you perform the Quant Optimization will depend on the stability of the beam current. Repeated measurement of a known standard will indicate whether beam current is varying. The variation in analysis total was in direct proportion to the change in current since the last Quant Optimization. If there was a change in the spectrum range or type of detector since the last Quant Optimization was performed, a message box was displayed "The spectrum range or the detector type selected is different from the one used for the last Quant Optimization".

X –ray peaks involve multiple lines and accurate calibration requires a large peak with well-known line energies and intensities. Therefore, you should choose a pure element with k series lines that are strongly excited at the energy range you are using. Higher energy lines are less strongly excited but can give more accurate gain calibration provided the statistical precision is not compromised by poor excitation of the line. Accurate calibration can be achieved using the following pure elements Si, Ti, V, Cr, Mn, Fe, Co, Ni, Cu. Oxides or compounds should not be used because of the chemical effects on the line emissions. For example, if an accelerating voltage of 5 kV were used, then pure Si would be a suitable Optimization element. For 10kV pure Ti is a good choice. For 20 kV accelerating voltage, pure Co or Cu would be suitable for the Optimization element.

The system profiles were calibrated using Co as an optimization element. Pure Co resists oxidation and polishes well and is therefore the most suitable choice to monitor beam current when you want to obtain un-normalised or "absolute" estimates of composition. However, below 15kV, cobalt K is weakly excited and it is better to choose another pure element for monitoring. The system will make suitable corrections to allow the following pure elements to be used: Si, Ti, V, Cr, Mn, Fe, Co, Ni, Cu. If the optimisation standard is oxidised, contaminated or has a rough surface, then this will have a direct effect on the analysis totals.

If the element used for the Quant Optimization is not Co, satisfactory results may still be obtained, particularly if the alternative standard is a well polished pure element with the same conductive coating (if used) as the sample to be analysed. If you cannot obtain the ideal standard for optimisation, then the analysis total will not be reliable but satisfactory results can still be obtained by normalizing to a total of 100%. With normalization, you need not

worry about beam current fluctuations but care must be taken not to omit any major elements from the list because this will not be obvious in an analysis total, which is forced to 100%.

In the previous samples and all subsequent samples both Cu and Co standards were used for Quant Optimization (*Fig. 7.18).*

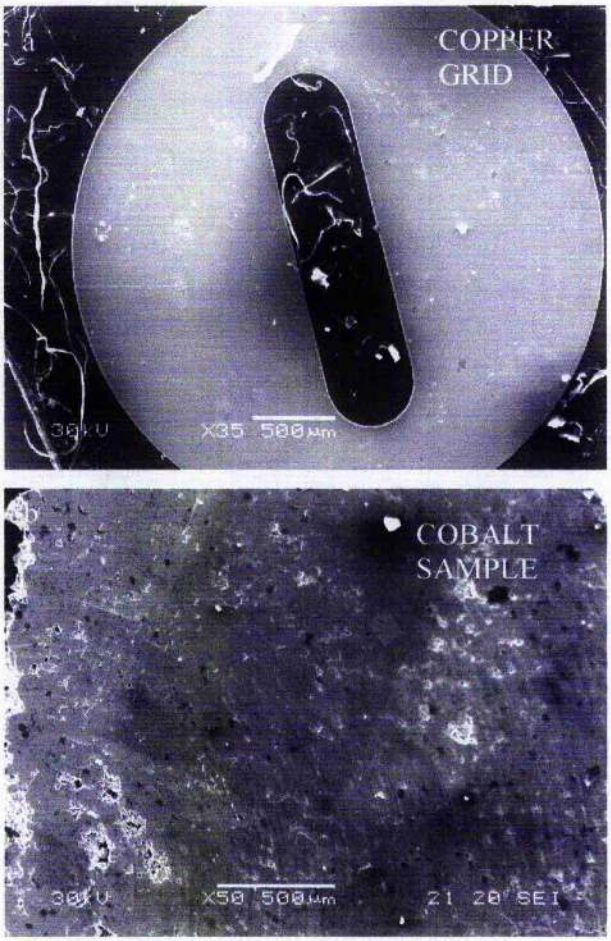

Fig. 7.18 (a) A low magnification image of a copper grid, used for Quant Optimization, (b) low magnification image of cobalt sample.

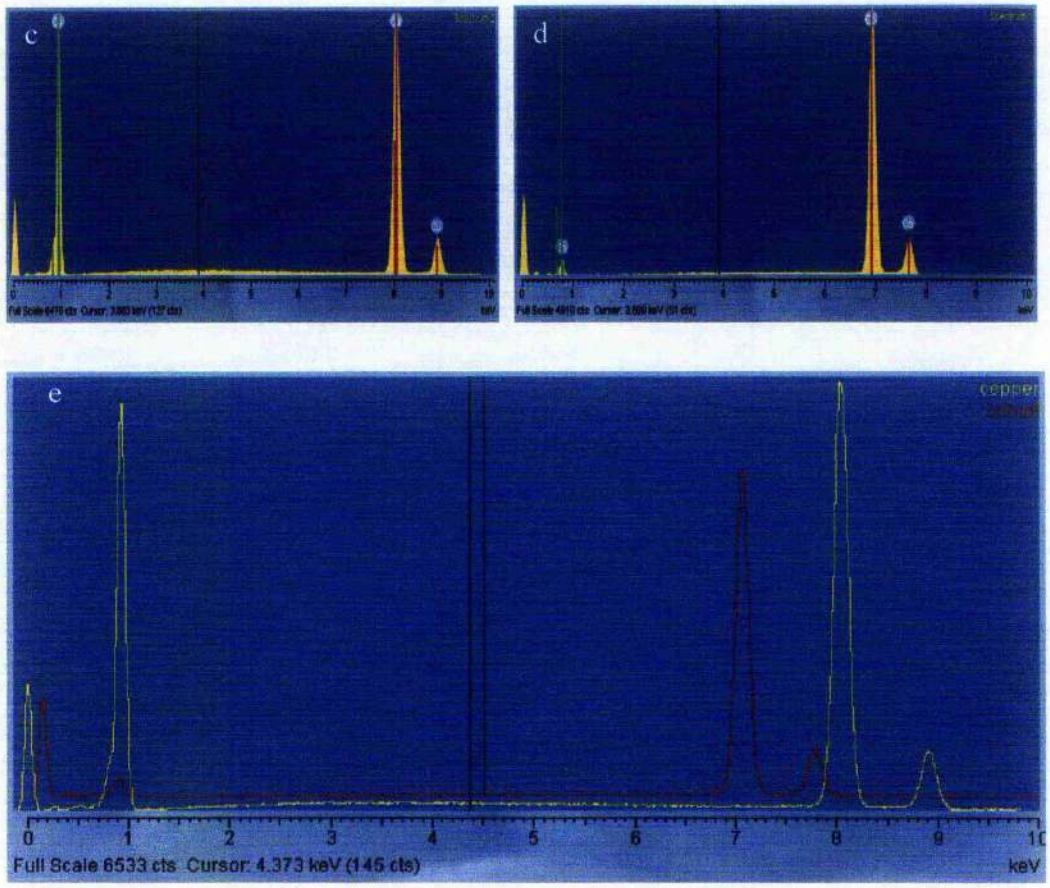

Fig. 7.18 (c) and (d) spectra acquired for Cu and Co respectively and (e) spectra for Cu and Co superimposed on one another.

Both of the two elements used for Quant Optimization have very strong intensity Kα peaks, for Co Kα 6.92 and Cu Kα 8.04 respectively therefore it follows that either Co or Cu could be used as the optimising standard for elements toward the higher energy range of the spectrum. However in the lower energy range, Co has a much weaker intensity Lα peak than that of Cu, CoLα 0.77 and CuLα 0.9 respectively, once again it follows that for an element at the lower energy level of the spectrum it would be more suitable to use Cu as the optimising standard for more accurate results.

7.4 Identification of a contaminate within a solid solution sample of $BaBiO_3$

A solid solution of $BaBiO_3$ was synthesised using the protocol described in section one. EDS on the TEM ISIS microanalysis system showed a probable contaminate within the nominal expected ratio of Ba:Bi 1:1. It was decided to analyse the suspected contaminated sample along with a known standard solid solution of $BaBiO_3$ using the SEM INCA system. The advantages of this system over the ISIS being multiple point analysis and mapping over a large area of the sample, this would enable us to identify the contaminate and whether it is homogenous throughout the sample or present in small areas in the sample. This is impossible to do using TEM, which analyses a very small area of one crystal at a time.

Results

Images of the standard sample *(Fig. 7.19)* and the contaminated sample *(Fig. 7.20)* were taken firstly to see if there was an apparent change in morphology between the two samples, either in the size of the crystals or indeed of the shape.

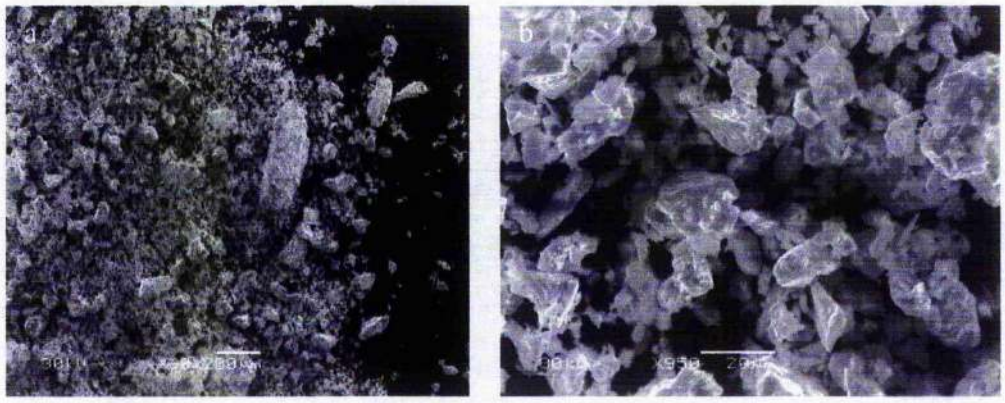

Fig's. 7.19(a) An image at low mag x60 of the standard $BaBiO_3$ sample, (b) the same sample taken at much higher magnification, x950.

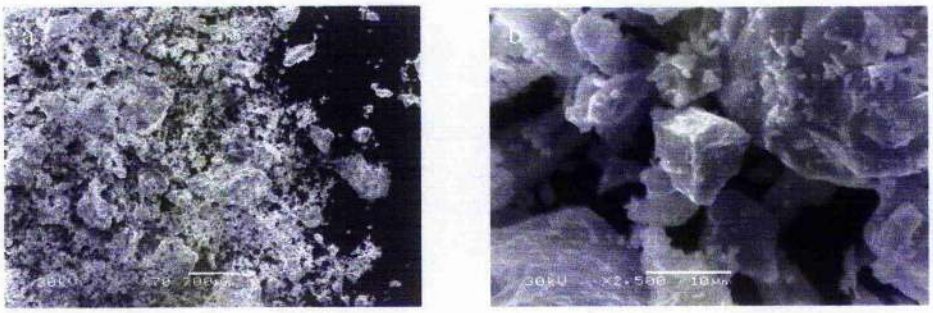

Fig's. 7.20 (a) is an image at low mag x70 of the possibly contaminated sample, (b) is the same sample of $BaBiO_3$ taken at higher magnification, x2,500.

The images above are at different magnifications and show similar morphology; indeed it would probably be impossible to identify a trace element contamination by morphology even at very high magnifications.

Point ID

Point ID microanalysis was carried out on the standard sample *(Fig. 7.21)* and the contaminate *(Fig. 7.22)*.

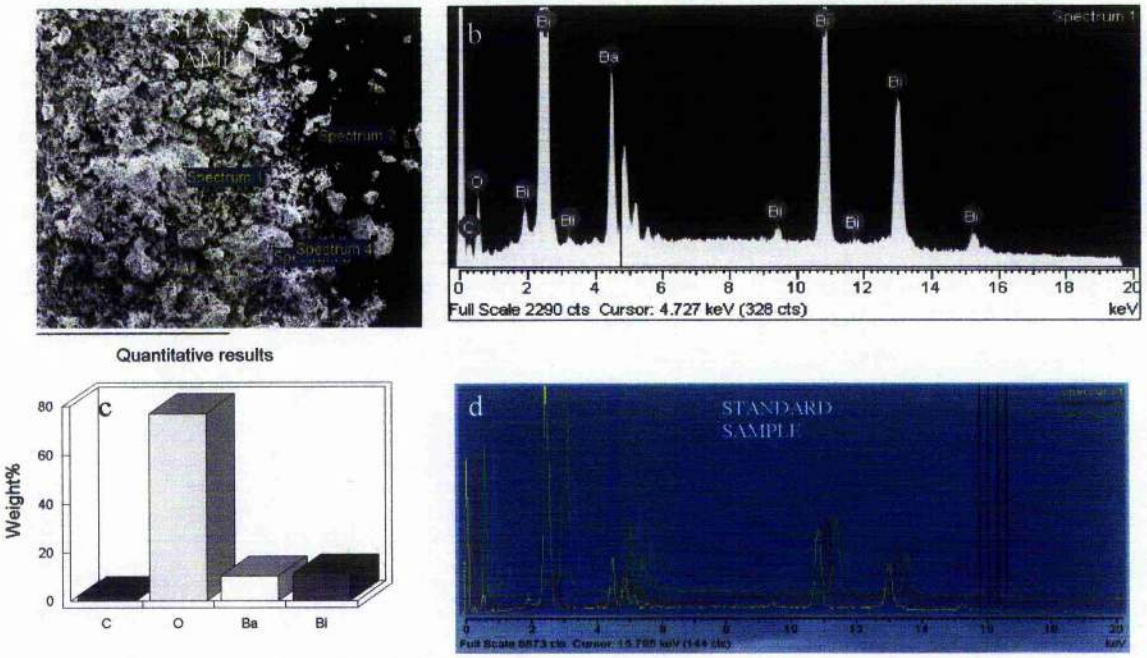

Fig. 7.21 Standard sample of BiBaO3 quant results.

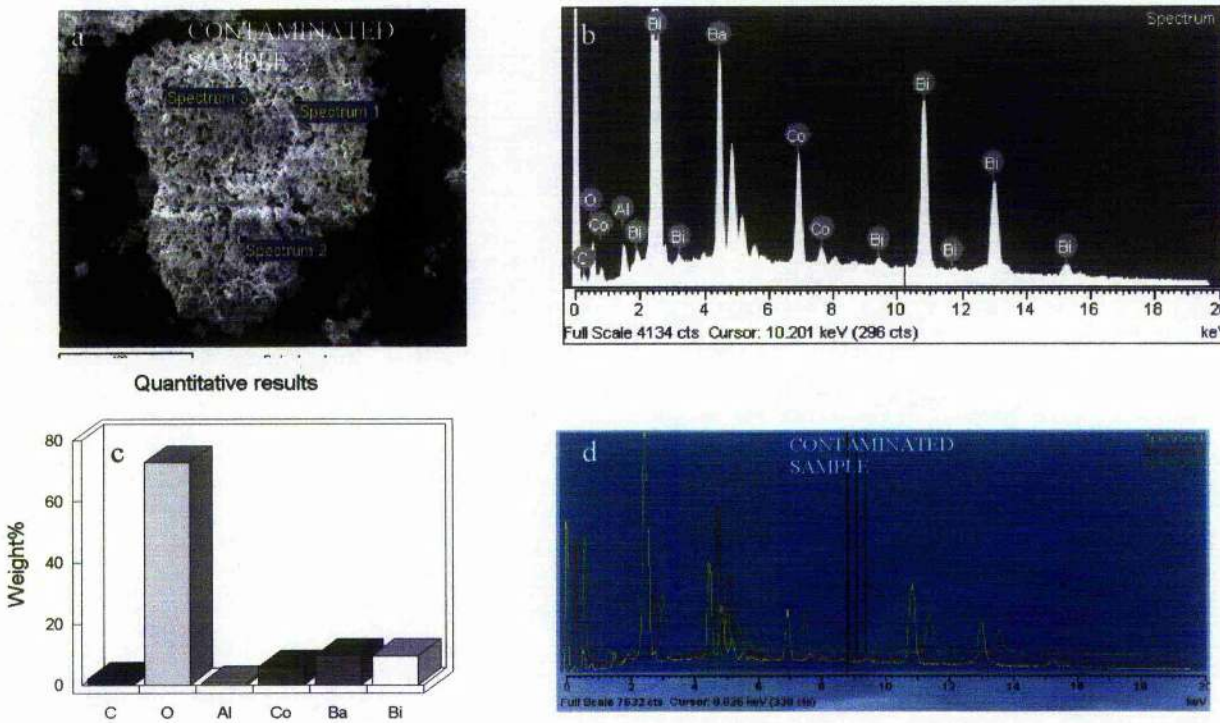

Fig. 7.22 (a) the sample with points for analysing, (b) spectrum after acquisition, (c) quantitative results, (d) three spectra superimposed to compare elemental peaks of the contaminated sample of $BaBiO_3$.

From these results it was confirmed that Co was the main contaminant with also some Al present. For both elements it was found that the Kα lines were the strongest Co Kα 6.92 and Al Kα 1.48 respectively. The ratio of the Ba:Bi seems largely unaffected by the contaminant, although interpretation of the results would obviously be compromised with the presence of Al and Co. What cannot be assumed from the above results is that the contaminants are spread throughout the sample, to show if this is, or is not the case mapping studies must once again be undertaken.

Mapping

An area of the standard solid solution was mapped (*Fig. 7.23)* initially for comparison; this would hopefully show the homogeneity of the principal elements, Ba,

Bi. The mapping should also show the heavy C content of the double-sided carbon film on which the powder sample is mounted. Carbon and oxygen however appear in any sample undertaking EDS microanalysis.

It is sometimes useful to see the heavy carbon round the sample as this gives some perspective to the sample especially if it is a single crystal. The mapping took place at an accelerating voltage of 30kV and a spot size of 40-50; the acquisition rate was approx 2.3 - 3Kcps over 30-40 minutes.

In retrospect the time of mapping for the standard sample should have been increased, as the signal from each element is rather weak, whereas the signal in the contaminated sample is a lot stronger

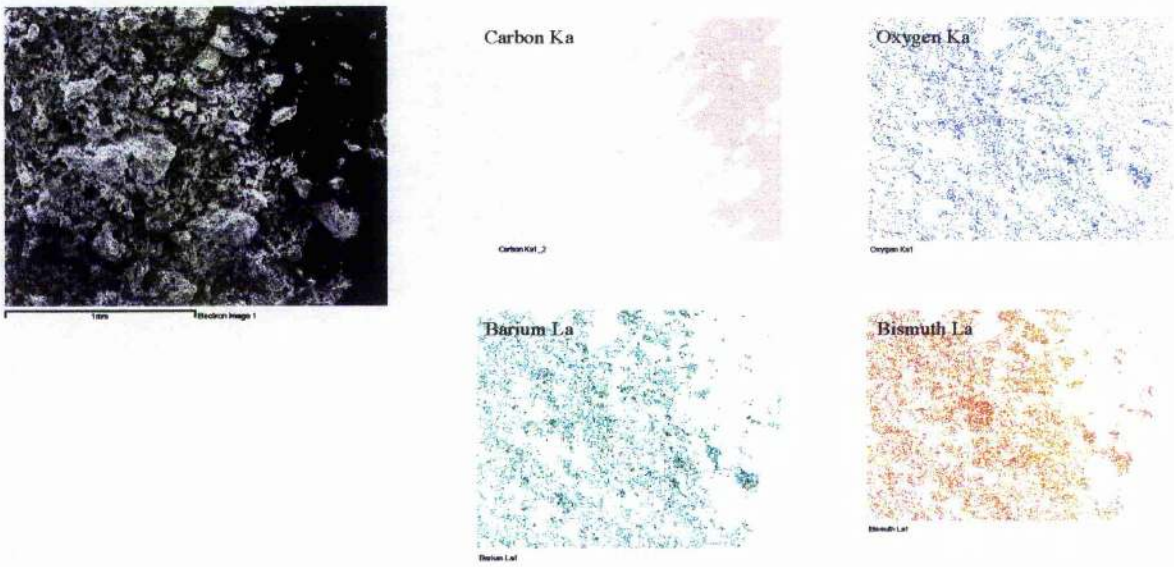

Fig. 7.23 Elemental mapping of the standard $BaBiO_3$ sample showing the area of interest and element concentration.

Mapping of the standard sample shows homogeneity for the Bi and the Ba, the heavy C signal is due almost totally to the insulating Carbon tape on which the powder sample sits. Mapping on an area of the contaminated sample (*Fig. 7.24)* was then carried out at 30kV. It should be noted that the longer the sample is left to map under a 30kV beam the greater and clearer the results. The mapping time used may be in the region of 30

min to 2 hours depending on the sample and acquisition rate. It follows that a low acquisition rate needs a longer time under the beam for better mapping results.

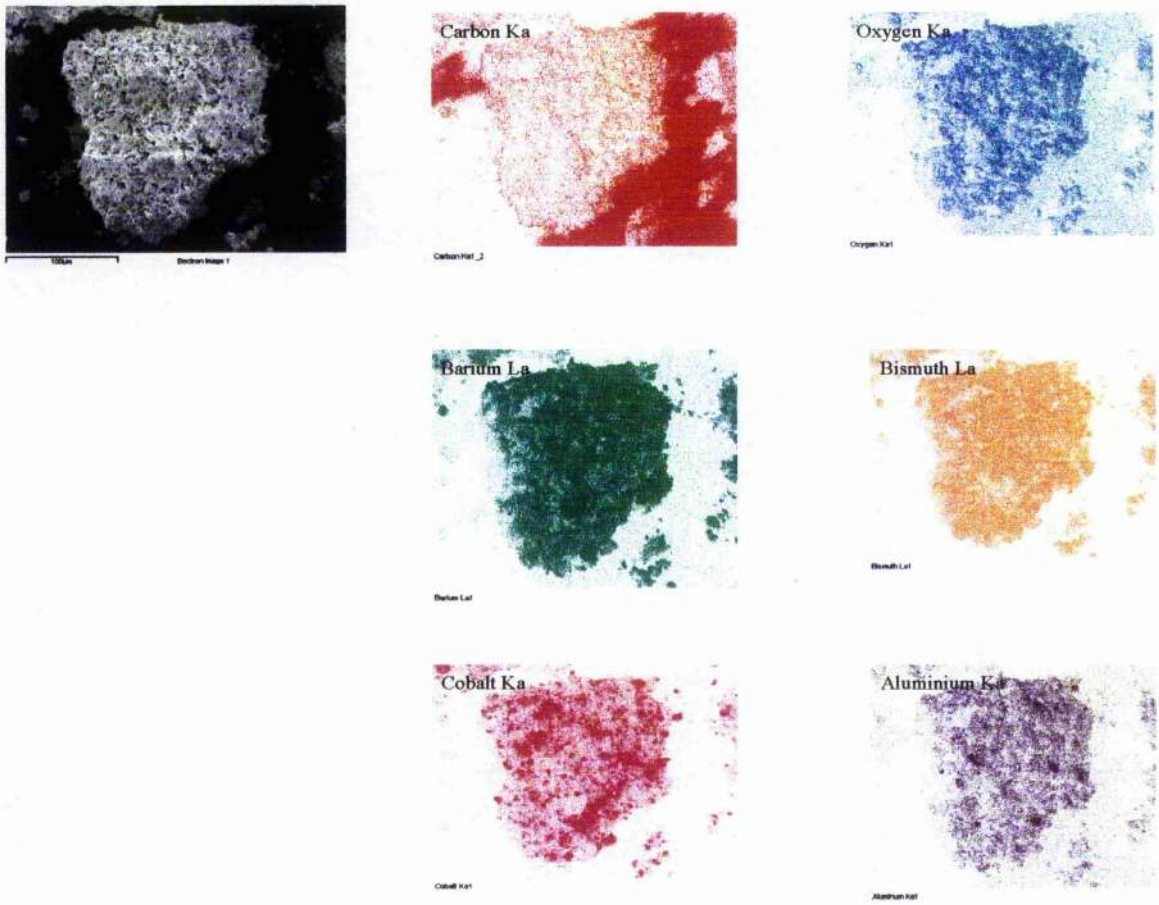

Fig. 7.24 mapping of the contaminated sample showing the area of interest and element concentration.

Results for the contaminated solid solution of $BaBiO_3$ shows a fairly dramatic result with high intensity areas of signal within the sample for cobalt and aluminium. The carbon signal is fairly high for the element within the sample, although much greater as would be expected for the surrounding carbon tape. However it can be seen that the carbon signal is very weak on the left hand side of the image where only carbon tape is

located, this could be due to the position of the actual sample to the detector, which may be obscuring the X-rays from that particular area, however it is more likely that they are due to the shadow of the particle itself. This phenomenon can also be seen to a lesser extent in the signal from the other elements on the left hand side of the sample especially with the O, Ba, and Bi mapping images. The two contaminants of Al and Co show very clearly and throughout the sample, however there are specific areas where the signal is very strong especially in the Co sample, it is in these areas that contamination is at its worst. It would appear that this is not a homogenous contamination of the solid solution and one more likely to have occurred during the synthesis of the $BaBiO_3$ solid solution.

7.5 Identification of metals within zeolite ZSM-5.

Introduction.

Zeolite based heterogeneous catalysts are used by industrial chemical companies in the interconversion of hydrocarbons and the alkylation of aromatic compound. A very good example of this is the zeolite ZSM-5 (*Fig. 7.25)* this was developed by Mobil oil; it is an aluminosilicate zeolite with a high silica and low aluminium content. Its structure is based on channels with insecting tunnels. The aluminium sites are very acidic. The substitution of Al^{3+} in place of the tetrahedral Si^{4+} silica requires the presence of an added positive charge. When this is H^+, the acidity of the zeolite is very high. The reaction and catalysis chemistry of the ZSM-5 is due to this acidity.

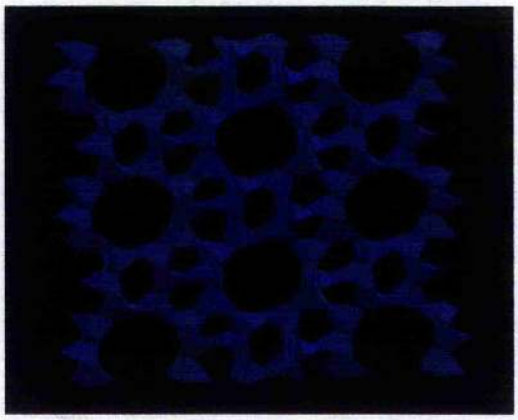

Fig. 7.25 Three-dimensional image of ZSM-5.

ZSM-5 is a highly porous material and throughout its structure it has an interesting two-dimensional pore structure. ZSM-5 has two types of pores, both formed by 10-membered oxygen rings. The first of these pores is straight and elliptical in cross section; the second pores intersect the straight pores at right angles in a zigzag pattern and are circular in cross section *(Fig. 7.26)*.

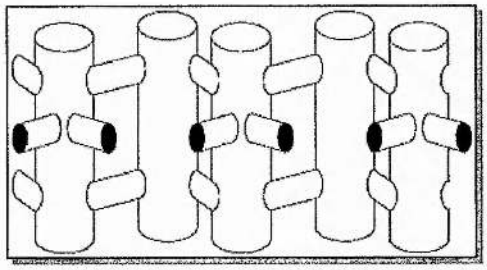

Fig. 7.26 Schematic drawing of the pore structure of ZSM-5.

This unique two-dimensional pore structure allows a molecule to move from one point in the catalyst to anywhere else in the particle. The large openings are the elliptical straight pores in the ZSM-5. For the MTG (methanol-to-gasoline) process it is the pores created by these 10 oxygen rings, along with the zigzag pores intersecting them that are essential to the formation of products that are desirable components of gasoline. An 8-oxygen ring zeolite will not produce molecules with 6 or more carbon; molecules of this size will not fit into the small pores of these zeolites. The large pores of a 12 –oxygen ring zeolite produce large amounts of C-11 and C-12 compounds, which are undesirable products of gasoline.

Zeolitic metal – ZSM-5 systems are active in the reduction of NO. It has been a long sought goal in the heterogeneous catalysis of Nitric Oxide to understand:

1. What makes a catalyst site highly active?
2. How may catalyst properties be tailored to have a concentration of active sites with strong resistance to deactivation.

3.To determine the reactivity using different metals of various types of CO and NO on Cu-ZSM-5, Co-ZSM-5, Fe-ZSM-5 etc catalysts under transient and solid state conditions, and to find out the catalytic activity.

Many new techniques have been used lately in the preparation of catalytic materials with novel properties, and to determine the catalytic properties of cobalt oxide and ceria

promoted metals. The site of these metals in ZSM-5 is also a consideration. In this respect EDS chemical analysis is an essential tool in the determination of the metals within the ZSM-5 system and their location and concentration. ZSM is usually synthesised under hydrothermal conditions, from solutions of aluminate, sodium silicate or sodium hydroxide. The templating ion is critical. The templating ion is usually an organic cation around which the aluminosilicate lattice is formed, so that the tunnel size is determined by the templating cation. ZSM is formed by a careful procedure of heating and purification of the product. The metals, in this study were then substituted for Si. The following ZSM samples were synthesised and supplied by Prof Russell Morris, Dept of Chemistry, University of St Andrews.

Fe-ZSM-5

An area on the sample was chosen that reflected the appearance of the overall sample and a spectrum acquired for quantitative analysis *(Fig. 7.27)* and following this elemental mapping *(Fig. 7.28)*

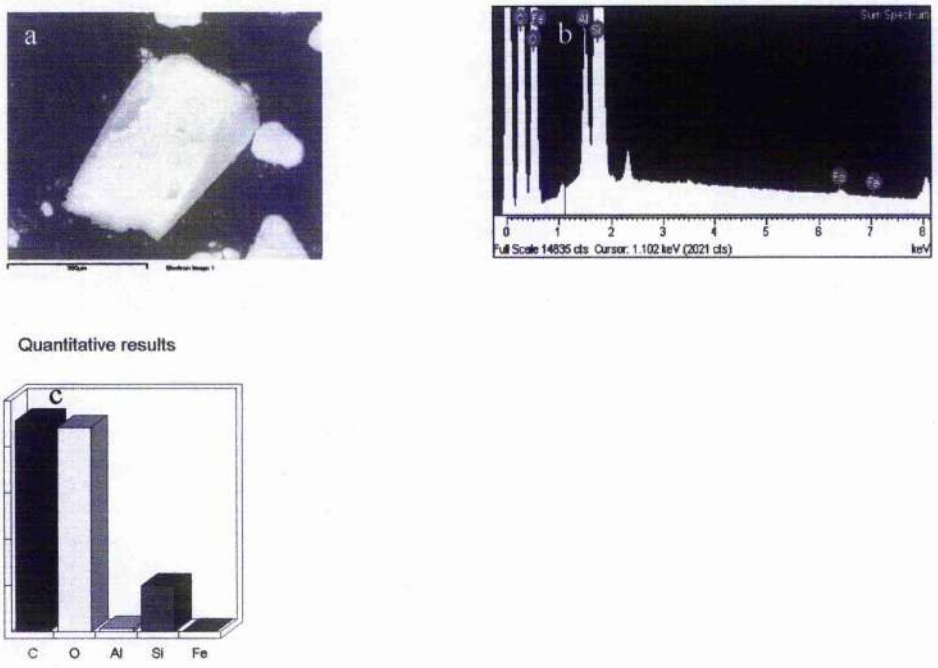

Fig. 7.27 (a) the area for analysing from Fe-ZSM-5, (b) spectrum after acquisition, (c) quantitative results.

Fe ZSM-5 is an active catalyst for the production of methanol by the oxidation of methane. Some present studies deal with the effect of the different Si/Al ratio on the local structures of the Fe-oxides within the Fe-ZSM-5 decomposition of N_2O into N_2O_2

From the quantitative results it can be seen that there is a significantly higher weight % of Si to Al, and a small quantity of Fe. The homogeneity of the sample is then confirmed using elemental mapping *(Fig. 7.28)*

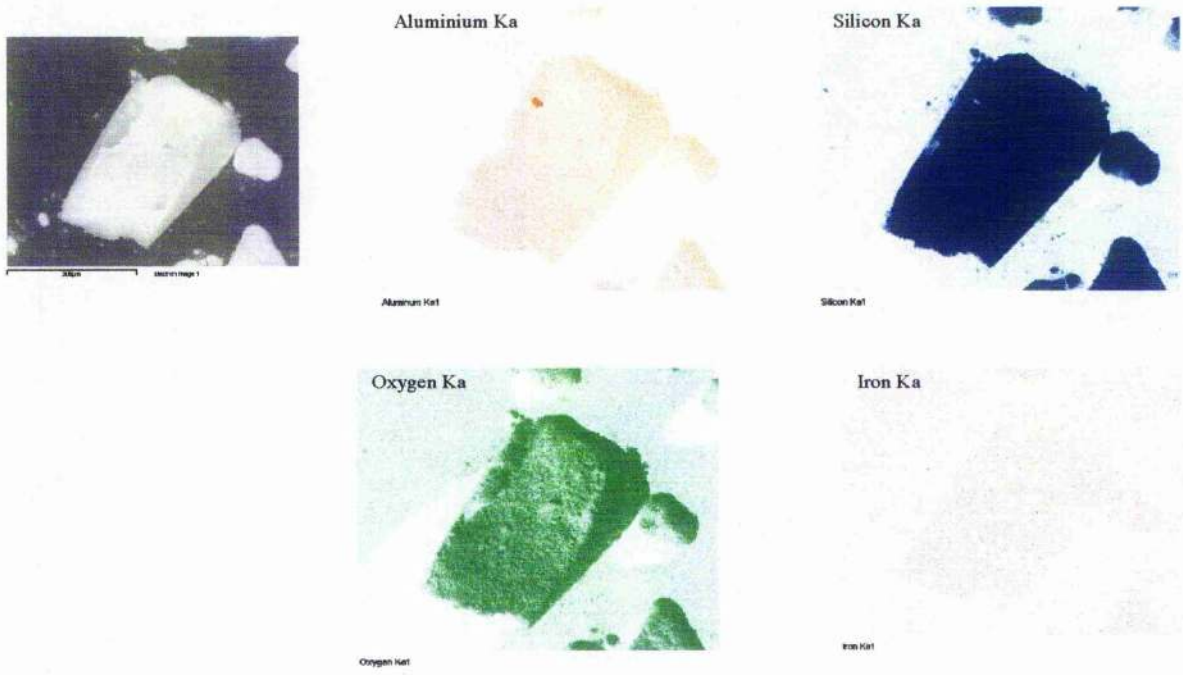

Fig. 7.28 Elemental mapping analysis, showing concentration of separate elements.

Homogeneity of the sample is confirmed by the above results, with a heavy signal for Si, followed by O then Al. The Fe content is less than the other elements, however the signal is strong enough to show that Fe is spread throughout the sample and not only in localised isolated areas.

Co-ZSM-5

Co-ZSM-5 is also a de NO_X catalyst. This is usually prepared by wash-coating a cobalt ion exchanged ZSM-5 zeolite together with an alumna binder on a co-ordinate honeycomb structure. This can then be tested for NO_X reduction with C_2H_4 under oxidising conditions in a certain temperature range.

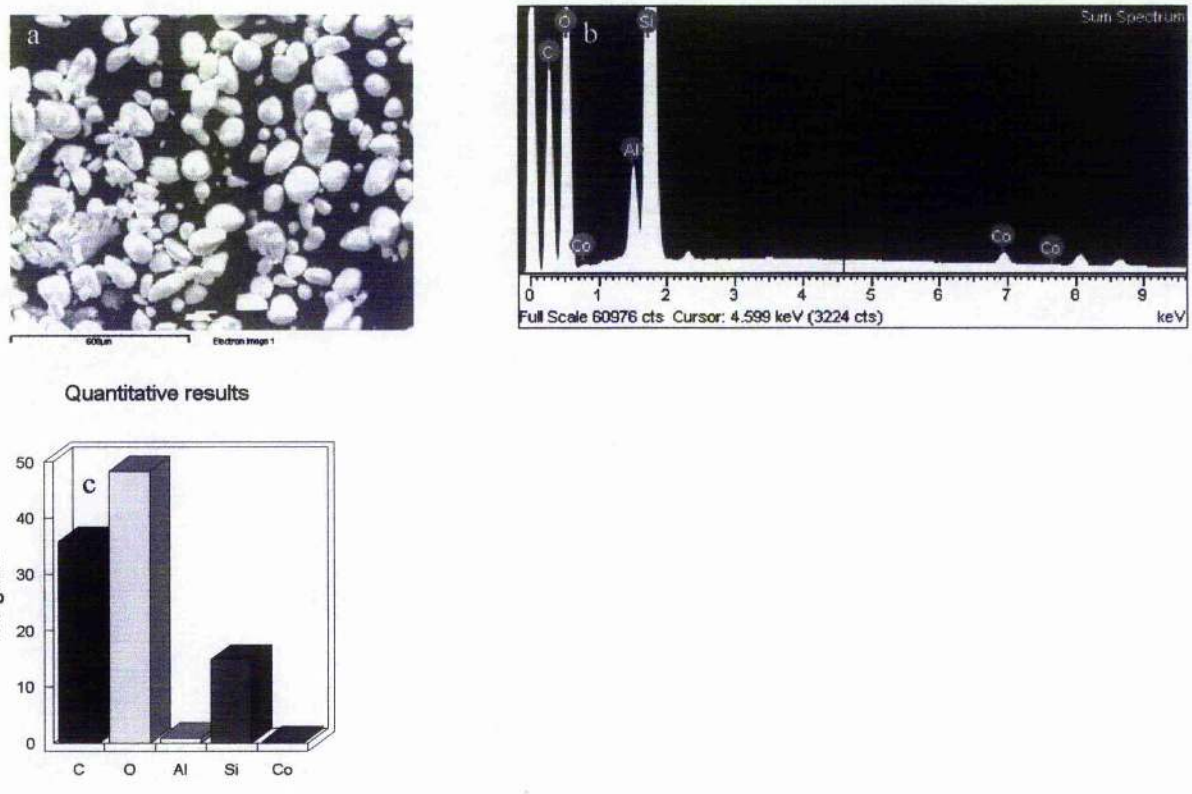

Fig. 7.29 (a) the area from Co-ZSM-5 for analysing, (b) spectrum after acquisition, (c) quantitative results.

The Si % weight is greater than the Al as in the Fe-ZSM-5, although in this case even more so, the Co has the smallest amount of weight % of any of the elements. The area chosen for the point ID analayis was over a much greater area of the sample, shown in the micrograph (*Fig. 7.29a)* above.

Distribution of each of the principal elements in the Co-ZSM-5 sample can be obtained once again using elemental mapping (*Fig. 7.30).*

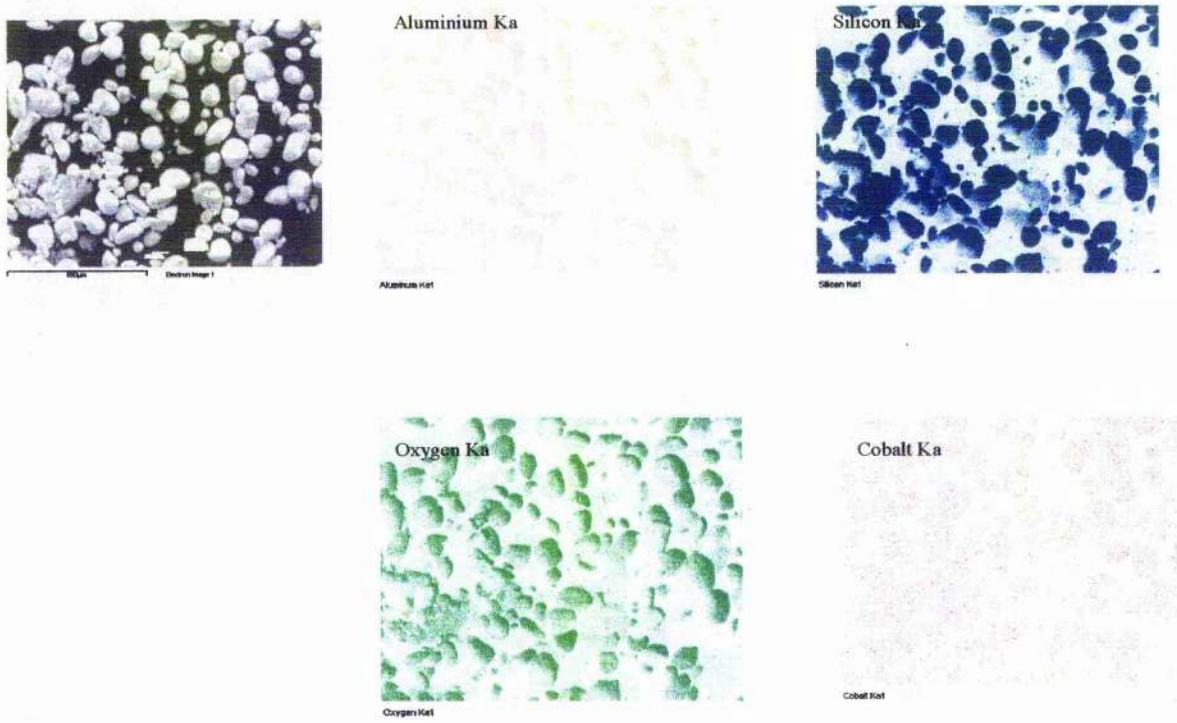

Fig. 7.30 Elemental mapping analysis showing concentration of separate elements of the Co-ZSM-5 sample.

Distribution and concentration of the four elements is consistent with that of Fe-ZSM-5. There is a high signal for Al but a much higher one for Si. Oxygen as would be expected, once again has a significant presence and has a consistent distribution. The Co would appear to be homogenous although the signal is relatively weak in comparison with the other elements present. As in the previous sample background signal is a problem and therefore a long acquisition time of at least an hour is beneficial for good solid mapping results.

Cu-ZSM-5

Cu-ZSM-5 is another of those catalysts, which reduce NO_X with hydrocarbons in a net oxidising atmosphere. There is in Cu-ZSM-5, as in the two previous samples a relationship between, in this case the state of the Cu and in its reactivity, and also in the change of state of the Cu with thermal deactivation. In previous work (*Tanabe 1995)* it was discovered that this thermal deactivation was found to occur by the migration of copper ions, which was induced by the de-alumination of zeolite and not by the aggregation of copper ion.

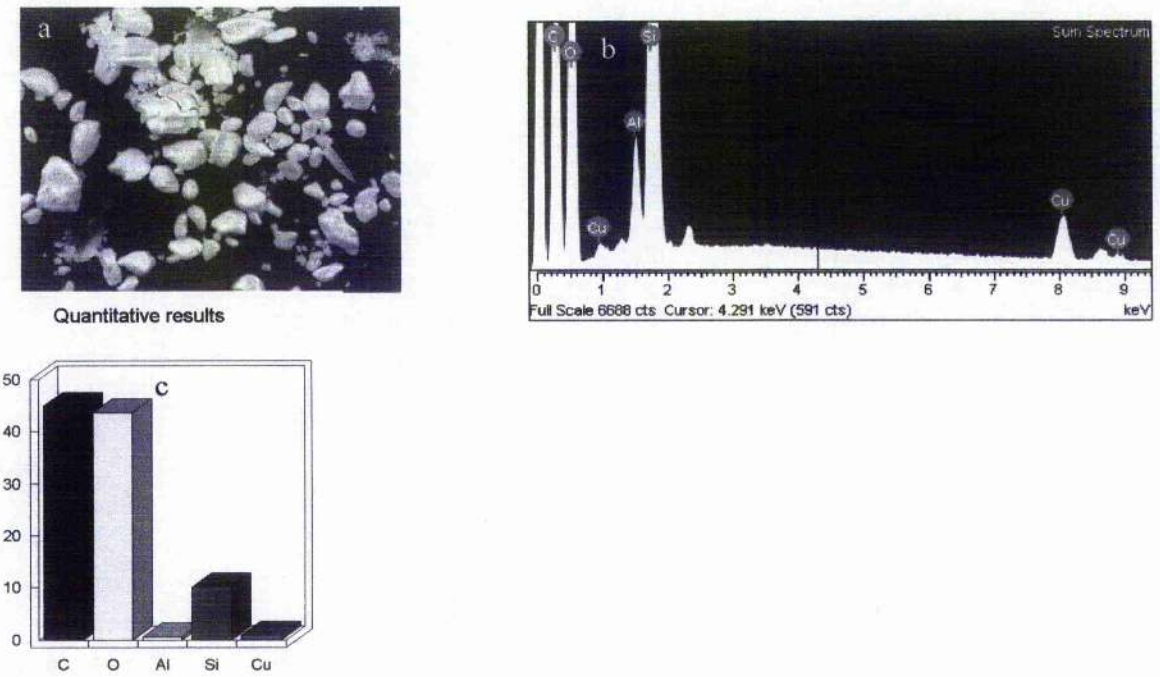

Fig. 7.31 (a) the sample area for analysing, (b) spectrum after acquisition, (c) quantitative results for Cu-ZSM-5.

Similar results were obtained for the Quant Analysis results as in the previous samples (*Fig. 7.31).* If anything was to be noted, it is that there is a very slight increase in the Al weight %, also the Cu content in this sample is raised in relation to the metals

(Fe, Co) in the previous ZSM-5 samples. Both weight % for Si and Al Seem to be slightly down on the last samples.

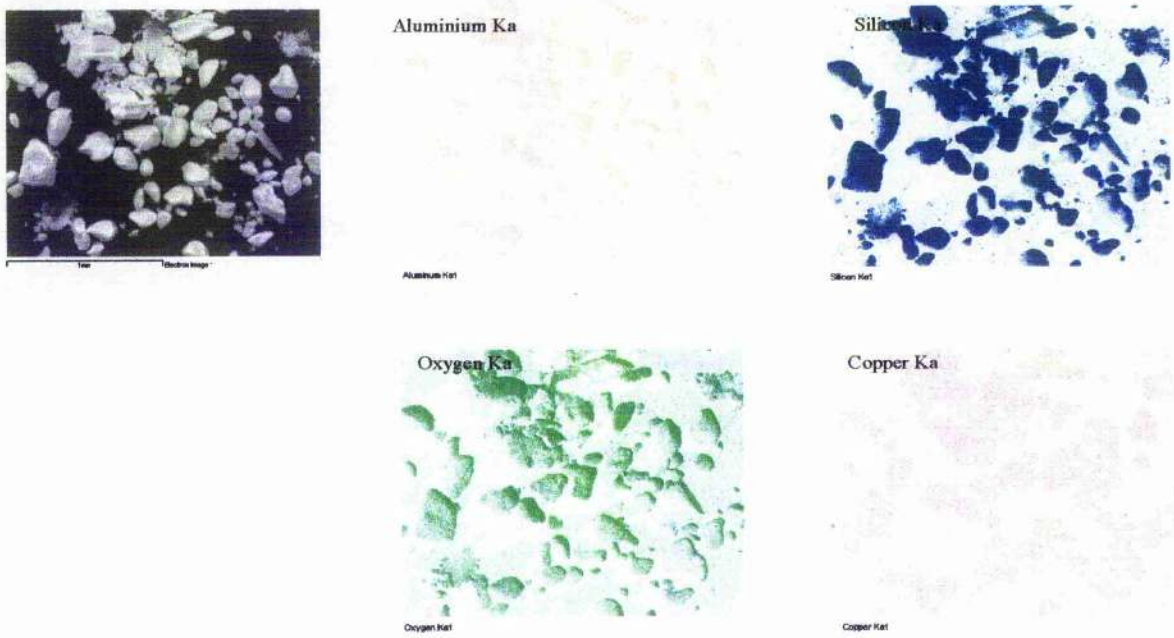

Fig. 7.32 Elemental mapping analysis showing concentration of separate elements of the Cu-ZSM-5 sample.

Elemental mapping confirms that the metal element, in this case Cu has an increased presence over that of Fe and Co in ZSM-5 in the previous samples, and it is homogenous throughout the sample. The Al, content of the sample has decreased as has the Si content, O appears constant.

Ni-ZSM-5

The final sample Ni-ZSM-5 is also a **molecular sieve** and also can be used in the reduction of NO_X.

Molecular sieve

A molecular sieve is the desiccant of choice for many applications. This is a synthetically produced zeolite that enables the selective adsorption of polar molecules to take place at low vapour pressures. Molecular sieve will reduce relative humidity to zero and is widely used in the pharmaceutical, electronic and chemical industries. Molecular sieve can have several pore sizes.

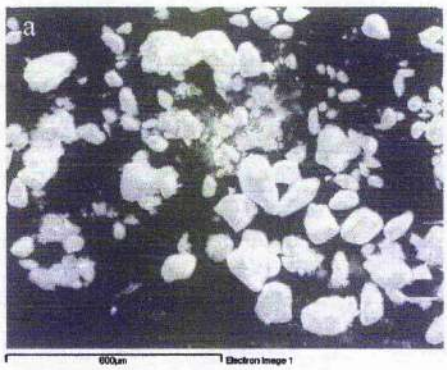

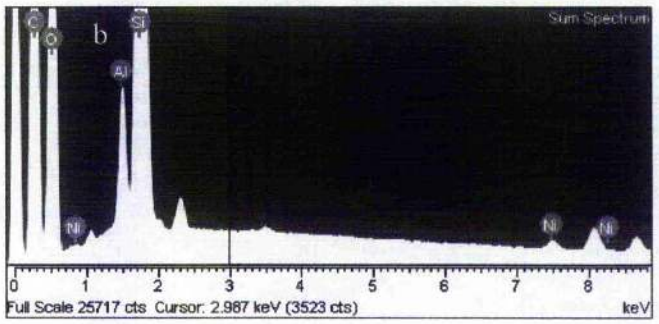

Quantitative results

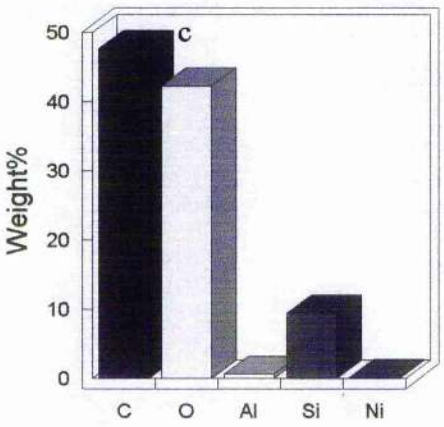

Fig. 7.33 (a) the sample area for analysing, (b) spectrum after acquisition, (c) quantitative results for Ni-ZSM-5.

The results for the Quant analysis in Ni-ZSM-5 show Al at a very low Weight% as is Ni. Although the metal element is scarce the result is consistent with the Weight % of the other metal elements in the previous ZSM-5 (*Fig. 7.34)* samples.

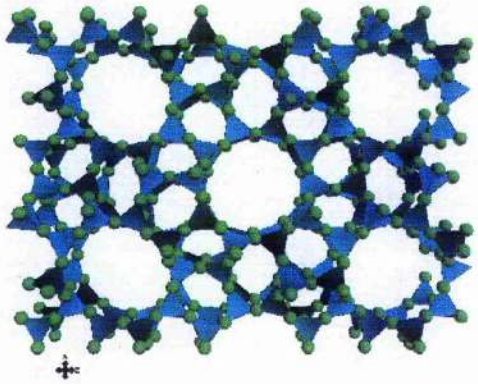

Fig. 7.34 ZSM-5 is also known as ***MFI.***

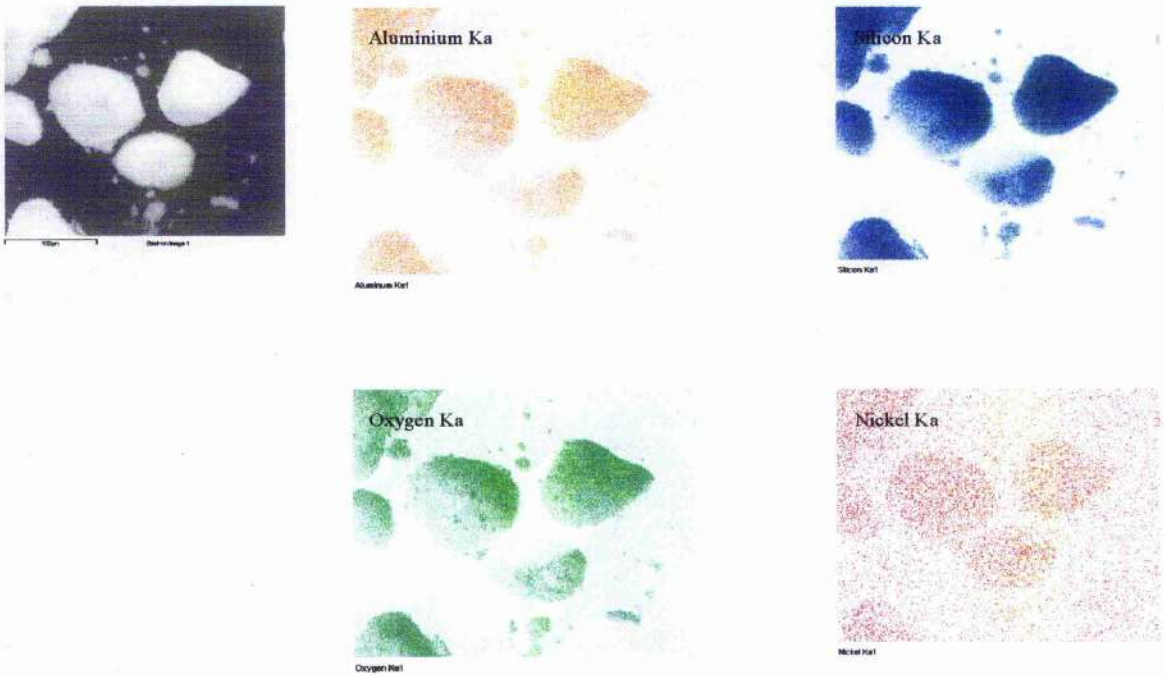

Fig. 7.35 Elemental mapping analysis showing concentration of separate elements of the Ni-ZSM-5 sample.

Mapping, finally for this sample (*Fig. 7.35)*, shows the expected homogeneity for the four elements. However it can be seen that the background signal in the Ni image is noisy, this may be due to the fairly long acquisition time for mapping.

The mapping was acquired over a period of one hour in order for Ni to show in the sample and therefore perhaps this explains the rather messy background. There are also areas in the sample, (especially in the O and Si) that show an apparent weak signal, this does not imply less of the element, rather this is more likely due to absorbance of X-ray from one part of the sample to another, being shielded from the X-Ray detector or possibly, that one part of the sample is actually closer to the detector than another. These are all possibilities that can occur when dealing with the EDS of powder samples.

Chapter 8 Conclusions

It has previously been thought that the accelerating voltage used for EDS microanalysis for SEM should be the maximum for the machine, in the case of non-field emission SEM this is 30 Kv. However it has been shown during this part of the thesis that the accelerating voltage can be decreased sufficiently to expose peaks of the very light element (excepting Hydrogen) such as Nitrogen. This was shown using microanalysis on NH_4Cl at a range of voltages from 3-30 kV.

Just as imaging and the voltage used for this are determined by the kind of sample, it is also the case that the voltage and spot size can be adjusted to give the optimal X-ray acquisition for a particular element. In very low voltage i.e.: 5kV the time frame for acquisition may be increased accordingly. From results it can be concluded that the current practice of using only high voltage for X-ray acquisition is at the very least debatable and at worst clearly wrong for certain elements. The decrease in voltage may lead to an increase in atomic% and improvement in weight % for light elements such as Nitrogen.

It was also shown that in this section of the thesis that SEM imaging and chemical analysis of solids encompasses many sorts of samples, not only powder samples but also paper, rubber, plastics and ceramics. All of these can be analysed with great success if voltage and spot size are taken into consideration. Some samples react adversely to a strong electron beam and therefore low voltage is required for imaging. In the case of EDS on those samples, acquisition time can be increased accordingly to obtain a satisfactory set of results.

Point ID was shown to be the process of choice for initial elemental identification and ratio within a sample, however for identifying homogeneity elemental mapping is far more useful.

Techniques undertaken in this thesis also show that temperature variations change the positions of the elemental peaks and that the microscope beam current will vary with time. In this case undertaking of beam quant calibration is advised for better results. This optimization should be performed at least ideally every two hours under normal working conditions for consistent results. The elements used for calibration are dependant on the

expected elemental peak positions from the sample and the voltage selected. In using 20kV voltage i.e. normal conditions, pure Co and Cu are suitable optimization elements. Cu is a better optimising standard for elements at the higher energy range of the spectrum, whereas Co is a better standard to use for those elements at the lower energy range of the energy spectrum.

Scanning electron microscopy EDS microanalysis has a definitive role to play also in the analysis of ZSM-5 and its site of metals. It identifies the presence of a metal, its relative quantity in its ratio with other elements, and its homogeneity within a sample.

One drawback of Elemental Mapping of ZSM-5 is that it is only qualitative information. That is they show us only relative amounts i.e. in the case for Fe, Co, Ni, Cu this makes it difficult to make comparisons.

However these maps do have the potential for being quantitative. An example would be to utilize the individual maps for defining the special area of the elements and then simply counting pixels for measuring percent metal versus Si and Al.

It is however far easier to use Point ID with a standard and acquire data from many points on a sample or use Analyzer for elemental quantitative analysis over the whole area which is to be mapped. When this is done it is consistently seen that the metal element presence is very small relative to the Al, Si which make up the bulk of the catalyst ZSM-5.

In this section it has been shown that it is not an understatement to state that scanning electron microscopy is one of the most useful analytical techniques used by to-days solid state chemists in the characterisation of solids. In the complex samples mentioned in this section phase identification is prerequisite to detailed characterisation.

Appendix A

XPD study of some Ba rich compositions of $BaBiO_3$ system.*

BaBiO3		d(1.1:0.9)	d(1.2:0.8)	d(1.4:0.6) **
d(A)	hkl			
				5.01
4.35	100	4.35	4.35	4.35
			3.10	3.69
3.07	110	3.07	3.07	3.08
			2.62	2.64
2.18	200	2.17	2.17	2.18
			2.01	2.01
3.3	210	1.94	1.94	1.96
1.77	211	1.77	1.77	1.79
				1.68
1.53	220	1.53	1.53	1.55
				1.48
1.44	221	1.45	1.45	1.46
1.37	310	1.37	1.37	1.38
1.25	222	1.24	1.25	1.26

*All of the d values were obtained using Stoe winXPOW software based on the XRD patterns. The numbers in blue represent the d value of spots that fall outwith those of the basic perovskite pattern as taken from the standard sample.

** (x: y) is the mole ratio of Ba to Bi.

Appendix B

Unit cell dimensions of Ba and Bi rich compositions of the $BaBiO_3$ system.

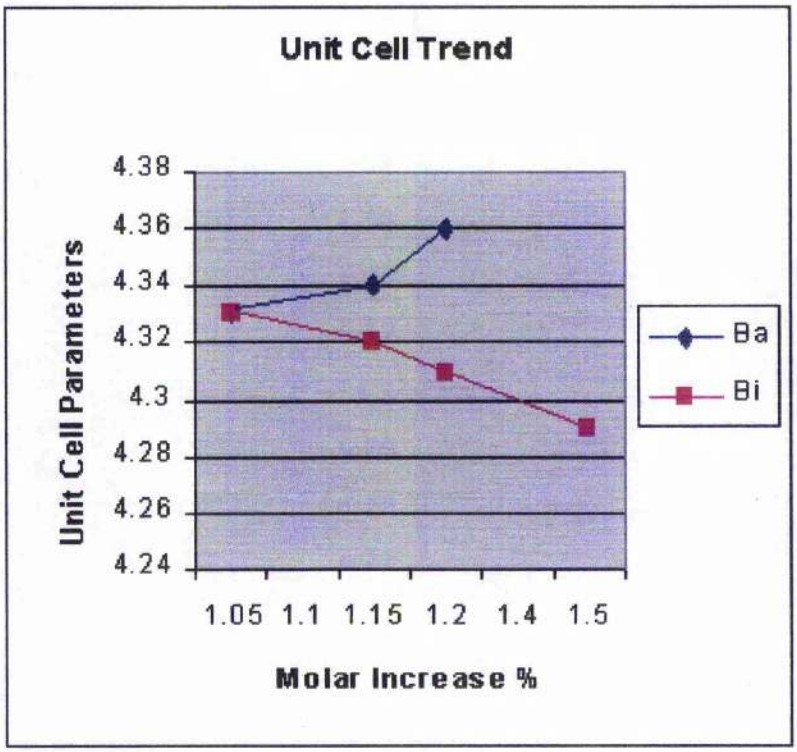

Appendix B showing the trend whereby the unit cell increases with the increase in molar% of Ba and decreases with an increase of molar% Bi in the $BaBiO_3$ system.

References and Bibliography

P. B. Allen and I. B. Bischofs, *Phys. Rev. B 65, 115113* (2002).

J. T. Armstrong, *Microbeam Analysis-1988, Ed. DE Newbury. San Francisco Press, San Francisco, 239-246,* (1988).

J. S. Beck, J. C. Vertuli, W. J. Roth, J. Am. Soc. 114, 834 (1992).

L.W Beck, J. L White, J. F Haw, *J. Am. Chem. Soc., 114,* 6182 (1992).

L. W. Beck, T. R. Kraweitz, D.H Barich, *J. Am. Chem. Soc. 117, 1047-1048* (1995).

J. B. Boyce, F. G. Bridges, T. Claeson, T. H. Geballe and J. M. Remeika, *Phys. Rev. B 41, 6306* (1991).

J. B. Boyce, F. G. Bridges, T. Claeson, T. H. Geballe, G. G. Li and A. W. Sleight, *Phys. Rev. B 44, 6961* (1991).

D. W. Brect, *in Zeolite Molecular Sieves:Struc. Chem. and use, Johwilley, London* (1974).

A. N. Broers, *J. Appl. Phys. 38, 1991-1992* (1967).

C. Chaillout, M. Marezio, J. P. Remeika and A. Santoro, *Solid. State. Commun. 65, 1363* (1988).

X. Cheng, J. Chaudhuri, J.H. Edgar, *J. Elec. Mat. 26, 1389-1393* (1997).

A. E. Conrady, *Applied optics and optical design, part one, Dover publications* (1985).

J. M. Cowley and A. F. Moodie, *Acta. Cryst. 10, 609* (1957).

D. E. Cox and A. W. Sleight, *Solid. State. Commun. 19, 969* (1976).

D. E. Cox and A. W. Sleight, *Acta. Cryst. B35, 1* (1979).

P. A. Cox, *The electronic structure and chemistry of solids, Oxford science publications, chapt 7, 195-196,* (1987).

P. A. Cox and V. E. Henrich, *The surface science of metal oxides, Cambridge University press* (1994).

M. J. Danks, H. B. Jervis, M. Nowotny, W. Zhou, T. A. Mashmeyer and D. W. Bruce, *Catalysis Letters Vol. 82, No. 1-2, 95-98* (2002).

P. Echlin, C.E. Fiori, J. Goldstien, D. C. Joy, D. E. Newbury, *Advanced Scanning Electron Microscopy and X-ray analysis* (1986).

T. E. Everhart and R. F. M. Thornley, *J. Sci. Inst. 37, 246* (1960).

P. J. Goodhew, J. Humphries, R. Beanland, *Electron Microscopy and analysis, Third edition, Taylor and Francis, London* (2001).

M. S. Hegde, P. Barboux, C. C. Chang, J. M. Tarascon, T. Venkateson, *Phys. Rev. B 39, 4752* (1989).

Y. Koyama and M. Ishimaru, *Phys. Rev. B 45, 9966* (1992).

C. T. Kresge, M. E. Leonowicz, W. J. Roth, J. C. Vartuli and J. S. Beck, *Nature. 359, 710* (1992).

L. F. Matheiss, E. M Gyorgy, D. W Johnson, *Phys. Rev. B 37, 3745* (1988).

M. R. McCartney, P. Kriut, A. H. Buist, M. R. Scheinfein, *Ultramicroscopy. Vol 65, issue 3, 179-186* (1996).

N. K. McGuire and M. Okeefe, *Solid. State. Commun. 52, 433* (1984).

B. McEnaney, T.J. Mais, J. Rouquerol, F. Rodríguez-Reinoso, K.S.W. Sing, K.K. Unger, *The Royal Society of Chemistry, Special Publication No. 213 351-358* (1997).

R. L. Myklebust, C. E. Fiori, K. F. J. Heinrich, *Spectral Processing Techniques in a Quantitative energy Dispersive X-Ray Microanalysis Procedure (FRAME C). NBS Special Publication 604, pp.365-379* (1981).

T. Nakamura, S. Kose and T. Sata, *J. Phys. Soc. Jpn. 31, 1284* (1971).

V.I Nikolaichik, S. Amelinckx, L.A. Klinkova, N.V. Barkovskii, O.I. Lebedev and G.Van Tendeloo, *J.Solid State Chem. 163, 44* (2002).

A. F. Orchard and G. Thornton, *J.Chem.Soc.Dalton Trans. 1238* (1977).

N. K. Ramen, M. T. Anderson and C. J. Brinker, *Chem. Mat. 8, 1682* (1996).

Ø. Rist, A. Rike, L. Ljones, P. H. J. Carlsen, *Molecules, 6, 979-987* (2001).

M. B. Robin and P. Day, *Adv. Inorganic. Chem and Radiochem. 10, 247* (1967).

H. Sakuma, H. Hashizume, A. Yamanaka, *Acta Cryst B46, 693-698* (1990).

J. H. Sinfelt, *Bimetallic Catalysts, An Exxon Monograph, J. Wiley, New York* (1983).

W. Sleight, J. L Gillson, P. E Bierstadt, *Solid. State. Commun. 17, 27* (1975).

W. J. Smith, *modern optical engineering 3rd edition, McGraw-Hill* (2000).

O. T. Somorjai, *Cornell University Press, Ithaca, New York* (1981).

T. Tanabe, *Reactivity and co-ordination structure of Cu ion in Cu-ZSM-5 for NO_X reduction catalysts, Technical Journal: R+D review vol 30-31* (1995).

G. Thornton and A. J. Jacobsen, *Acta. Cryst. B34, 351* (1978).

S. H. Tolbert, A. Firouzi, G. Stucky, B. F. Chmelka, *Science. vol 278, 264-268* (1997).

Y. J. Uemura, B. J. Sternlieb, D. E. Cox, *Nature. 335, 151* (1988).

D. Vann Dyck, S. Van Aert, A. J. den Dekker, A. van den Bos, *Ultramicroscopy 98, 27-42* (2003).

T. E. Weirich, *International school of crystallography* (2004).

A. F. Wells, *Structural. Inorganic. Chemistry. Oxford. University. Press. 484* (1962).

G. K. Wertheim, J. P. Remeika and D. N. E. Buchanan, *Phys. Rev. B26, 2120* (1982).

C. G. Wu, and T.Bein, *Chem. Mater. 6, 1109* (1994).

W. Zhou, *Progress in TEM applications in material science. 1, 1-26* (1999).

W. Zhou, *Micron. 31, 605-611* (2000).

W. Zhou and J. Klinowski, *Chem. Phys. Lett. 292, 207* (1998).

W. Zhou, R. Mokaya, Z. Shan, T. Maschmeyer, *Progress in natural science, Vol. 11 No. 1* (2000).